Quantum Dynamics of Ultrafast Dissipative Processes

Thesis submitted for the degree

Doctor of Philosophy

by

David Gelman

Submitted to the Senate of the Hebrew University

February 2006

Quantum Dynamics of Ultrafast Dissipative Processes

Thesis submitted for the degree

Doctor of Philosophy

by

David Gelman

Submitted to the Senate of the Hebrew University

February 2006

This work was carried out under the supervision of

Professor Ronnie Kosloff

I would like to express my sincere gratitude to my teacher Professor Ronnie Kosloff for his guidance and patience

Abstract

This thesis is devoted to developing a fully quantum theoretical model of systems embedded in condensed phases, which are subject to ultrashort laser pulses. These systems are ubiquitous in chemistry, and there is a strong need in a comprehensive theoretical framework for interpretation and prediction of experimental data. The chief obstacle facing dynamical simulations of many-body systems is the exponential scaling of the computational effort with the number of degrees of freedom. Despite the growing number of theoretical methods, no comprehensive solution to this scaling problem has been achieved. Most of the existing theoretical methods fail to provide a consistent treatment of all aspects of a quantum dissipative system.

The Surrogate Hamiltonian method, which is the basis of the presented work, has been developed for simulating quantum transient phenomena taking place in a condensed-phase environment. The method is based on constructing a surrogate finite system-bath Hamiltonian, that in the limit of an infinite number of bath modes reproduces the true dynamics of the system. Employing a finite Hamiltonian makes the proposed method particularly suitable for ultrafast processes.

The method requires solving the time-dependent Schrödinger equation of the combined system rather than the Lioville von Neumann equation of the reduced density matrix. As a result, the Surrogate Hamiltonian starts with a fully correlated initial state, and the treatment of time-dependent external fields poses no problem. The method is not restricted to special forms of system-bath coupling, and formally, no weak coupling assumption is employed.

The first part of this thesis presents a numerical comparison between a spin bath (employed by the Surrogate Hamiltonian) and a widely-used bath of harmonic oscillators. The dissipative quantum dynamics of an anharmonic oscillator coupled to a bath is studied with the purpose of elucidating the differences between the

relaxation to a spin bath and to a harmonic bath. The main findings confirmed the fact that in the weak coupling limit the harmonic bath can be mapped to the spin bath. In addition, under this limit the spin bath converges with only single excitations of the bath modes, which means that the system and the bath are almost disentangled.

The spin and harmonic baths begin to deviate when the initial excitation of the primary system is increased. The first indication of differences is the requirement for two simultaneous bath excitations in order to converge the spin bath. For longer time periods, the spin bath saturates, limiting the ability to assimilate the system's energy. The effect of the saturation can be reduced if the bath Hamiltonian includes a mode-mode coupling term, spreading the excitation between the non-resonant modes.

The possibility of entanglement of bath modes mediated by the primary system is a major conceptual difference between the spin bath and the harmonic bath. Nevertheless, the very similar dynamics observed in the weak and medium coupling cases indicate that from the viewpoint of the reduced dynamics it is hard to distinguish between the two baths.

The original construction of the method was limited to phenomena at low temperatures. The new method, presented in this thesis enables employing the Surrogate Hamiltonian to a wider range of temperatures with more favorable scaling properties. The method is based on averaging over random phase thermal wavefunctions - Boltzmann-weighted, random-phase superpositions of states in the combined system-bath Hilbert space.

The random phase method obtains converged results for thermal observables by averaging a relatively small number of randomly chosen initial states. Moreover the number of initial states required to obtain convergence is a decreasing function of the size of the total Hilbert space due to self-averaging, and it also decreases with temperature. These findings suggest that the Surrogate Hamiltonian method has the same scaling properties for the zero temperature simulation as for the finite temperature simulations. As a consequence, the Surrogate Hamiltonian method can be applied for moderate temperature simulations, as long as the bath modes do not saturate.

The effect of the dissipation on nonadiabatic dynamics has been discussed in the second part of this thesis. The numerical extension of the Surrogate Hamiltonian method to multidimensional models has been employed to provide a new insight into nonadiabatic processes. Particularly, the system containing a conical intersection in the presence of a dissipative environment has been studied with the purpose of identifying observable ultrafast spectroscopic signatures. A model system, consisting of two vibronically coupled electronic states with two nuclear degrees of freedom, has been constructed. Dissipation was treated by two different methods: Lindblad semi-group formalism and the Surrogate Hamiltonian approach. Pump-probe experimental expectation values such as transient emission and absorption have been calculated and compared to the adiabatic and diabatic population transfer. The main findings of our work support the physical picture of rapid curve-crossing in the case of conical intersection. The stimulated emission signals have shown decay on a time-scale of tens of femtoseconds. The energy relaxation, dominated by an intramolecular vibrational relaxation and monitored by the transient absorption signal, proceeded at a much slower time scale. This suggests that conical mixing symmetry is in itself not sufficient to generate a femtosecond relaxation, measured experimentally as a fast recovery of the bleach.

The interaction of an optimized chirped pulse with a molecule embedded in a solvent has been investigated in the study presented in the last part of the thesis. The study was aimed at gaining insight on the interplay between the pulse parameters and the molecular response, which leads to minimal excitation and maximal transmission. This task was carried out by setting simulations which included light-matter interaction in an explicit fashion. The closed-loop feedback strategy has been employed to find the optimal field. The effect of the dissipation on the optimized solutions has been investigated, and the results of the simulations were compared to the experimental data.

In this thesis the Surrogate Hamiltonian has been developed as an efficient and practical tool. It has shown the ability to treat strongly driven chemical systems consistently, including the system-bath correlations and the influence of electromagnetic fields. The numerical extension of the Surrogate Hamiltonian beyond one dimension allows the treatment of realistic chemical systems with nonadiabatically

coupled potential energy surfaces. The random-phase thermal wavefunction enables numerical simulations at a wider range of temperatures. The limitation of the Surrogate Hamiltonian to short times can be overcome by its combination with the semi-group approach. The combined method enables us, in principle, to simulate long-time dynamics, approaching equilibrium.

Contents

Chapter 1

Prologue

With the development of ultrashort lasers, chemists became able to probe the dynamics of molecules on the time scale of nuclear motion, which opened the door for elucidating chemical reactions in a "real-time" regime [1, 2]. Novel experimental techniques, however, only emphasize a crucial need in extensive theoretical tools for interpretation and prediction of experimental data.

Successful theoretical simulations of ultrafast molecular dynamics are based on quantum time-dependent wavepacket calculations [3–6]. The solution of the Schrödinger equation provides a complete dynamical picture of a pure quantum-mechanical state. This description is satisfactory for isolated molecules in the gas phase. However, when experiments involve processes taking place in condensed-phase environments, the fully quantum description of such systems remains a challenging task. The main obstacle is rooted in the exponential growth in complexity with the number of degrees of freedom.

Significant simplifications may be achieved by partitioning the total many-body system into a primary part and a bath describing the environment [7]. The primary system consists of a few physically relevant degrees of freedom, which are probed experimentally and treated explicitly. The bath, on the other hand, consists of a large or even infinite number of degrees of freedom and enters the model implicitly, i.e. only its influence on the primary system is addressed. The separability between a system and an environment is not trivial. From an experimental point of view it is based on an assumption that one can probe the degrees of freedom of the primary system solely, without affecting directly the degrees of freedom of the environment.

The theory demands a clear operational decomposition into a well-defined primary system and a stable reservoir [8, 9].

Let us consider a combined system with following Hamiltonian:

$$\hat{\mathbf{H}} = \hat{\mathbf{H}}_S \otimes \mathbb{1}_B + \mathbb{1}_S \otimes \hat{\mathbf{H}}_B + \hat{\mathbf{H}}_{SB} + \hat{\mathbf{H}}_{SF}(t) \ , \tag{1.1}$$

where $\hat{\mathbf{H}}_S$ is the Hamiltonian of the primary system, $\hat{\mathbf{H}}_B$ - the bath Hamiltonian and $\hat{\mathbf{H}}_{SB}$ describes the interaction between the system and the bath. The time-dependent interaction of the system with the external electromagnetic field is represented by $\hat{\mathbf{H}}_{SF}(t)$.

It is assumed that the combined system-bath is closed, and therefore its dynamics are generated by a unitary evolution:

$$\hat{\boldsymbol{\rho}}(t) = \hat{\mathbf{U}}(t)[\hat{\boldsymbol{\rho}}_S(0) \otimes \hat{\boldsymbol{\rho}}_B(0)]\hat{\mathbf{U}}^{+}(t) \ , \tag{1.2}$$

where $\hat{\mathbf{U}}(t) = e^{-i\hat{\mathbf{H}}t/\hbar}$ is the time-evolution operator of the total system. The dynamics of the primary system, however, are no longer unitarian and the interaction with the environment creates system-bath correlations. Interaction with the environment leading to energy relaxation and dephasing is often described by the term *quantum dissipation*.

1.1 Methods to treat quantum dissipation

A considerable number of methods to treat "system plus bath" models have been proposed in recent years [7]. Here is a short review of different approaches to the problem of quantum dissipation

Since the combined dynamics are not feasible in most cases, many attempts have been made to develop a simpler description in a reduced state space. The reduced dynamics approaches are constructed to avoid the size scaling of a full treatment. The equations of motion are derived for the reduced density operator $\hat{\boldsymbol{\rho}}_S = \mathsf{tr}_B\{\hat{\boldsymbol{\rho}}\}$, obtained as a partial trace over the bath degrees of freedom.

Following the Nakajima-Zwanzig projector formalism [10–13], the dynamics of the reduced density matrix $\hat{\boldsymbol{\rho}}_S$ is given by a closed integro-differential equation:

$$\frac{d}{dt}\hat{\boldsymbol{\rho}}_S = -\frac{i}{\hbar}\,\mathcal{L}_S(\hat{\boldsymbol{\rho}}_S) - \int^t \mathcal{K}(\tau)\hat{\boldsymbol{\rho}}_S(t-\tau)d\tau \ , \tag{1.3}$$

where $\mathcal{L}_S$ is the system's free Liouville operator and $\mathcal{K}$ is an environment memory kernel. Although the Nakajima-Zwanzig equation is formally exact, it is of little practical use, since the memory kernel cannot be calculated. The equation serves, therefore, as the basis for further approximations.

An important class of approximate quantum dissipative methods is based on two main assumptions: firstly, that the system-bath interaction is weak and therefore it can be considered up to a second order (Born approximation), and secondly, that the bath memory time scale is extremely short compared to any appropriate time scale within the system (Markov approximation). Under these conditions one can derive a Markovian quantum master equation (QME) of the Bloch-Redfield type [14–20] and its generalization [21–26].

The assumption of a weak system-bath coupling restricts the range of phenomena that can be treated with QMEs, especially in condensed phase systems.

To overcome the restriction of the second order QME caused by the weak-coupling approximation, the high order QMEs [27–29] have been derived and applied mostly to the spin-boson problem. However, the fact that the system-bath coupling is given in terms of multi-time correlation functions makes the computational implementation of this scheme difficult. Strategies for calculating memory kernel, that do not resort to the assumption of weak system-bath coupling have also been proposed [30–32].

On the other hand, to model dynamics of quantum systems, which are subject to a strong, short electromagnetic field, the Markovian approximation should be abandoned. A number of methods to modify the Redfield theory beyond of Markovian approximation have been proposed [33–37]. A method developed by Meier and Tannor [38], for example, uses a special parametrization of the bath spectral density, leading to a set of coupled Markovian equations for the reduced density matrix and auxiliary density matrices, which incorporate the memory effects. The number of needed auxiliary density matrices depends on the coupling strength and temperature, and for low temperature the calculations become numerically demanding. While the method is not restricted to a specific form of the system-bath coupling, it does consists of the weak-coupling assumption.

The method can treat time-dependent interactions explicitly and includes initial

correlations between the system and the bath. The latter is of particular importance, since most of the reduced description approaches accept the factorization of the initial state $\hat{\boldsymbol{\rho}}_S(0) \otimes \hat{\boldsymbol{\rho}}_B(0)$. This widely used assumption of an initially uncorrelated system-bath state is not consistent with most experimental situations, and has been criticized in a number of works [26, 39–41].

An alternative approach for modeling the reduced dynamics, formally referred to as semigroup analysis, was introduced by Lindblad [42] along with Gorini, Kossakowski and Sudarshan [16, 43]. This dynamical semigroup approach is based on the Markovian assumption augmented by a condition that the time evolution operator of the quantum mechanical system generates a completely positive dynamical semigroup [16, 44]. The complete positivity condition physically means that populations can never become negative. Lindblad determined the general form that all reduced dynamical equations must take:

$$\frac{d}{dt}\hat{\boldsymbol{\rho}}_S = -\frac{i}{\hbar}\,[\hat{\mathbf{H}}_S, \hat{\boldsymbol{\rho}}_S] + \sum_j \left(\hat{\mathbf{F}}_j \hat{\boldsymbol{\rho}}_S \hat{\mathbf{F}}_j^+ - \frac{1}{2}\{\hat{\mathbf{F}}_j \hat{\mathbf{F}}_j^+, \hat{\boldsymbol{\rho}}_S\} \right) . \tag{1.4}$$

The Lindblad operators $\hat{\mathbf{F}}_j$'s are bound operators acting on the Hilbert space of the system. The nature of the bath is implied in the formulation of a specific Lindblad operator, which can be chosen to fit some phenomenological requirements or can be derived from the full Hamiltonian. Such operators that can be constructed to describe different relaxation and dephasing processes and parameters, entering into the equation, can be obtained in a weak coupling limit, using perturbation theory [8, 45–47]. The semigroup approach is intrinsically quantum-mechanical and follows directly from a physical picture of dissipation. However, the method is based on the Markovian assumption, and therefore restricted to problems, in which the separation of time scales between the system and the bath is possible.

Based on the semigroup approach, a number of methods have been developed in order to include bath memory effects. In particular, Percival et al. have developed a nonlinear stochastic Schrödinger equation approach using Monte Carlo methods [48, 49], and recently the method has been extended to treat non-Markovian situations [50–56].

An alternative formulation of system-bath dynamics is based on the path integral description of quantum mechanics [57], and introduces the influence of the bath

in terms of the Feynman-Vernon influence functional [58]. For a linearly coupled harmonic oscillator bath the exact influence functional can be obtained in a closed form [59–61]. The application of real-time path integrals has been limited due to the "dynamical sign problem": the numerous path contributions are interfering with each other, producing partial cancellations, which lead to numerical instabilities. Several numerical methods based on the path integral formulation have been developed, including the optimized Monte Carlo simulation method [62, 63], a path class summation approach [64] and "interacting-blip chain" approximation [65]. Accurate long-time path integral calculations have become possible with the development of iterative tensor quasiadiabatic propagators by Makri and co-workers [66–69].

The numerical evaluation of the multi-dimensional integral nevertheless is computationally challenging, which limits the applications of path integral methods to relatively simple systems, linearly coupled to the bath. Finally, mapping the bath Hamiltonian onto a harmonic one is questionable for energy relaxation and dephasing of molecules in the liquid phase or on solids.

However, the fact that path integral results are numerically exact and that all approximation are made when specifying the Hamiltonian makes path integral calculations a popular benchmark for newly developed methods [70, 71].

Almost all the approaches mentioned above, treat the environment within the linear response regime as a bath of harmonic oscillators. Thus the influence of the bath enters as the bath correlation function. Several methods have been proposed for calculating bath correlation functions, based on a mixed quantum-classical treatment [72, 73], analytical continuation [74–77], centroid molecular dynamics [78–80], quantum mode coupling theory [81,82], and the semiclassical approximation [83–87]. The difficulty is that practically only classical and semi-classical methods exist for calculating correlation functions.

Despite the great progress in the field of quantum dissipation over the last few decades, there is still a strong need for the development of efficient theoretical tools to treat quantum dissipative processes. Ultra-fast pump-probe experiments allow a real time resolution of chemical processes in condensed-phase environments. The interpretation of these experiments remains a challenging problem and strongly depend on theoretical support. Theoretical models able to describe consistently all aspects

of ultra-fast experiments in a condensed-phase, are absent. The requirements for such methods include the ability to treat non-Markovian dynamics without the restriction of a weak system-bath coupling, an explicit treatment of a time-dependent field and its influence on the system-bath interactions. Non-harmonic baths with an ab-initio calculated system-bath coupling are highly desirable.

1.2 Motivation and objectives of the research

The Surrogate Hamiltonian method [88] has been developed to simulate ultrafast quantum dynamical processes for systems embedded in a bath. The method is based on constructing a surrogate *finite* system-bath Hamiltonian, that in the limit of an infinite number of bath modes reproduces the true dynamics of the system. This is done by renormalizing the system-bath interaction term in the Surrogate Hamiltonian. Since within a finite interval of time the system is not able to access the actual full complexity of the bath, it is sufficient to replace the bath modes by a finite set, which mimics the full dynamics for a finite time (shorter than the Poincaré period at which recurrences appear [15]). Employing a finite Hamiltonian makes the proposed method particularly suitable for ultrafast processes.

The Surrogate Hamiltonian method is not Markovian and differs from the Redfield [18,19] or semigroup treatments [16,42,43]. It is close in spirit to real time path integral techniques and the MCTDH method [89–92], which includes the environmental degrees of freedom explicitly. The MCTDH method employs the combined system-bath wavefunction expanded in a basis of time-dependent configurations, and describes the dynamics of the complete system.

Similarly, the Surrogate Hamiltonian method requires to solve the time-dependent Schrödinger equation of the combined system rather than the Lioville von Neumann equation of the reduced density matrix. As a result, the method is able to start with a fully correlated initial state, and the treatment of time-dependent external fields poses no problem. The method is not restricted to special forms of system-bath coupling, and formally, no weak coupling assumption is employed.

The applications of the Surrogate Hamiltonian method include dissipative processes taking place on metal surfaces [88, 93, 94] and ultrafast charge transfer pro-

cesses in condensed matter [95, 96]. While the method has already been established as a practical tool, a number of aspects, which have yet to be addressed, served as a motivation for the research summarized in this thesis.

The Surrogate Hamiltonian method employs a bath of two-level systems, which acts as a spin bath [97–101]. The quantum properties of such a bath are different from the widely used bath of harmonic oscillators. The bath modes of the linearly driven harmonic bath are uncorrelated. In the spin bath even a linear coupling to the primary system induces quantum entanglement between different spins inside of the bath. The latter makes a spin bath a more appropriate candidate to treat quantum phenomena, than a nearly classical harmonic bath.

While a harmonic bath is natural for systems interacting with the radiation field [102], it has also been applied to less favorable scenarios such as energy relaxation and dephasing of molecules in a liquid phase or on solid surfaces. In these cases a strong coupling or interactions with a low-temperature environment may cause large system-bath correlations, and will therefore result in a failure of the Markovian approximation, as well as the assumption of the weak system-bath coupling.

In this context, our study is aimed to elucidate the differences between two kinds of baths. In the limit of weak coupling, it has been shown that the two baths are equivalent [97–99]. The limiting coupling strength - where the dynamics induced by the two baths differ - has not yet been characterized. It is valuable to know how the fundamental differences between the two kinds of bath are reflected in the dynamics of the primary system, if at all.

The ultimate goal of theoretical simulations based on the Surrogate Hamiltonian approach is to achieve a comprehensive description of realistic experimental systems. For that purpose the extension of the method to finite-temperature situation is required. The application of the method has been restricted to the low-temperature regime due to unfavorable computational scaling. For finite temperatures thermal averaging requires computing the large number of eigenstates and then repeating the propagation step for each initial state. The number of eigenfunctions required grows with temperature, and what is more important, it grows exponentially as the number of bath modes increases. The prohibitive scaling of numerical effort used in the Surrogate Hamiltonian method is behind the motivation for developing an

alternative scheme for thermal averaging.

The Surrogate Hamiltonian method allows the analysis of multidimensional systems without restricting the potential shape. The early applications of the method [88,93–96] have been limited to a primary system with one nuclear degree of freedom coupled to a dissipative environment. However, the chemistry of numerous systems involves nuclear dynamics on few nonadiabatically coupled potential energy surfaces. The most complicated nonadiabatic processes involve conical intersections [103,104]. These processes are intrinsically quantum-mechanical and extremely sensitive to the landscape of the potentials involved [105] The influence of the dimensionality on nonadiabatic transitions has been widely acknowledged [106–109]. The numerical extension of the Surrogate Hamiltonian beyond one dimension is necessary in order to treat realistic chemical systems with nonadiabatically coupled potential energy surfaces. The ultrafast time scale of the internal-conversion process, often associated with the existence of conical intersections, make the Surrogate Hamiltonian well-suited for the treatment of such systems.

The special emphasis of our study is placed on introducing time-dependent observables, which are the direct signature of the ultrafast dynamics measured in the typical pump-probe experiments. The use of the Surrogate Hamiltonian method has an advantage of a consistent treatment of initial correlations between the system and the bath, as well as the ability to describe the pulse field and its influence on the system-bath interaction explicitly. The non-perturbative approach allows us to directly simulate the dynamics induced by the pump pulse. Considering spectroscopic observables, such as transient absorption and emission, enables reproduction of all qualitative features of ultrafast pump-probe experiments.

Since optimization techniques have become an integral part of modern experiments, it is inevitable to include them in our model. It is important to check the capability to design control strategies in the presence of dissipation. Despite some attempts [110–112] there is a shortage of methods able to treat control systems in the presence of a dissipative environment. The ability of the Surrogate Hamiltonian method to treat time-dependent fields in a non-perturbative manner is a clear advantage over other approaches, particularly reduced dynamical ones.

1.3 Outline of the thesis

The presented thesis is based on the publications listed in **Appendix E** and is organized as follows: The Surrogate Hamiltonian method is introduced in **Chapter 2** and the possible dissipative processes are discussed. **Chapter 3** contains a numerical comparison between a spin bath employed by the Surrogate Hamiltonian approach, and a harmonic bath. The dissipative quantum dynamics of an anharmonic oscillator coupled to a bath is studied with the purpose of elucidating the differences between the relaxation to a spin bath and to a harmonic one.

The application of the method to the finite-temperature problems is discussed in **Chapter 4**. A new scheme for calculating thermally averaged observables, based on random phase thermal wavefunctions is presented. The method is tested for the model of Morse oscillator in equilibrium with an ohmic bath, perturbed by a short pulse.

In **Chapter 5** the method is applied to a dissipation taking place in a multidimensional system, which includes conical intersections. A model system consisting of two vibronically coupled electronic states with two nuclear degrees of freedom is considered. The dissipation is treated by two different methods, Lindblad semigroup formalism and the Surrogate Hamiltonian approach. Pump-probe experimental expectation values such as transient emission and transient absorption are calculated and compared to the adiabatic and diabatic population transfer.

Chapter 6 discusses an application of the Surrogate Hamiltonian method to a problem of optimal control. Optimal control theory is employed for the task of minimizing the excited-state population of a dye molecule in solution. The closed-loop feedback strategy is employed to find the optimal field. The control task is solved for the combined system, including the excited molecule immersed in a finite, but large environment. The latter may cause both vibrational and electronic dephasing, as well as vibrational relaxation - processes that have a time scale comparable to the pulse duration. The study investigates the influence of the experimental control parameters, such as pulse fluence and chirp, on the induced dynamics.

Finally, some concluding remarks are made in **Chapter 7**. Numerical details are presented in **Appendices A-D**.

Atomic units are employed throughout the thesis unless otherwise stated.

Chapter 2

The Surrogate Hamiltonian method

The Surrogate Hamiltonian method [88] is based on the idea that for sufficiently short times the system is not able to resolve the full density of the bath states. Therefore it is possible to replace an infinite number of the bath modes by a finite set of representative modes:

$$\hat{\mathbf{H}}_B \sim \sum_{k=1}^{\infty} \hat{\tilde{\mathbf{n}}}_k^{\mathsf{true}} \longrightarrow \sum_{k=1}^{N} \hat{\mathbf{n}}_k^{\mathsf{rep}} \,, \tag{2.1}$$

This new "surrogate" Hamiltonian faithfully represents the dynamics of the primary system under the influence of an infinite bath for a *finite* time. The method then requires to solve the time-dependent Schrödinger equation of the combined system and the bath instead of the Liouville von Neumann equation.

In the limit of an infinite number of bath modes, the Surrogate Hamiltonian is completely equivalent to the original, "true" Hamiltonian. Since, at least in principle, the number of modes N can be increased, it is possible to check convergence.

The truncation leading to the Surrogate Hamiltonian, Eq. (2.1), relies on a time-energy uncertainty argument: In a finite time, $t \ll \infty$, the system can only resolve a finite number, $N \ll \infty$, of bath states and not the full density of states of the bath. The sampling density in energy of the finite set of bath states is determined by the inverse of the time interval. This argument leads to two observations – the Surrogate Hamiltonian is well-suited for the description of ultrashort events, and the number of needed modes increases with the interaction strength between system and bath.

Strong and intermediate coupling strengths might therefore pose a computational challenge. From the above derivation, it is clear, however, that no weak coupling assumption was needed. In addition, and this is the major difference to standard approaches, and therefore the major advantage, the Surrogate Hamiltonian method yields a controllable approximation.

The two level system (TLS) bath is described by the Hamiltonian

$$\hat{\mathbf{H}}_B = \mathbb{1}_S \otimes \sum_i \varepsilon_i \hat{\boldsymbol{\sigma}}_i^+ \hat{\boldsymbol{\sigma}}_i \tag{2.2}$$

with $\hat{\mathbf{n}}_i = \hat{\boldsymbol{\sigma}}_i^+ \hat{\boldsymbol{\sigma}}_i$ the occupation number operator and ε_i the energy of the ith bath mode. $\mathbb{1}_S$ denotes the identity in the Hilbert space $\mathcal{H}_S$ of the system, i.e. $\hat{\mathbf{H}}_B$ acts on the total Hilbert space $\mathcal{H}_S \otimes \mathcal{H}_B$. For N bath modes the Hilbert space $\mathcal{H}_B$ of the bath has dimension 2^N. This results from a single TLS or spin-$\frac{1}{2}$ being defined on a two-dimensional Hilbert space and the possibility to combine each of the two basis states for all N modes. The dimension of the total Hilbert space $\mathcal{H}_S \otimes \mathcal{H}_B$ is then given by the product of the dimensions of $\mathcal{H}_S$ and 2^N. If, for example, the state of the system is described by a wave function represented on a grid and the dimension of the grid is N_g, the state of the total system is described by 2^N N_g-dimensional wave functions. Obviously, this dimension quickly gets very large when the number of bath modes N is increased. However, considering all 2^N possibilities of combining the bath modes corresponds to considering *all* possible system-bath correlations which might not be necessary. The number of simultaneously allowed excitations can then be restricted. In an extreme case, only single excitations are considered. This reduces the dimension of the total Hilbert space from 2^N to $N+1$. The approximation made can again be checked by increasing the number of simultaneously allowed excitations, i.e. it is controllable.

The basis of the TLS Hilbert space was chosen to be the spin-down and spin-up states. Spin-up corresponds to the TLS being excited while for spin-down the TLS is deexcited. This representation proved to be particularly useful, since the index labeling the 2^N components of the wave function contains the information of the TLS being excited or deexcited, respectively.

There are two possibilities to look at the TLS bath. So far it has been introduced in its own right, assuming the eigenvalues ε_i and eigenstates n_i have been obtained in a prediagonalization of the bath. However, a TLS can also be thought of as

a low temperature approximation to a harmonic oscillator. At low temperature, only the ground and first excited state of a harmonic oscillator should be significantly populated. The TLS bath can therefore be viewed as a low temperature approximation to a harmonic oscillator bath, and the parameters of the two can be connected. In particular, the role of the spectral density for the TLS bath should become clear. This approach has been pursued when the Surrogate Hamiltonian was first introduced [88] and it shall briefly be reviewed here.

The starting point is the Heisenberg equations of motion for the primary system. For simplicity, the primary system is taken to be one-dimensional with the Hamiltonian:

$$\hat{\mathbf{H}}_S = \hat{\mathbf{T}} + V(\hat{\mathbf{Q}}) = \frac{\hat{\mathbf{P}}^2}{2m} + V(\hat{\mathbf{Q}}) \; . \tag{2.3}$$

A generalization to more nuclear degrees of freedom is straightforward, and the treatment of more than electronic ground state dynamics will be discussed in the following sections. The interaction between system and bath can be decomposed into a sum of products of system and bath operators without loss of generality [22,113],

$$\hat{\mathbf{H}}_{SB} = f(\hat{\mathbf{Q}}) \otimes \sum_i \hat{\mathbf{V}}_i \tag{2.4}$$

with Hermitian operators $\hat{\mathbf{V}}_i$ acting on the bath Hilbert space. The $\hat{\mathbf{V}}_i$ can be written in terms of creation and annihilation operators, for simplicity real coupling matrix elements and a linear combination of creation and annihilation operators are assumed. The interaction Hamiltonian is then given by

$$\hat{\mathbf{H}}_{SB} = f(\hat{\mathbf{Q}}) \otimes \sum_i V_i \left(\hat{\mathbf{A}}_i^+ + \hat{\mathbf{A}}_i \right) \; , \tag{2.5}$$

where $\hat{\mathbf{A}}_i^+$ and $\hat{\mathbf{A}}_i$ are creation and annihilation operators, respectively, of an abstract bath mode i. The interaction is characterized by the coupling function $f(\hat{\mathbf{Q}})$ and coupling constants V_i. The Heisenberg equations of motion for the system are then given by

$$\begin{aligned} \frac{\mathsf{d}}{\mathsf{d}t}\hat{\mathbf{Q}} &= \frac{\hat{\mathbf{P}}}{m} \, , \\ \frac{\mathsf{d}}{\mathsf{d}t}\hat{\mathbf{P}} &= -\frac{\mathsf{d}}{\mathsf{d}\hat{\mathbf{Q}}} V(\hat{\mathbf{Q}}) - \frac{\mathsf{d}}{\mathsf{d}\hat{\mathbf{Q}}} f(\hat{\mathbf{Q}}) \otimes \sum_i V_i \left(\hat{\mathbf{A}}_i^+ + \hat{\mathbf{A}}_i \right) \; . \end{aligned} \tag{2.6}$$

For infinitely many modes, the sum in Eq. (2.6) can be replaced by an integral, $\sum_i \longrightarrow \int \mathsf{d}\varepsilon\rho(\varepsilon)$,

$$\sum_i V_i \left(\hat{\mathbf{A}}_i^+ + \hat{\mathbf{A}}_i\right) = \int \mathsf{d}\varepsilon\rho(\varepsilon)\sqrt{J(\varepsilon)}\left(\hat{\mathbf{a}}^+(\varepsilon) + \hat{\mathbf{a}}(\varepsilon)\right) , \tag{2.7}$$

where the density of states $\rho(\varepsilon)$ and the spectral density $J(\varepsilon)$ of the bath have been introduced. The creation operators are related by

$$\hat{\mathbf{a}}^+(\varepsilon) = \frac{1}{\sqrt{J(\varepsilon)}} \sum_i V_i \hat{\mathbf{A}}_i^+ \delta(\varepsilon - \varepsilon_i) , \tag{2.8}$$

and an analogous equation holds for the annihilators. The new operators $\hat{\mathbf{a}}^+(\varepsilon)$, $\hat{\mathbf{a}}(\varepsilon)$ can be viewed as creator and annihilator, respectively, of an interaction mode. They enter the new, *Surrogate* Hamiltonian describing the combined system,

$$\begin{aligned} \hat{\mathbf{H}}_{Surr} = \hat{\mathbf{T}} + V(\hat{\mathbf{Q}}) + \int \mathsf{d}\varepsilon\rho(\varepsilon)\,\varepsilon\,\hat{\mathbf{a}}^+(\varepsilon)\hat{\mathbf{a}}(\varepsilon) \\ + f(\hat{\mathbf{Q}}) \int \mathsf{d}\varepsilon\rho(\varepsilon)\sqrt{J(\varepsilon)}\left(\hat{\mathbf{a}}^+(\varepsilon) + \hat{\mathbf{a}}(\varepsilon)\right) . \end{aligned} \tag{2.9}$$

If the spectral density is of finite support $[\varepsilon_0, \varepsilon_{cut}]$, the integrals in Eq. (2.9) can be sampled by a finite number of energies, $N \ll \infty$. In the limit $N \to \infty$ the full system-bath dynamics is then recovered. The finite sampling ε_i, $i = 0, \ldots, N-1$ specifies the energies at which creation and annihilation operators are defined,

$$\hat{\mathbf{a}}_i^+ = \hat{\mathbf{a}}^+(\varepsilon_i) , \qquad \hat{\mathbf{a}}_i = \hat{\mathbf{a}}(\varepsilon_i) \tag{2.10}$$

and

$$v_i \hat{\mathbf{a}}_i^+ \rho(\varepsilon_i) = \sqrt{J(\varepsilon_i)}\hat{\mathbf{a}}^+(\varepsilon_i) , \qquad \text{and} \quad \text{c.c.} \tag{2.11}$$

The interaction of mode i with the system is then given by

$$v_i = \sqrt{J(\varepsilon_i)/\rho(\varepsilon_i)} . \tag{2.12}$$

A similar procedure to obtain the coupling constants is followed in [84]. The discretized Surrogate Hamiltonian then reads [88]

$$\hat{\mathbf{H}}_{Surr} = \hat{\mathbf{T}} + V(\hat{\mathbf{Q}}) + \sum_{i=0}^{N-1} \varepsilon_i \hat{\mathbf{a}}_i^+ \hat{\mathbf{a}}_i + f(\hat{\mathbf{Q}}) \otimes \sum_{i=0}^{N-1} v_i \left(\hat{\mathbf{a}}_i^+ + \hat{\mathbf{a}}_i\right) . \tag{2.13}$$

The spectral density $J(\varepsilon)$ enters the above expressions, Eq. (2.7) and Eq. (2.8) as a normalization factor. Unfortunately, as no unique definition of the spectral

density exists, some care must be devoted to ensure the same definition is used when comparing different methods. For the harmonic oscillator bath, the spectral density is introduced as Fourier transform of the bath correlation function [22,102]. The definition of spectral density is chosen to include the density of states [84,102],

$$J(\varepsilon) = \sum_i |V_i|^2 \delta(\varepsilon - \varepsilon_i) \ . \tag{2.14}$$

The meaning of spectral density then becomes obvious: It is the system-bath coupling weighted by the density of states, i.e. it specifies the effective interaction. The influence of the bath on the system is thus fully characterized by $J(\varepsilon)$.

The sampling density in energy of this set is determined by the inverse of the time interval. The finite bath of N spins is constructed with a system-bath coupling term, which in the limit $N \to \infty$ converges to the given spectral density of the full bath. The Surrogate Hamiltonian, consists of a finite number of bath modes, and it is therefore limited to representing the dynamics of the investigated system for a finite time (shorter than the Poincaré period at which recurrences appear [15]). These recurrences are caused by the finite size of the bath so that after some time the energy flow into the bath partly is reversed.

Eq. (2.13) and Eq. (2.12) or Eq. (2.13) together with a microscopic model for the interaction are the starting point of the simulations. Since TLS are used as bath modes, the abstract operators $\hat{\mathbf{a}}_i^+$, $\hat{\mathbf{a}}_i$ are replaced by TLS or spin operators $\hat{\boldsymbol{\sigma}}_i^+$, $\hat{\boldsymbol{\sigma}}_i$.

Within the Surrogate Hamiltonian method, it is straightforward to introduce into the model different system-bath interaction mechanisms, such as electronic and vibrational pure dephasing. The process of dephasing corresponds physically to fluctuations in the values of the system energies - electronic dephasing is then the fluctuation in the electronic energy levels, while vibrational dephasing describes changes in the vibrational energies. A qualitative picture of pure dephasing is based on an almost elastic exchange of energy between bath modes, which alters the accumulated phase of the system. For electronic dephasing (the primary system consists of two electronic states), the bath modulates the electronic excitation:

$$\hat{\mathbf{H}}_{SB}^{ed} = \Delta_V(\hat{\mathbf{Q}}) \frac{1}{2} \begin{pmatrix} -1 & 0 \\ 0 & 1 \end{pmatrix} \otimes \sum_{ij} c_{ij}^{ed} (\hat{\boldsymbol{\sigma}}_i^+ \hat{\boldsymbol{\sigma}}_j + \hat{\boldsymbol{\sigma}}_j^+ \hat{\boldsymbol{\sigma}}_i) \ . \tag{2.15}$$

$\Delta_V(\hat{\mathbf{Q}})$ is the difference potential describing the dependence of the modulation on

the nuclear displacement. The coefficients c_{ij} are biased to represent almost elastic encounters,

$$c_{ij} = \bar{c}_e \, \mathsf{e}^{-\frac{(\varepsilon_i - \varepsilon_j)^2}{2\sigma_\varepsilon^2}} \ , \tag{2.16}$$

with $\bar{c}_e$ a global dephasing parameter, and σ_ε determines the inelastic width. The dephasing rate is proportional to the square of the band width of c_{ij} [95].

For vibrational dephasing, the bath modulates the vibrational Hamiltonian:

$$\hat{\mathbf{H}}_{SB}^{vd} = \begin{pmatrix} \hat{\mathbf{H}}_g & 0 \\ 0 & \hat{\mathbf{H}}_e \end{pmatrix} \otimes \sum_{ij} c_{ij}^{vd} (\hat{\boldsymbol{\sigma}}_i^+ \hat{\boldsymbol{\sigma}}_j + \hat{\boldsymbol{\sigma}}_j^+ \hat{\boldsymbol{\sigma}}_i) \ . \tag{2.17}$$

In order to activate a pure dephasing process, the bath modes must be initially populated. The detailed algorithm of applying Eqs.(2.17-2.15) has been described in Ref. [95] and is briefly reviewed in Appendix B.

The full Surrogate Hamiltonian contains all possible correlations between the primary system and the environment. The combined system-bath state is described by a 2^N dimensional spinor $\Psi(\hat{\mathbf{Q}}, \hat{\boldsymbol{\beta}}_1, \ldots, \hat{\boldsymbol{\beta}}_{2^N})$ with N being the number of bath modes. The spinor is bit ordered, i.e., the jth bit set in the spinor index corresponds to the jth TLS mode, which is excited if the counting of bits starts at $j = 0$. The dimension 2^N results from the total number of possibilities to combine two states N times.

Thus the total wave function can be written as

$$\begin{aligned} |\Psi(\hat{\mathbf{Q}}, \{\hat{\boldsymbol{\beta}}_\mathbf{j}\})\rangle = a_0 |\phi_0(\hat{\mathbf{Q}})\rangle + \sum_{j=0}^{\binom{N}{1}} a_j |\phi_j(\hat{\mathbf{Q}})\rangle \\ + \sum_{j,k=0}^{\binom{N}{2}} a_{jk} |\phi_{jk}(\hat{\mathbf{Q}})\rangle \ + \ldots \ , \end{aligned} \tag{2.18}$$

where $|\phi_j(\hat{\mathbf{Q}})\rangle = (0, \ldots, \phi_j(\hat{\mathbf{Q}}), \ldots, 0)^T$ is a singly-excited spinor,
$|\phi_{jk}(\hat{\mathbf{Q}})\rangle = (0, \ldots, \phi_j(\hat{\mathbf{Q}}), \ldots, \phi_k(\hat{\mathbf{Q}}), \ldots, 0)^T$ is a doubly-excited spinor and so on. The jth component corresponds to the jth TLS being excited.

However, considering all 2^N possibilities of combining the bath modes might not be necessary in a weak coupling limit. In this case, for short time dynamics, it is possible to restrict the number of simultaneous bath excitations [96]. As an extreme example, only single excitations might be considered. If one restricts the number of simultaneous excitations, the dimension of the spinor becomes the sum of binomial

coefficients $\sum_{k=0}^{N_{exc}} \binom{N_{exc}}{k}$ with N_{exc} the number of simultaneous excitations. The construction is similar to the configuration-interaction (CI) approach in electronic structure theories. The restriction of simultaneously allowed excitations leads to significant numerical savings and its validity can be checked by increasing N_{exc}.

Observables associated with operators of the primary system are determined from the reduced system density operator: $\hat{\boldsymbol{\rho}}_S(Q,Q') = \mathsf{tr}_B\{|\Psi\rangle\langle\Psi|\}$, where $\mathsf{tr}_B\{\ \}$ is a partial trace over the bath degrees of freedom. The system density operator is constructed from the total system-bath wave function and only this function is propagated. The explicit construction of the reduced density operator is only necessary if the operator corresponding to the desired observable is not diagonal in coordinate space.

A grid representation is used to represent each spinor component of the wave function. The kinetic energy operator is applied in Fourier space employing FFT [4], and the Chebychev method [3, 114] is used to compute the evolution operator (Cf. Appendix A). Numerical details for applying the bath operators are described in Appendix B.

A fully correlated initial state is easily obtained in the Surrogate Hamiltonian method. Once the system-bath Hamiltonian $\hat{\mathbf{H}}$ is set, the correlated ground state can be determined by propagating an initial guess wave function in imaginary time using $\hat{\mathbf{H}}$ [114]. By employing a filter-diagonalization method [115–117] other eigenstates are extracted directly. Thermal observables can be obtained by Boltzmann weighting the result from individual calculations for pure states (the procedure of calculating thermal observables is discussed in Chapter 4).

So far the general idea of the Surrogate Hamiltonian has been discussed. The new directions and further development of the method are presented in the next two chapters.

Chapter 3

Comparison between spin and harmonic baths

The Surrogate Hamiltonian method implements the bath consisting of two-level systems, which acts as a spin bath [97–101]. However, a bath composed of a set of noninteracting harmonic oscillators is the one most widely used. The idea originates from a normal mode analysis combined with a weak system-bath coupling assumption [58]. If the bath is only weakly perturbed by the system, it can be considered linear, and therefore described as a collection of harmonic oscillators.

Such a bath is natural for systems interacting with the radiation field [102]. The harmonic bath model has also been applied to less favorable scenarios such as energy relaxation and dephasing of molecules in the liquid phase or on the solid surfaces. In these cases a strong coupling or interactions with a low-temperature environment may cause large system-bath correlations, and will therefore result in a failure of the both Markovian and Born approximations. To overcome such difficulties in the dynamics of molecules that are in intimate interaction with an environment, the Surrogate Hamiltonian method has been developed.

The origins of the spin and harmonic baths are different. The harmonic bath is closely related to a normal mode decomposition. Once this is done the spectral density function is able to completely determine the relaxation dynamics. From a computational point of view the determination of the spectral density is a major task. The most popular working procedure is to extract it from classical mechanics [118]. The drawback is that this procedure assumes harmonic modes and a linear

system bath coupling term. The spin bath has its origin in a tight binding model of condensed phase. This can also become a simulation procedure if the parameters of the tight binding model can be estimated from first principles [94].

The purpose of this part of our study is to compare the performance of the two baths in a simple system composed of a primary anharmonic oscillator coupled to a multi-mode bath. In the limit of weak system-bath coupling, it has been shown that the two baths are equivalent. For finite temperature the equivalence requires a rescaling of the spectral density function which determines the coupling of the primary system to the different bath modes [97–99]. The limiting coupling strength where the dynamics induced by the two baths differ has not yet been characterized. For stronger coupling strength, the ergodic behavior of the two baths should be different. The bath modes of the linearly driven harmonic bath are uncorrelated. In the spin bath the coupling to the primary system induces quantum entanglement between the different modes. It is valuable to know how this fundamental difference influences the dynamics of the primary system.

Our comparative study is based on a numerical model of a system coupled to a bath, with a large but finite number of modes. For a finite interval of time determined by the inverse of the energy level spacing, the finite bath mimics exactly a bath with an infinite number of modes. For this interval the primary system cannot resolve the full density of states of the bath. By renormalizing the system-bath interaction term to the density of states, the finite bath faithfully represents the infinite bath up to this time limit.

The dynamics of the primary oscillator coupled to the harmonic bath has been recently calculated based on the multi-configuration time dependent Hartree approximation (MCTDH) [119, 120]. The authors were able to show that for a Morse oscillator coupled to a bath, converged results could be obtained for a bath consisting of 60 modes to a time scale of 3 ps. The present study utilized the same system and system-bath coupling parameters, but employed a spin bath in the context of the Surrogate Hamiltonian. The comparison allows an evaluation of the similarities and differences between the two descriptions. Once the differences are identified, it becomes possible to modify the Surrogate Hamiltonian bath to extend the realm of similarity.

In the weak coupling limit the numerical study of Nest and Meyer [119] was able to identify a coupling parameter where the Markovian semigroup limit was reached. One can reason that the Surrogate Hamiltonian bath should behave similarly in this range of coupling parameters.

The system-bath construction in both cases is not Markovian and differs from the Redfield or semigroup treatments. The Surrogate Hamiltonian approach is close in spirit to real path integral techniques [7, 58, 121], where a large many-body propagator is constructed and approximated. Generally, the path integral methods, are applicable to harmonic baths and a linear system-bath coupling, and lead to a non-Markovian description.

3.1 Dissipative dynamics of anharmonic oscillator

3.1.1 Model

The system under study describes a primary system immersed in a bath. The state of the combined system-bath is described by the wave function $\Psi(\hat{\mathbf{R}}, \hat{\boldsymbol{\beta}}_1, \ldots, \hat{\boldsymbol{\beta}}_{2^N})$ where $\hat{\mathbf{R}}$ represents the nuclear configuration of the dynamical system, and $\{\hat{\boldsymbol{\beta}}_j\}$ are the bath degrees of freedom. The Hamiltonian of such a combined system is:

$$\hat{\mathbf{H}} = \hat{\mathbf{H}}_S \otimes \mathbb{1}_B + \mathbb{1}_S \otimes \hat{\mathbf{H}}_B + \hat{\mathbf{H}}_{SB} \quad . \tag{3.1}$$

The primary system is constructed from an anharmonic (Morse) oscillator of mass M:

$$\hat{\mathbf{H}}_S = \frac{\hat{\mathbf{P}}^2}{2M} + D\left(e^{-2\alpha\hat{\mathbf{R}}} - 2e^{-\alpha\hat{\mathbf{R}}}\right) \ . \tag{3.2}$$

The coupling term is non-linear in the Morse oscillator coordinate R, but reduces to a linear one for a small R:

$$f(\hat{\mathbf{R}}) = \frac{1 - e^{-\alpha\hat{\mathbf{R}}}}{\alpha} \ . \tag{3.3}$$

$\hat{\mathbf{H}}_B$ denotes the bath Hamiltonian consisting of an infinite sum of single mode Hamiltonians $\hat{\mathbf{h}}_j$:

$$\hat{\mathbf{H}}_B = \sum_j \hat{\mathbf{h}}_j, \ . \tag{3.4}$$

For the harmonic bath the single mode Hamiltonians take the form:

$$\hat{\mathbf{h}}_j \quad = \quad \frac{\hat{\mathbf{p}}_j^2}{2m_j} + \frac{m_j\omega_j^2}{2}\hat{\mathbf{q}}_j^2 \quad = \quad \omega_j \hat{\mathbf{a}}_j^+ \hat{\mathbf{a}}_j \ , \tag{3.5}$$

where $\hat{\mathbf{p}}_j, \hat{\mathbf{q}}_j$ are the normal mode momentum and coordinate respectively, and $\hat{\mathbf{a}}_j = \sqrt{\frac{m_j\omega_j}{2}}\hat{\mathbf{q}}_j + \frac{i}{\sqrt{2m_j\omega_j}}\hat{\mathbf{p}}_j$ is the corresponding annihilation operator. For the spin bath:

$$\hat{\mathbf{h}}_j \quad = \quad \omega_j \hat{\boldsymbol{\sigma}}_j^+ \hat{\boldsymbol{\sigma}}_j \ , \tag{3.6}$$

where $\hat{\boldsymbol{\sigma}}_j^+$, $\hat{\boldsymbol{\sigma}}_j$ are the standard spin creation and annihilation operators of mode j.

The system-bath interaction $\hat{\mathbf{H}}_{SB}$ can be decomposed into a sum of products of system and bath operators without loss of generality. Specifically a system-bath coupling inducing vibrational relaxation is considered:

$$\hat{\mathbf{H}}_{SB} = -f(\hat{\mathbf{R}}) \otimes \sum_j \hat{\mathbf{V}}_j \ , \tag{3.7}$$

where $\hat{\mathbf{V}}_j = \lambda_j \hat{\mathbf{q}}_j = \lambda_j(\hat{\mathbf{a}}_j^+ + \hat{\mathbf{a}}_j)$ for the harmonic bath and $\hat{\mathbf{V}}_j = \lambda_j(\hat{\boldsymbol{\sigma}}_j^+ + \hat{\boldsymbol{\sigma}}_j)$ for the spin bath. $f(\hat{\mathbf{R}})$ is a function of the system coordinate operator. The influence of the bath on the primary system is characterized by the spectral density function $J(\omega)$.

The spectral density function was chosen to be the same for the harmonic bath case as well as for the Surrogate Hamiltonian method. For an Ohmic bath the damping rate γ is frequency-independent and the spectral density in the continuum limit is given by

$$J(\omega) = M\gamma\omega \tag{3.8}$$

for all frequencies ω up to the cutoff frequency ω_c. A finite bath with equally spaced sampling of the energy range was used.

The parameters used are the same as in Ref. [119]: a well depth D of 0.018 a.u., $\alpha = 2$ a.u., and a mass of $M = 10^5$ a.u. The initial state was chosen to be a Gaussian displaced by $R_0 = 2\tilde{R}$ from the origin with a width of $\sigma = \tilde{R}$ ($\tilde{R} \approx 0.09129$ a.u. is the characteristic length scale of the Morse oscillator). For such a displacement the coupling term (3.3) is almost linear. The initial system-bath state has a direct product form where the bath is at zero temperature. Such a state has no initial correlations between the system and the bath.

There are a few characteristic time scales of the system. The period of the Morse oscillator is $\tau_{osc} = 2\pi/\Omega \approx 127$ fs, where $\Omega = \alpha\sqrt{2D/M}$ refers to the harmonic frequency of the potential. The bath has two time scales. τ_{bath} is associated with the highest frequency $\omega_c = 2.5\Omega$ and corresponds to a time scale of 52 fs. The time

scale corresponding to the frequency spacing $\Delta\omega$ defines the Poincaré period (τ_{rec}). It should be larger than any other time scale of interest. With ω_c fixed this time becomes:

$$\tau_{rec} = \frac{2\pi}{\Delta\omega} = \frac{2\pi N}{\omega_c} \ . \tag{3.9}$$

Thus, with an increasing number of bath modes, the convergence progresses in time. In our simulations the number of TLS is chosen to be $N = 20 \ldots 60$ (for different coupling strengths), which ensures that τ_{rec} is greater than the overall simulation time.

The calculations were performed in three different interaction regimes identified by considering the involved time scales: (i) weak coupling referring to $\gamma^{-1} = 1630$ fs $\gg \tau_{osc}, \tau_{bath}$; (ii) the intermediate situation characterized by $\gamma^{-1} = 163$ fs $\approx \tau_{osc} > \tau_{bath}$; (iii) the strong coupling regime defined by $\gamma^{-1} = 54$ fs $\approx \tau_{bath} < \tau_{osc}$.

In the simulations discussed below, the average position of the oscillator and the energy relaxation were calculated for all three coupling strengths. For comparison, the effective subsystem energy was defined as in [119]:

$$E_S = \langle \hat{\mathbf{H}}_S^{'} \rangle = \langle \hat{\mathbf{H}}_S \rangle \ + 0.5 \langle \hat{\mathbf{H}}_{SB} \rangle \ . \tag{3.10}$$

It includes half of the system-bath interaction term.

The dynamics of the system combined with the bath is generated by solving the time-dependent Schrödinger equation:

$$\Psi(\hat{\mathbf{R}}, \{\hat{\boldsymbol{\beta}}_\mathbf{j}\}, t) = e^{-i\hat{\mathbf{H}}t} \Psi(\hat{\mathbf{R}}, \{\hat{\boldsymbol{\beta}}_\mathbf{j}\}, 0) \ . \tag{3.11}$$

Each spinor component $\psi_j(\hat{\mathbf{R}})$ is represented on a spatial grid. The kinetic energy operator is applied in Fourier space employing FFT [4], and the Chebychev method [114] is used to compute the evolution operator. Numerical details of applying the bath operators have already been given in Ref. [88, 95].

In the MCTDH method [122, 123] the wavefunction Ψ, which describes the dynamics of a system with M degrees of freedom, is expanded as a linear combination of time-dependent Hartree products:

$$|\Psi(Q_1, \ldots, Q_M, t)\rangle = \sum_{j_1=1}^{n_1} \cdots \sum_{j_M=1}^{n_M} A_{j_1,\ldots,j_M}(t) \prod_{\kappa=1}^{M} |\varphi_{j_\kappa}^{(\kappa)}(Q_\kappa, t)\rangle \ ,$$

where $|\varphi_{j_\kappa}^{(\kappa)}\rangle$ is the single-particle function (spf) for the κ degree of freedom and the $A_{j_1,\ldots,j_M}$ denote the MCTDH expansion coefficients. The total number of coefficients

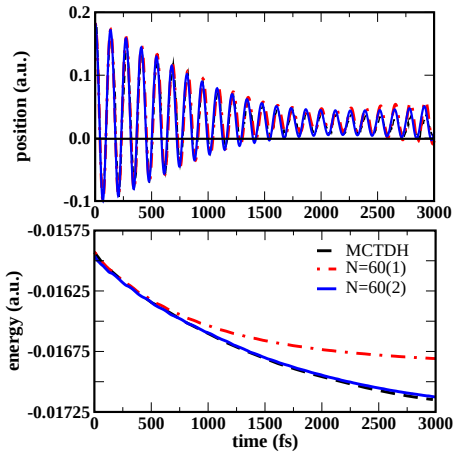

Figure 3.1: The energy relaxation (lower panel) and damped oscillations of the average position (upper panel) of the Morse oscillator in the weak coupling limit ($\gamma^{-1} = 1630$ fs). The bath is assumed to be Ohmic with cutoff frequency $\omega_c = 2.9 \cdot 10^{-3}$ a.u. and consists of $N = 60$ TLS. The initial state was chosen to be a Gaussian displaced by $R_0 = 2\tilde{R}$ with a width of $\sigma = \tilde{R}$, where $\tilde{R} \approx 0.09129$. Dashed lines refer to the MCTDH calculations with a bath of harmonic oscillators (adopted from Ref. [119]). Dashed-dotted lines refer to the Surrogate Hamiltonian calculations with only single excitations. Solid lines refer to calculations with two simultaneous excitations allowed.

$A_{j_1,\ldots,j_M}$ and basis function combinations scales exponentially with the number of degrees of freedom M. Considering a system coupled to a multi-mode bath, the use of the *multiconfigurational* wave function ensures the correct treatment of the system-bath correlations [92, 124]. The method also enables grouping of several modes together, which reduces both the number of single-particle degrees of freedom and the correlation effects between different modes. Although the exact treatment is contained in the limit of an infinite number of configurations, in the weak coupling limit, the time-dependent basis employed in the MCTDH method should be relatively small. Worth et al. [124] have pointed out that even for weak coupling, one spf per bath mode (the Hartree limit) is not sufficient to fully describe the system-bath interaction. However, the number of spf's for the bath degrees of freedom can be increased until convergence is achieved, which makes this approximation controllable.

3.1.2 Energy relaxation and small amplitude motion

First a restricted Surrogate Hamiltonian is applied, which limits the possible system-bath correlations. The most extreme restriction includes only single excitations. The

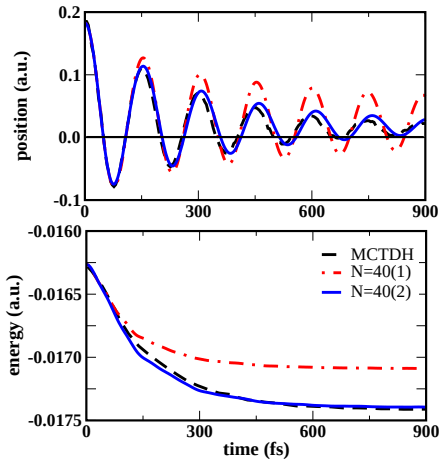

Figure 3.2: The energy relaxation (lower panel) and damped oscillations of the average position (upper panel) of the Morse oscillator in the intermediate coupling regime ($\gamma^{-1} = 163$ fs). The bath parameters and the initial state are the same as in the weak coupling calculations. The number of bath modes is $N = 40$. Dashed lines refer to the MCTDH calculations with a bath of harmonic oscillators (adopted from Ref. [119]). Dashed-dotted lines refer to the Surrogate Hamiltonian calculations with single excitations only. Solid lines refer to the calculations with two allowed simultaneous excitations.

results for the weak coupling case ($\gamma^{-1} = 1630$ fs) are shown in Fig. 3.1. For a short period of time the energy relaxes with the same rate in the two types of bath. However, after $t_s \approx 500$ fs the rate decreases and eventually the system energy becomes constant. It should be pointed out, that the saturation time is not the recurrence (Poincaré) time ($t_s < \tau_{rec}$). This is confirmed by the fact that for time $t > t_s$ the overall energy transfer from the bath back to the system is not complete. Calculating the population of the bath modes shows that at $t > t_s$ most of the system energy is transferred to very few (or even one) bath modes, which are in resonance with the system's frequency. Modes which are near to the resonance mode or modes become saturated and start to transfer the excitation back to the system. A dynamic "steady state" between the system and the bath is formed, where most of the modes transfer energy back, while one (or very few) continue to absorb energy from the system.

When the number of simultaneous excitations is increased to two, the effect of saturation appears at a later stage ($t_s > 2000$ fs). The results become similar to those of Ref. [119] and the values of the average position (see Fig. 3.1 (upper panel)) are nearly indistinguishable. We conclude that for the weak coupling case,

the bath that has two simultaneous excitations is completely sufficient to reproduce the dynamics generated by *all* simultaneous excitations for times up to 2 ps.

The relaxation dynamics for medium coupling are shown in Fig. 3.2. A saturation effect was obtained for the bath restricted to single excitations. However, two simultaneous excitations were sufficient to overcome this saturation and converge the whole dynamics of the problem. A slight difference in the energy relaxation rate of the two baths is identified. The TLS bath causes stronger relaxation, but the results are still in good agreement with those of Ref. [119]. Since the initial state is a function of $\hat{\mathbf{R}}$ and the system-bath coupling depends on $\hat{\mathbf{R}}$ as well, the initial excitation influences the effective strength of the coupling. If the initial displacement, i.e. the initial excitation of the primary system, is decreased, the saturation is postponed. We can then deduce that the relaxation rate converges to the value of Ref. [119]. Combining the results of Figs. 3.1 and 3.2 leads to the conclusion that the differences between the two types of bath in the weak and intermediate coupling regimes are caused by the saturation of a few "central" modes in the spin bath. This saturation is postponed if the bath includes more correlations. For very weak coupling, these higher order system-bath correlations become insignificant.

The problem of including all system-bath correlations is therefore crucial in the medium and strong coupling regime. Fig. 3.3 shows the difference in the system energy ($\langle\hat{\mathbf{H}}_S\rangle + 0.5\langle\hat{\mathbf{H}}_{SB}\rangle$) for two cases: a bath with only single excitations and a bath in which two simultaneous excitations are allowed. The calculations were made for different coupling strengths. As the coupling strength is reduced, the difference decreases. Thus in a very weak coupling limit, the TLS bath with only single excitations (no system-bath correlations) becomes sufficient to describe the dynamics for relatively long times. In this limit the TLS bath coincides completely with the harmonic bath.

The issue of including system-bath correlations has also been addressed in the MCTDH calculations. In Ref. [120] the same system has been studied with the G-MCTDH method (the MCTDH with Gaussian expansion functions). Differences between the single-configurational (the Hartree limit) and the multi-configurational descriptions (with an increasing number of single particle functions) have been obtained for the energy relaxation process. In these calculations at least four single

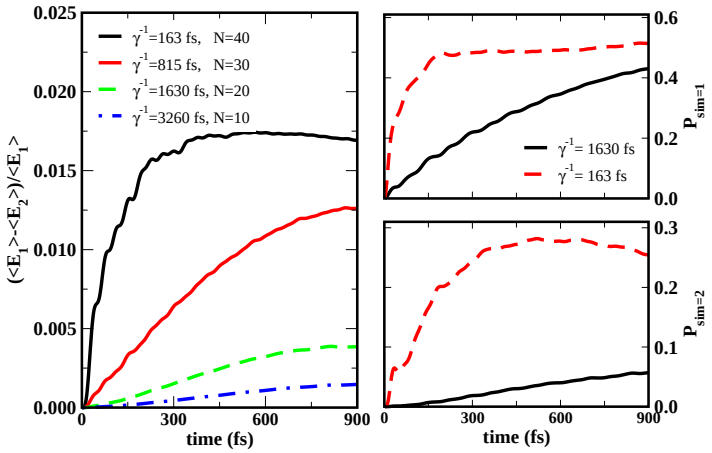

Figure 3.3: (Left panel) The relative difference in the effective subsystem energy ($\langle H_S \rangle + 0.5\langle H_{SB} \rangle$) between the bath with only single excitations allowed $\langle E_1 \rangle$ and the bath with two simultaneous excitations $\langle E_2 \rangle$ as a function of time. The difference is calculated for a few coupling strengths. The simulation time is $t = 900$ fs and the number of bath modes is $N = 10 \ldots 40$. (Right panel) The population P_{sim} of 1 and 2 simultaneous bath excitations is compared to the bath with two simultaneous excitations. The solid lines refer to the weak coupling limit ($\gamma^{-1} = 1630$ fs) and the dashed lines refer to medium coupling ($\gamma^{-1} = 163$ fs).

particle functions per resonant bath modes and two spf for secondary modes were required to achieve convergence in the relatively weak coupling limit ($\gamma^{-1} = 500$ fs).

In the strong coupling regime (Fig. 3.4) there is considerable deviation between the two models. In the Surrogate Hamiltonian model the energy relaxes faster and the oscillator is damped after a single period. As expected, convergence requires many simultaneous excitations. For example, a bath consisting of $N = 20$ modes requires at least four simultaneous excitations for converging the energy relaxation dynamics. Although the spin bath with a few simultaneous excitations is sufficient to overcome the saturation effect, it does not produce the same results as the harmonic bath in the MCTDH method.

3.1.3 The interaction between the bath modes

The saturation of bath modes is expected whenever an anharmonic bath is employed. Nevertheless, to mimic the harmonic bath more closely the saturation of the bath modes should be reduced. This effect is obtained by allowing energy exchange between the bath modes. For the Surrogate Hamiltonian this is done by adding to

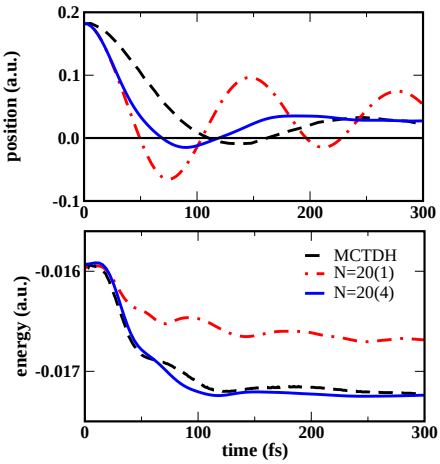

Figure 3.4: The energy relaxation (lower panel) and damped oscillations of the average position (upper panel) of the Morse oscillator in the strong coupling strength ($\gamma^{-1} = 54$ fs). The bath parameters and the initial state are the same as in the weak coupling calculations. The number of bath modes is $N = 20$. Dashed lines refer to Nest and Meyer's MCTDH calculations (adopted from Ref. [119]). Dashed-dotted lines refer to the Surrogate Hamiltonian calculations with single excitations. Solid lines refer to a bath with four excitations allowed simultaneously.

the bath Hamiltonian $\hat{\mathbf{H}}_B$ the following term:

$$\hat{\mathbf{H}}_{int} = \sum_{ij} \kappa_{ij} (\hat{\boldsymbol{\sigma}}_i^+ \hat{\boldsymbol{\sigma}}_j + \hat{\boldsymbol{\sigma}}_j^+ \hat{\boldsymbol{\sigma}}_i) \ , \tag{3.12}$$

where the parameter $\kappa_{ij} (= \kappa_{ji}^*)$ is the interaction strength between two bath modes. The interaction can be restricted to the nearest neighbors in energy by the condition $\kappa_{ij} = 0$ for $|i - j| > 1$. The detailed algorithm of applying Eq.(3.12) in the bit representation has been described in Appendix B in the context of pure dephasing.

The term $\hat{\boldsymbol{\sigma}}_i^+ \hat{\boldsymbol{\sigma}}_j + \hat{\boldsymbol{\sigma}}_j^+ \hat{\boldsymbol{\sigma}}_i$ describes a two quasi-particle interaction within the bath. A qualitative picture is based on an almost elastic exchange of energy between the two nearest neighbor bath modes which are almost degenerate. The process is described by a creation of an excitation in one mode at the expense of another and vice versa.

The new bath Hamiltonian including the interactions can be diagonalized leading to:

$$\hat{\tilde{\mathbf{H}}}_B = \sum_i \tilde{\omega}_i \hat{\tilde{\boldsymbol{\sigma}}}_i^+ \hat{\tilde{\boldsymbol{\sigma}}}_i \ , \tag{3.13}$$

where $\tilde{\omega}_i$ are the eigenvalues of $\hat{\mathbf{D}}^+ (\hat{\mathbf{H}}_B + \hat{\mathbf{H}}_{int}) \hat{\mathbf{D}}$. In the new basis of $\{\hat{\tilde{\boldsymbol{\sigma}}}_i\}$ the system-bath interaction term in Eq. (3.13) is also modified. However for sufficiently

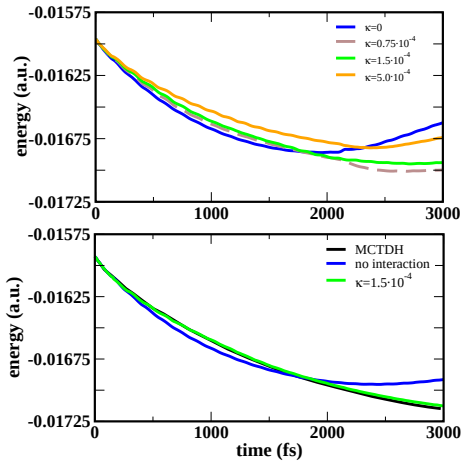

Figure 3.5: The energy relaxation with interaction between the bath modes is shown in the weak coupling limit ($\gamma^{-1} = 1630$ fs). The bath is assumed to be Ohmic with cutoff frequency $\omega_c = 2.9 \cdot 10^{-3}$ a.u. (Upper panel) The influence of the parameter κ is shown for a bath of $N = 40$ modes. (Lower panel) The energy relaxation is shown with the optimal parameter of $\kappa = 1.5 \cdot 10^{-4}$ (thin line). The thick solid line refers to MCTDH calculations with a bath of harmonic oscillators ([119]). The dashed line refers to Surrogate Hamiltonian calculations with two simultaneous excitations allowed without interaction between the bath modes. The bath consists of $N = 60$ modes.

small κ the eigenvalues of the bath change only slightly, but the saturation effect is postponed to a much later time.

Fig. 3.5 shows the influence of the interaction between the bath modes on energy relaxation in the weak coupling limit ($\gamma^{-1} = 1630$ fs). The dynamics are calculated for a relatively long period of 3 ps. For such a long time the saturation effect is observed even for a bath with two simultaneous excitations. Since the saturation time t_s is determined mostly by the saturation of the few modes close to resonance with the subsystem, increasing the number of modes does not prolong t_s.

Adding an interaction between the bath modes leads to slower decay and delayed saturation (Cf Fig. 3.5, upper panel). This can be understood from the following considerations: the interaction term, Eq.(3.12), describes the transport of excitation from one bath mode to its nearest neighbor. Consequently, κ determines how quickly the excitation is transported away from a TLS mode close to resonance with the primary system. On the other hand, the interaction energy, i.e. the expectation value of $\langle \hat{\mathbf{H}}_{SB} \rangle$, depends on the population of the primary system and of the bath modes close to it. If the population is removed from those bath modes and "diffuses"

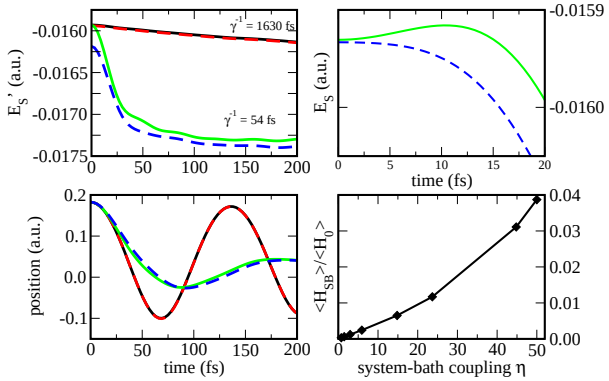

Figure 3.6: Effect of initial correlations. The energy relaxation and damped oscillations of the average position are shown for the initially uncorrelated (solid lines) and correlated (dashed lines) states. The dynamics for weak ($\gamma^{-1} = 1630$ fs) and strong couplings ($\gamma^{-1} = 54$ fs) are compared. A bath consisting of $N = 10$ modes with 2 and 5 simultaneous excitations (for the weak and strong coupling, respectively) is sufficient to obtain the converged results. (Left) The effective subsystem energy (upper panel) ($E_S^{'} = \langle H_S \rangle + 0.5\langle H_{SB} \rangle$) and the expectation value for the Morse coordinate (lower panel) are shown. (Right) The bare subsystem energy (upper panel) $E_S = \langle H_S \rangle$ in the strong coupling regime ($\gamma^{-1} = 54$ fs) is shown for the short time dynamics. The energy stored in the system-bath coupling (lower panel) is calculated as a function of the coupling constant $\eta = M\gamma$.

all over the bath, the interaction energy decreases and the decay becomes slower. This explains the upper panel of Fig. 3.5 which shows the energy relaxation for different values of κ.

An optimal value of the inter-spin coupling parameter κ should minimize saturation without altering the spectral density. As an example, $\kappa = 1.5 \cdot 10^{-4}$ for calculations carried out for $N = 60$ bath modes (Cf. the lower panel of Fig. 3.5). For this value of κ the spectrum of the bath deviated less than 1%. The energy relaxation in this case is almost indistinguishable from the results obtained in Ref. [119] for the harmonic bath.

3.1.4 Correlated versus uncorrelated states

The widely used assumption of an initially uncorrelated system-bath state is not consistent with most experimental situations [26, 41, 125]. The influence of initial correlations has been addressed in the context of the weak coupling approximation, where it appears as an additional inhomogeneous term [26].

A fully correlated initial state is easily obtained in the Surrogate Hamiltonian

method. Once the system-bath Hamiltonian $\hat{\mathbf{H}}$ is set, the correlated ground state can be determined by propagating an initial guess wave function in imaginary time using $\hat{\mathbf{H}}$ [114].

The influence of initial correlations is shown in Fig. 3.6. The uncorrelated state is identical to that of the previous calculations: the primary system is defined as a shifted Gaussian wave packet, while the bath is not excited. For the correlated initial state, the ground state of the total system was calculated first. Then this ground state was displaced by the shift operator in momentum space $\hat{\mathbf{D}} = e^{-iR_0\hat{\mathbf{k}}}$ with $R_0 = 2\tilde{R}$. The dynamics of the correlated state are compared to that of the uncorrelated state for weak and strong couplings ($\gamma^{-1} = 1630$ fs and $\gamma^{-1} = 54$ fs). The dashed and solid lines in Fig. 3.6 correspond to the initial state being correlated and uncorrelated, respectively.

The short-time dynamics differ for the correlated and uncorrelated cases, since the correlations need to be built up in the uncorrelated case [40]. In the latter case an initial slippage in the system energy can be observed before the reduced dynamics appear to be Markovian (right upper panel). This effect is insignificant for weak coupling. Even for strong coupling, the differences between the correlated and uncorrelated cases were found to be very small. Apparently, the displacement is a stronger "perturbation" than that caused by the correlations, i.e. the displacement establishes a new initial state [126].

3.1.5 Decoherence

Decoherence has become a popular term used to describe loss of phase in coherent superpositions of quantum states due to interaction with a bath. It is therefore natural to compare the decoherence properties of the spin bath to those of the harmonic bath. The first difficulty is that there are different approaches to the definition of decoherence. Alicki [9] identifies pure decoherence (dephasing) with the decay of the off-diagonal elements of the density operator, which is not accompanied by dissipation. He then argues that dephasing cannot be caused by a harmonic oscillator bath with a coupling, which is linear in coordinates or momenta.

Energy relaxation is also accompanied by loss of phase. For comparison, we will consider decoherence as a process caused by energy relaxation, which is character-

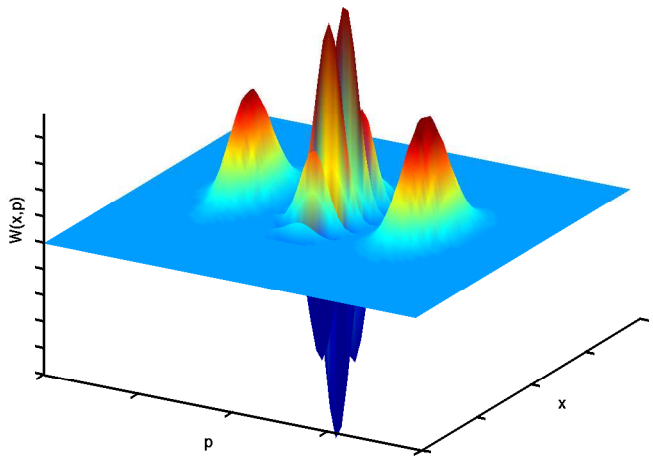

Figure 3.7: Wigner function $W(x,p)$ of a superposition of two spatially displaced Gaussian wave packets at $R_0 = \pm 0.25$ a.u. with a coherent-state width of $\sigma = (2M\omega_0)^{-1}$ (Cat state). The figure shows $W(R,P)$ at the initial time $t = 0$. The interference term, which appears between the Gaussian packets, indicates their coherence and decays with time.

ized by a time $T_1 = \gamma^{-1}$. The decoherence effect will be illustrated in terms of the dissipative dynamics of cat states, defined as a superposition of two coherent states. The interaction with the environment leads to decay of the coherences of such a superposition on an extremely short time scale, usually much shorter than the corresponding relaxation time scale [127]. This process has been modeled using G-MCTDH by [120], and as a result can be used for a comparative study.

The Wigner function of the cat state (Fig. 3.7) consists of two Gaussians centered at $(\pm R_0, p_0)$ and an interference term, which is centered at the origin. The off-diagonal part of the density matrix in the coherent-state basis, which contains information about quantum interferences between the two components of the cat state, decays with the rate γ_{coh}. In the Markovian limit the decay rate is proportional to the square of the distance between the coherent states. For zero temperature it is given by [128, 129]:

$$\gamma_{coh} = \frac{\gamma M \omega_0 \delta^2}{2\hbar} \,. \tag{3.14}$$

ω_0 and δ are parameters of the primary system (ω_0 represents the frequency of the harmonic oscillator, and δ is the separation distance between the coherent states).

The decoherence rate for a primary system coupled to a TLS bath is calculated and compared to the calculations for a bath of harmonic oscillators with the G-MCTDH method [120]. The calculations are performed for a cat state in a harmonic

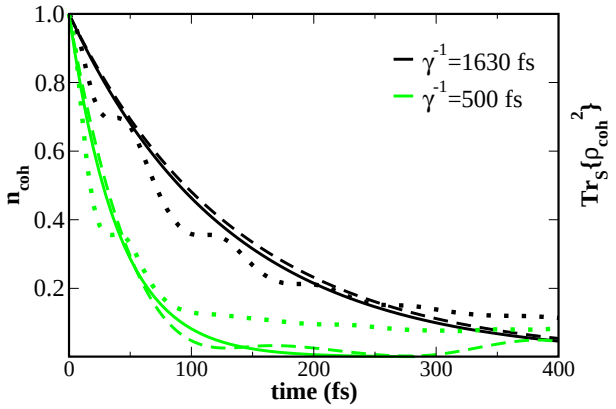

Figure 3.8: The decoherence effect in terms of decay of the coherence norm and off-diagonal elements in the energy representation. The coherence norm n_{coh} is shown as a function of time for two different couplings, $\gamma^{-1} = 1630$ fs and $\gamma^{-1} = 500$ fs. In the golden rule limit, off-diagonal elements of the reduced system density matrix $\rho(R, R')$ decay exponentially with the decoherence rates $\gamma_{coh}^{-1} = 130$ fs and $\gamma_{coh}^{-1} = 40$ fs (for the two given couplings, respectively). This decay is shown by the full lines. The dashed lines refer to the calculated decay of the decoherence norm. The dotted lines show the decay of $\mathsf{tr}_S\{\hat{\boldsymbol{\rho}}_{coh}^2\}$ in the energy representation.

oscillator potential with $\omega_0 = 10^{-3}$ a.u. and $M = 10^5$ a.u. The bath has the same parameters as for the previous calculations with damping rates of $\gamma^{-1} = 1630$ fs and $\gamma^{-1} = 500$ fs.

A quantitative measure of decoherence of the primary system is the coherence norm used by Strunz et al. [130]:

$$n_{coh}(t) = \mathsf{tr}_S \left\{ \hat{\boldsymbol{\rho}}_S^{\mathsf{coh}}(t) \hat{\boldsymbol{\rho}}_S^{\mathsf{coh}+}(t) \right\} \ , \tag{3.15}$$

where $\hat{\boldsymbol{\rho}}_S^{\mathsf{coh}}$ refers to off-diagonal elements of the subsystem reduced density matrix in the basis of coherent states.

Since decoherence is a basis-dependent phenomenon, one can ask if it can also be measured in the basis of the eigenstates of the system Hamiltonian $\hat{\mathbf{H}}_S$. The question arises, whether these eigenstates form a pointer basis [131] - the basis with respect to which off-diagonal elements in the reduced density operator disappear due to decoherence. To perform this test the system density operator $\hat{\boldsymbol{\rho}}_S(t) = \mathsf{tr}_B\{\hat{\boldsymbol{\rho}}\}$, which has been calculated in the coordinate basis is transformed to the basis of the $\hat{\mathbf{H}}_S$ eigenstates. Decomposing such a state to a dynamical and a static part leads to [132]:

$$\hat{\boldsymbol{\rho}}_S(t) = \hat{\boldsymbol{\rho}}_{coh}(t) + C^2 \hat{\boldsymbol{\rho}}_S^{\mathsf{eq}} \tag{3.16}$$

where $\hat{\boldsymbol{\rho}}_S^{\mathsf{eq}}$ is the equilibrium stationary system density operator and C^2 is an overlap functional given by

$$C^2 = \mathsf{tr}_S\{\hat{\boldsymbol{\rho}}_S(t) \cdot \hat{\boldsymbol{\rho}}_S^{\mathsf{eq}}\} / \mathsf{tr}_S\{\hat{\boldsymbol{\rho}}_S^{\mathsf{eq}\,2}\} \quad . \tag{3.17}$$

$\hat{\boldsymbol{\rho}}_{coh}(t)$ in Eq.(3.16), has no diagonal elements in the energy representation and is therefore traceless. Thus the decoherence effect is measured by the decay of $\mathsf{tr}_S\{\hat{\boldsymbol{\rho}}_{coh}^2\}$.

Fig. 3.8 shows the decay of the coherence norm n_{coh} and $\mathsf{tr}_S\{\hat{\boldsymbol{\rho}}_{coh}^2\}$ for two different coupling strengths (both are weak). The thick lines refer to a simple exponential decay predicted by Eq.(3.14) for a harmonic bath and confirmed by Ref. [120]. The dashed lines refer to the calculated decay of n_{coh}, which is in good agreement with the prediction. The decay of $\mathsf{tr}_S\{\hat{\boldsymbol{\rho}}_{coh}^2\}$ (the dotted lines) has almost the same rate at a relatively short time. However, the off-diagonal elements of $\hat{\boldsymbol{\rho}}_S$ in the energy representation do not decay strictly to zero. Therefore, in this case, the system energy eigenstates cannot be considered as a pointer basis [131].

3.2 Entanglement

Entanglement between two quantum states is a manifestation of additional quantum correlation. For example entanglement between the system and the bath means $\hat{\boldsymbol{\rho}} \neq \hat{\boldsymbol{\rho}}_S \otimes \hat{\boldsymbol{\rho}}_B$. In a dissipative environment it is expected that initial entanglement between parts of the system are lost leading to decoherence [133, 134]. In addition a bath can also provide an indirect interaction between totally decoupled parts of the primary system and entangle them [135, 136].

The difference between the harmonic and the spin baths should be manifested in another type of entanglement - quantum correlations between different bath modes. A system interacting with the spin bath, can induce entanglement between two spin modes, which are not directly interacting with each other. In the harmonic bath on the other hand, a system linearly coupled to different modes is not able to entangle those modes (see Appendix C).

Peres [137] and Horodecki et al. [138] have provided a criterion, based on partial transposition, to determine whether a given mixed state of two subsystems is entangled (cf Appendix D). Since the criterion is defined only for two coupled TLS, the

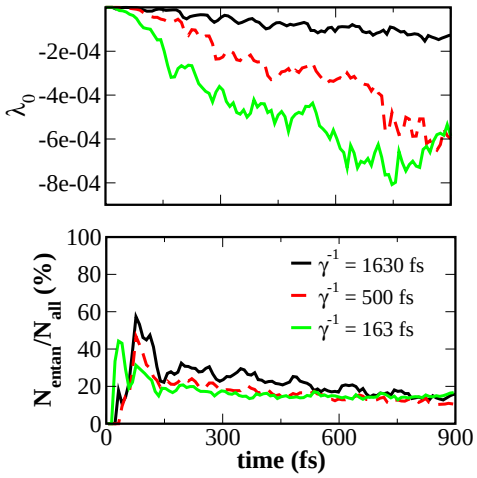

Figure 3.9: Measurement of entanglement between the bath modes as a function of time. (Upper panel) The smallest eigenvalue of the partial transposition ρ^{T_j} of the reduced density matrix for pair of the bath modes (i, j) is calculated according to Appendix D. The negative eigenvalues are averaged over all possible combinations of the bath modes. (Lower panel) The relative number of entangled pairs of the bath modes as a function of time. The calculations are performed for three different system-bath coupling strengths ($\gamma^{-1} = 1630, 500, 163$ fs). The bath consisting of $N = 40$ modes with two simultaneous excitations allowed is used in all calculations.

study of entanglement is limited to *two* bath modes (i) and (j). The density operator of any two bath modes $\hat{\boldsymbol{\rho}}_{ij}$ is obtained as a partial trace of $\mathsf{tr}_{k\neq i,j}\{\hat{\boldsymbol{\rho}}_B\}$ over the rest of the bath modes, where the density operator of the bath is $\hat{\boldsymbol{\rho}}_B = \mathsf{tr}_S\{\hat{\boldsymbol{\rho}}\}$. The procedure checks whether the partial transposition of $\hat{\boldsymbol{\rho}}_{ij}$ with respect to one of the modes has negative eigenvalues. The smallest eigenvalue λ_0 of the partial transpose matrix ρ^{T_j} constitutes the criteria. Then the eigenvalues with $\lambda_0 < 0$ are averaged over all *entangled* pairs of bath modes.

In Fig. 3.9 the averaged parameter λ_0 is shown as a function of time for three different coupling strengths. The entanglement calculations were based on converged results obtained for a bath of $N = 40$ modes. This was sufficient to a time scale of 900 fs, for all three system bath coupling strength considered. Since at $t = 0$ the bath is not excited, there are no entangled bath modes, therefore $\lambda_0 = 0$ for all pairs. As t increases λ_0 becomes negative for some of the pairs of the bath modes, meaning that these modes become entangled. As time progresses, the number of entangled pairs saturates for all three couplings (Cf Fig. 3.9, lower panel). Therefore, the increase in the absolute value of λ_0 is related primarily to the growth in population of the entangled modes. The maximum in the number of entangled modes for an

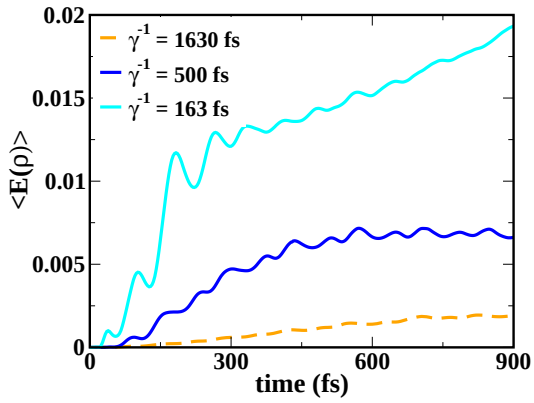

Figure 3.10: The entanglement of formation $E(\rho)$ is calculated for a couple of the bath modes (i, j). The average over all possible pairs is shown as a function of time. The calculations are performed for three different system-bath coupling strengths ($\gamma^{-1} = 1630, 500, 163$ fs). The bath consisting of $N = 40$ modes with two simultaneous excitations allowed is used in all calculations.

early time may be associated with the creation of higher-order entanglement terms where three or more simultaneous excitations become important. Such higher-order entanglement is not captured by the Peres-Horodecki parameter.

To characterize the degree of entanglement we use an additional measure, the entanglement of formation introduced by Wootters et al. [139–141] (Cf. Appendix D). For any $2 \otimes 2$ mixed state this quantity varies from zero (separable states) to one (maximally entangled states). Our results (Cf. Fig. 3.10) are obtained by averaging the entanglement of formation $E(\rho_{ij})$ (for two bath modes i and j) over all possible pairs of modes. The dynamics of $\langle E(\rho) \rangle$ is similar to those of the partial transpose parameter. It should be noted that the growth of entanglement shown in Figs. 3.9-3.10 is exclusive to the spin bath.

3.3 Discussion

The similarities and differences of the relaxation dynamics of a primary system coupled to a spin or to a harmonic bath have been analyzed. The study was facilitated by the ability to obtain converged numerical results for finite period in time. In both cases this task becomes possible by employing a large but finite number of bath modes and controlling the degree of correlation.

For all cases studied the extremely short time dynamics was identical. This

period represents the inertial response of the bath and is characterized by a zero derivative of the energy at the initial time $t = 0$. This non-Markovian dynamical evolution, "the slippage", is quite short and in many cases it can be ignored. The initial dynamics is closely related to the issue of the choice of the initial state. Preferably it should represent equilibrium system bath correlation and not be a product state. The Surrogate Hamiltonian method allows to create such a fully correlated initial state of the system-bath entity. However, in the present model differences in the dynamics between correlated and uncorrelated states seem to be insignificant, even in the strong coupling case. It is expected that the same phenomena would be observed in the harmonic bath.

For weak system-bath coupling the dynamics induced by both baths are also similar. This is a numerical confirmation that in the weak coupling limit the harmonic bath can be mapped to the spin bath [97–99]. In addition in this limit the spin bath converges with only single excitations of the bath modes meaning that the system and bath are almost disentangled. This fact is consistent with the convergence to the Markovian limit [142].

The decoherence properties of the harmonic and spin baths as determined by the loss of phase of cat states are found to be quite similar. This result is somewhat surprising since the ergodic properties of the two baths are different. To rationalize, one should notice that the coherence in cat states composed of a superposition of two coherent states in a single mode does not represent entanglement. Therefore, this phase loss does not characterize decoherence in accordance with Alicki's notion [9]. Moreover when a pure dephasing term was added it was found that it did not erode the phase coherence between cat states [143]. We conclude that the decoherence properties of the two baths still require a further study.

The spin and harmonic baths begin to deviate when the initial excitation of the primary system is increased. This difference is observed for excitations where the dynamics generated by the harmonic bath is still Markovian. The first indication of differences is the requirement for two simultaneous bath excitations in order to converge the spin bath. For longer time periods, the spin bath saturates, limiting the ability to assimilate the system's energy. The conclusion is that the limit of weak coupling is more restrictive in the spin bath case. The effect of the saturation

can be reduced if the bath Hamiltonian includes a mode-mode coupling term. This term causes diffusion of excitation between the modes, spreading the excitation over a greater number of bath modes. Thus bath modes, which are relatively far from resonance with the primary system become populated and the saturation is suppressed. Practically, this allows to increase the convergence timescale of the spin bath.

In the medium coupling regime there is an overall good agreement between the two models. The spin bath, however, causes stronger relaxation, a fact, which becomes even more visible in the case of strong coupling. In this regime the deviations between the two baths become significant.

The possibility of entanglement of bath modes mediated by the primary system is a major conceptual difference between the spin and harmonic baths. In the spin bath after a short initial period where only single excitations are excited, entanglement between pairs of spins sets-in with what seems as an exponential growth. Later on the pair entanglement is replaced by higher order terms and the pair-entanglement saturates. All these correlations are absent from the harmonic bath. Nevertheless the dynamics of the the primary systems are not very different, except for systems that have extremely strong coupling. The present simulations should be extended to finite temperatures, where different dynamics of harmonic and spin baths is expected when the coupling is larger than the weak coupling regime [70, 97, 99]. The random phase method [144], introduced in the following section, allows to extend the above models to finite temperature applications.

While the Surrogate Hamiltonian method employs a spin bath, the construction of the bath used in our work is still based on the idea of spectral density. The concept of spectral density is derived from a normal mode analysis and therefore intrinsically suffers from the assumption of a weak system-bath coupling. As a result, using the Surrogate Hamiltonian for systems with strong system-bath coupling is questionable, even if there is no formal restriction in the model. Future development of the Surrogate Hamiltonian should focus on a different construction of the spin bath. One of the possibilities is to build the bath from first principles - a strategy, that has already been employed for modeling dissipative dynamics on solid surfaces [94]. Alternative directions may use a random matrix modeling of the environment

[145–150].

The present study has been an important step in establishing the Surrogate Hamiltonian method as a practical simulation tool. The elucidation of the system-bath dynamics allows to tailor a simulation package in particular for ultrafast dynamical processes. The two bath models represent different physics. The Surrogate Hamiltonian is more suited to a local mode bath description, while the harmonic bath finds its origin in a global normal mode description. The very similar dynamics observed in the weak and medium coupling cases indicates that from the viewpoint of the reduced dynamics it is hard to identify a distinction between the two baths.

Chapter 4

Random phase thermal wavefunctions

The aim of theoretical simulations based on the Surrogate Hamiltonian approach is to achieve a comprehensive description of realistic experimental systems. For that purpose the extension of the method to finite-temperature situation is required. The early applications of the Surrogate Hamiltonian have been practically restricted to low temperatures due to unfavorable computational scaling. In following Chapter we present a new scheme, which employs a concept of random phase thermal wavefunction and enables the application of the Surrogate Hamiltonian method to systems at finite temperatures.

At zero temperature the combined system-bath is in a pure quantum state and therefore can be described by a single wave function. However, if the temperature T is finite the state of the system in thermal equilibrium with the bath is a quantum mixture, represented by the density operator [20]:

$$\hat{\boldsymbol{\rho}}_\beta = \frac{e^{-\beta\hat{\mathbf{H}}}}{\mathsf{Tr}\left\{e^{-\beta\hat{\mathbf{H}}}\right\}} \tag{4.1}$$

where $\beta = 1/k_bT$, k_b is Boltzmann's constant and $\hat{\mathbf{H}}$ is the Hamiltonian of the combined system. The density operator describing a thermal mixture can be represented in any complete basis of states (for example, the energy eigenstates of the combined Hamiltonian $\hat{\mathbf{H}}$):

$$\hat{\boldsymbol{\rho}}_\beta = \sum_j \frac{e^{-\beta E_j}}{Z} |\Psi_j\rangle\langle\Psi_j| \tag{4.2}$$

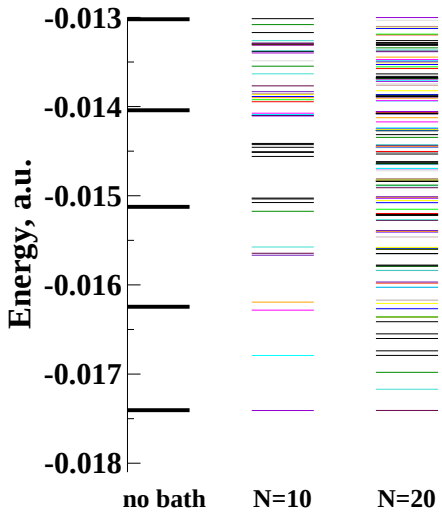

Figure 4.1: Energy levels of the combined system-bath. Calculations are performed for the model of a Morse oscillator linearly coupled to an Ohmic bath of two-level systems. Numerical parameters are given in Sec. 4.2. The energy eigenstates are calculated for the primary system only (left), for the total system with $N = 10$ bath modes (middle) and with $N = 20$ bath modes (right). All calculations are performed for a medium temperature $k_b T = 0.5\omega_0$ and only J eigenstates with Boltzmann weights $e^{-\beta E_J} \ll \epsilon$ are calculated.

where $Z = \sum_j e^{-\beta E_j}$ is the partition function and E_j is the energy of the jth eigenfunction $|\Psi_j\rangle$ of the total Hamiltonian $\hat{\mathbf{H}}$. In order to obtain the expectation value $\langle\hat{\mathbf{A}}\rangle_\beta$ of an observable $\hat{\mathbf{A}}$ for a thermal mixture of states, the expectation values $\langle\hat{\mathbf{A}}_j\rangle$ of each of the pure state components have to be calculated and then averaged by summing over all pure states multiplied by their Boltzmann thermal weights $e^{-\beta E_j}$. Within the Surrogate Hamiltonian method a thermal averaging will require repeating the calculation for each energy eigenstate of the combined system and bath.

This procedure, however, becomes extremely intractable for medium or high temperatures. The reason lies in the fact that the Hilbert space of the total system $\mathcal{H}_S \otimes \mathcal{H}_B$ contains considerably more states than the Hilbert space of the primary system alone $\mathcal{H}_S$. The number of states required for finite-temperature simulations grows with temperature, and what is more important, it grows exponentially as the number of bath modes increases (Cf. Fig. 4.1). Therefore, calculating a large number of the energy eigenstates explicitly and then repeating the propagation step for each initial state restricts the application of the Surrogate Hamiltonian method

to low temperatures. The unfavorable scaling relations of the Surrogate Hamiltonian are behind the motivation for developing an alternative method for the problem of thermal averaging.

4.1 Methodology

4.1.1 The thermal wavefunction

The initial state of a quantum encounter at finite temperature is described by the mixed state density operator Eq.(4.1). The density operator is diagonal in the energy representation therefore:

$$\hat{\boldsymbol{\rho}}_\beta \quad = \quad Z^{-1} \sum_{j=1}^{L} e^{-\beta E_j} |\psi_j\rangle\langle\psi_j| \; , \tag{4.3}$$

with $Z = \sum_j^L e^{-\beta E_j}$, L is the dimension of the Hilbert space $\mathcal{H}$. E_j is the energy of the the jth eigenfunction $|\psi_j\rangle$ of the stationary Hamiltonian $\hat{\mathbf{H}}_0$. An evaluation of Eq. (4.3) by direct diagonalization of $\hat{\mathbf{H}}_0$ would scale as $O(L^3)$. For a finite temperature, employing propagation techniques [114] Eq. (4.3) can be approximated using only J energy eigenfunctions $|\psi_j\rangle$ with Boltzmann weights where J is chosen such that $e^{-\beta E_J} \ll \epsilon$, where ϵ is the error. In this case the numerical effort is close to $O(J^3)$. In the application of interest, the Surrogate Hamiltonian method, both L and J scale exponentially with the simulation time. These scaling relations are the motivation for seeking an alternative method for thermal averaging.

The starting point is a wavefunction composed of a complete set of eigenfunctions $\{|\phi\rangle\}$ with equal amplitude and a random set of phases $\vec{\theta}$:

$$|\Phi(\vec{\theta})\rangle \quad = \quad \sqrt{Q} \sum_{k=1}^{L} \; e^{i\theta_k} |\phi_k\rangle \quad , \tag{4.4}$$

where $\sqrt{Q}$ is a normalization constant. The projection constructed from this wavefunction:

$$|\Phi(\vec{\theta})\rangle\langle\Phi(\vec{\theta})| \quad = \quad Q \sum_{n,m} \; e^{i(\theta_n - \theta_m)} |\phi_n\rangle\langle\phi_m| \; , \tag{4.5}$$

connects all states in the Hilbert space. Using the property of the average of random phases:

$$\left\langle e^{i(\theta_n - \theta_m)} \right\rangle = \frac{1}{2\pi} \int_0^{2\pi} e^{i(n-m)\theta} d\theta = \delta_{nm} \quad , \tag{4.6}$$

the off-diagonal elements of the projection Eq. (4.5) can be eliminated. This property is used to obtain the identity operator $\hat{\mathbf{I}}$ by averaging many realizations of the projection with different phase sets $\vec{\theta}$:

$$\hat{\mathbf{I}} \;=\; \lim_{K\to\infty}\left(\;\frac{1}{K}\sum_{k=1}^{K}|\Phi(\vec{\theta}_k)\rangle\langle\Phi(\vec{\theta}_k)|\;\right) \tag{4.7}$$

where $\vec{\theta}_k$ is the kth realization of the random phase set $\vec{\theta}$. This identity can be employed to construct the thermal state by averaging an ensemble of random thermal wavefunctions:

$$\hat{\boldsymbol{\rho}}_\beta = \frac{1}{Z}e^{-\frac{\beta}{2}\hat{\mathbf{H}}_0}\;\hat{\mathbf{I}}\;e^{-\frac{\beta}{2}\hat{\mathbf{H}}_0} \;=\; \lim_{K\to\infty}\;\frac{1}{Z}\left(\;\frac{1}{K}\sum_{k=1}^{K}|\Phi(\frac{\beta}{2},\vec{\theta}_k)\rangle\langle\Phi(\frac{\beta}{2},\vec{\theta}_k)|\;\right)\quad, \tag{4.8}$$

where the random thermal wavefunction becomes:

$$|\Phi(\frac{\beta}{2},\vec{\theta})\rangle \;=\; e^{-\frac{\beta}{2}\hat{\mathbf{H}}_0}|\Phi(\vec{\theta})\rangle\quad. \tag{4.9}$$

The advantage of Eq. (4.9) is that the random thermal wavefunction can be obtained by propagating an initial random phase wavefunction in imaginary time $\beta/2$. Using this construction a thermal average of an observable $\langle\hat{\mathbf{A}}\rangle_\beta$ becomes:

$$\langle\hat{\mathbf{A}}\rangle_\beta \;=\; \mathsf{tr}\{\hat{\boldsymbol{\rho}}_\beta\hat{\mathbf{A}}\} \;=\; \lim_{K\to\infty}\;\frac{1}{Z}\left(\;\frac{1}{K}\sum_{k=1}^{K}\langle\Phi(\frac{\beta}{2},\vec{\theta}_k)|\hat{\mathbf{A}}|\Phi(\frac{\beta}{2},\vec{\theta}_k)\rangle\;\right). \tag{4.10}$$

The random approach to the thermal-averaged observable is subject to statistical errors. If the realizations are statistically independent, the standard error of the mean value decreases with the square root of the number of random phase sets:

$$\sigma^2 = \frac{\lambda(L)}{K}\quad. \tag{4.11}$$

where $\lambda(L)$ takes into account the dependence of the statistical error on the Hilbert space size L and temperature T, but does not depend on the number of random sets K. Using a sufficiently large number of simulations, $\lambda(L)$ can be determined, as well as the number of random phase sets which are necessary to achieve a given accuracy σ. The dependence of $\lambda(L)$ on the system size can be related to the degree of self-averaging of the observable [151]. If $\lambda(L)$ is a non-increasing function of L with an increase in system size, the random method will become more efficient than the direct Boltzmann thermal averaging.

4.1.2 Numerical details

Method **A**: The numerical implementation of the algorithm is as follows:

1. The first step is to build the initial random phase wavefunction $\Psi(\hat{\mathbf{R}}, \vec{\theta})$. On each equally spaced grid point k the wavefunction is assigned a random value $e^{i\theta_k}$, where θ_k is a real number, $0 \leq \theta_k \leq 2\pi$. Each spinor component is also multiplied by $e^{i\theta_m}$.

2. The random wavefunction $\Psi(\hat{\mathbf{R}}, \vec{\theta})$ is propagated for an imaginary time $\beta/2$ by the thermal propagator $e^{-\frac{\beta}{2}\hat{\mathbf{H}}_0}$. The Newton propagation technique is used [152]. This random phase wavepacket is normalized, leading to $\Psi(\frac{\beta}{2}, \hat{\mathbf{R}}, \vec{\theta})$.

3. The thermal random wavefunction is now used as an initial state for a dynamical simulation propagated in real time. This includes an explicit time dependence of the Hamiltonian induced by an external field. The propagation is cut to short time segments and for each segment $e^{-i\hat{\mathbf{H}}\Delta t}$ is applied. The Chebychev method [114] is used to compute the evolution operator. For time-dependent Hamiltonian, the Chebychev propagator remains stable with a slightly different scaling [153].

4. The relevant dynamical observables of the primary system are calculated.

5. The simulation is repeated, many times, with different sets of initial random wavefunctions, (steps 1-4).

6. The final step is to average all the results obtained for different sets of random phases.

Method **B**: An alternative method for obtaining the random phase wavefunction is based on the assumption that the eigenvalues of $\hat{\mathbf{H}}_0$ are quasi-random. A propagation in real time $e^{-i\hat{\mathbf{H}}_0\tau}$ for a random period τ, will multiply to each eigenvalue component by a random phase $e^{-i\theta_k}$, where $\theta_k = E_k\tau$.

1. A wavefunction is constructed with equal amplitude in all components $\psi(\hat{\mathbf{R}})$.

2. The wavepacket is propagated in imaginary time $\beta/2$ by $e^{-\frac{\beta}{2}\hat{\mathbf{H}}_0}$ and normalized leading to $\psi(\frac{\beta}{2}, \hat{\mathbf{R}})$.

Table 4.1: The notations used herein

number of grid points	N
number of bath modes	M
dimension of $\mathcal{H}_S \otimes \mathcal{H}_B$	$L = N \cdot 2^M$
number of eigenstates in the direct averaging	J
number of random phase sets	K

3. The resulting wavefunction is propagated for a random real period $e^{-i\hat{\mathbf{H}}_0\tau}$ leading to $\psi(\tau, \frac{\beta}{2}, \hat{\mathbf{R}})$. The random time is chosen to be on the same order as the simulation periods ($\tau \sim t_{sim}$).

4. The wavefunction is then used as an initial state for the dynamical simulation where the propagation includes the effect of the external field $e^{-i\hat{\mathbf{H}}\Delta t}$.

5. The process (1-4) is repeated and averaged.

4.1.3 Numerical scaling

The required computational resources in CPU time of the different thermal averaging methods determines their applicability. The framework for estimating the numerical scaling of the simulation is set by the energy range $\Delta E_{range} = E_{max} - E_{min}$ and the time scale t_{sim}. The elementary step of the simulation is to perform the operation of the Hamiltonian on the wavefunction $\phi = \hat{\mathbf{H}}\psi$. When the Fourier method is used for the primary system, and the Surrogate Hamiltonian method for the bath, the scaling of this elementary step becomes $O(L \log L) = O(2^M M \cdot N \log N)$ [3].

The zero temperature simulation will serve as a reference to the cost of thermal averaging. There are two steps to the calculation. The first is finding the lowest energy state. This can be done by propagation in imaginary time τ. It is sufficient considering the required energy resolution to propagate to a time scale of $\tau = t_{sim}$. The number of propagation steps would be $n \approx \frac{1}{2}\sqrt{t_{sim} \cdot \Delta E_{range}}$ [114]. The simulation itself would require a larger number of propagation steps of the order of $n \approx \frac{1}{2} t_{sim} \cdot \Delta E_{range}$. The simulation effort will therefore scale as: $O(2^M M \;\; N \log N \;\; t_{sim} \cdot \Delta E_{range})$ or as $O(M 2^M) \;\sim O(2^M)$ with the number of bath modes.

For finite temperature the numerical effort of the direct approach requires obtaining J eigenfunctions and in addition J real time propagations for a period t_{sim} of each eigenvalue. J is determined by the condition that the Boltzmann weight is smaller than a tolerance $e^{-\beta E_J}/Z \ll \epsilon$. Assuming an even distribution of eigenvalues $E_J \approx \Delta E_{range} J/L$, leads to the estimation of J:

$$J \approx 1 + \frac{-k_b \log(\epsilon\ Z)}{\Delta E_{range}}\ L\ T \tag{4.12}$$

In Eq. (4.12) J scales linearly with temperature T and exponentially $O(2^M)$ with the number of bath modes. If J is small i.e. $J \leq 200$, the total numerical cost is J times the cost of the zero temperature calculation. This means that the numerical cost should scale as $O(2^{2M})$. When J becomes large the cost of obtaining the J eigenfunctions overcomes the cost of propagation. The numerical scaling of eigenfunction selection becomes proportional to $\sim J^3$ leading to an exponential scaling of $O(2^{4M})$ with respect to the number of bath modes. This is the reason that the direct method is practically restricted to low temperature simulations.

The numerical effort of the random phase thermal wavefunction method is split into the computation cost of obtaining the thermal wavefunction and cost of the K propagations of the wavefunction to obtain the thermal averaging. Both random method require an initial propagation in imaginary time $\tau = \beta/2$. The numerical effort is small compared to the real time propagation for $t = t_{sim}$. The numerical effort in randomization by real time propagation is approximately equivalent to the propagation effort required in the simulation. $\tau = 10\% t_{sim}$ was found to be sufficient. This means that the numerical effort is K times the effort at zero temperature. The number K can be estimated from Eq. (4.11) and depends on the functional dependence of $\lambda(L)$ on L. In the analyzed result (Cf. Sec. 4.2) it was found that due to self-averaging $\lambda(L)$ is a decreasing function of L. This means that the numerical scaling of the method with respect to the number of bath modes becomes equivalent to the zero temperature case of $O(2^M)$.

4.2 Application to a model problem

The illustrative example chosen to test the methods models a typical simulation of ultrafast spectroscopy in condensed phases. A molecule which is first equilibrated

with its solvent is subject to a short electromagnetic pulse. In the model the molecule is described as a Morse oscillator $V(\hat{\mathbf{X}}) = D(e^{-2\alpha\hat{\mathbf{X}}} - 2e^{-\alpha\hat{\mathbf{X}}})$ with $\hat{\mathbf{X}} = \hat{\mathbf{R}} - \hat{\mathbf{R}}_{eq}$, linearly coupled to the dissipative bath. The bath, assumed to be Ohmic, is described by its spectral density:

$$J(\omega) = \gamma\omega e^{-\omega/\omega_c}. \tag{4.13}$$

The dimensionless parameter γ determines the strength of coupling and ω_c is a cutoff frequency. A finite bath with equally spaced sampling of the energy range was used. The primary system parameters were chosen as $D = 0.05$, $\alpha = 2.0$ $\mu = 10^5$ (all in atomic units).

To simulate directly the absorption spectrum a short electromagnetic pulse is applied to the system. The corresponding electric field has the following time-dependent form:

$$E(t) = \mathcal{E}_0 \sin^2\left[\frac{\pi(t-t_0)}{t_p}\right]\cos(\omega_L t), \tag{4.14}$$

where $\mathcal{E}_0$ is the electric field amplitude, ω_L is the laser carrier frequency, and t_p is the pulse duration. The laser field has the $\sin^2$ form. Other pulse shapes, such a Gaussian resulted in essentially similar results.

The laser parameters were chosen as $\mathcal{E}_0 = 0.001$ a.u. and $t_p = 1000$ fs. The temperature was chosen to be relatively high $k_bT = \omega_0$ ($\omega_0 = \alpha\sqrt{2D/\mu}$), so that at least several of the vibrational energy levels are populated.

4.2.1 Power Absorption

The thermal averaged absorption spectrum was calculated using the methods described above. A non-perturbative direct method is employed applicable to strong or weak fields. The power absorbed or emitted from the radiation field is given by the expectation value [154]:

$$\mathcal{P} = \left\langle \frac{\partial\hat{\mathbf{H}}_{int}}{\partial t} \right\rangle = \mathsf{tr}_S\left\{\hat{\boldsymbol{\rho}}_S \frac{\partial\hat{\mathbf{H}}_{int}}{\partial t}\right\} \tag{4.15}$$

To obtain the total energy ΔE absorbed by a pulse, Eq. (4.15) is integrated for the total pulse duration. By varying the carrier frequency ω_L of the pulse and calculating ΔE, a spectrum of absorbed energy vs frequency was obtained.

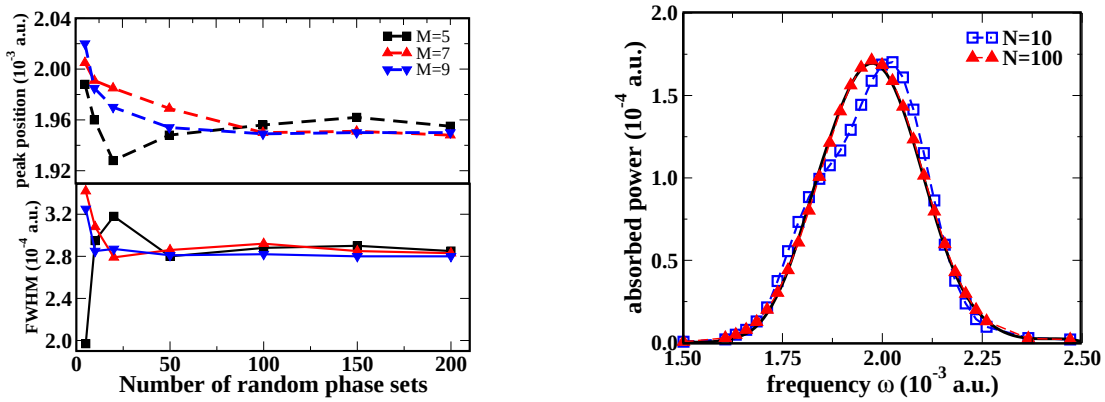

Figure 4.2: Convergence of the total absorbed power of the pulse with number of random phase sets. The peak position (top) and FWHN (bottom) of the pulse are shown. The calculations are made for different numbers of bath modes. The thermal averaged absorption is shown for $M = 7$(right). The solid line refers to the thermal average using the energy eigenstates. The dashed lines with squares and triangles refer to average over 10 and 100 random phase sets, respectively.

The bath parameters were chosen as $\gamma = 4.0$ and $\omega_c = 1.5\omega_0$ and with a 5-modes bath ($M = 5$), the Surrogate Hamiltonian method converges to a timescale of the pulse duration.

As a reference, the power was calculated directly by finding the first J eigenfunctions of H_0. The simulation including the pulse was run for each eigenfunction and Boltzmann averaged.

For $M = 3$ and $k_bT = \omega_0$ the required number of eigenstates $J \approx 30$, however, for $M = 9$ bath $J \approx 1420$.

The direct thermal averaging results were then compared with the random phase thermal wavefunction results. The convergence of the absorbed power with K random phase sets is shown in Fig. 4.2. For $K > 50$ the agreement between two calculations is quantitatively good. The random nature is demonstrated in Fig. 4.3 showing that the statistical error decreases linearly with $1/\sqrt{K}$. The function $\lambda(L)$ Eq. (4.11) which measures the self-averaging property is shown in Fig. 4.3. The best power dependence fit through the data $\lambda(L) \sim L^{\gamma}$ is found to be $\gamma \approx \frac{1}{2}$, ($0.45 \pm 0.09$ for $k_bT = \omega_0$). which means that the observable $\mathcal{P}$ is self-averaging.

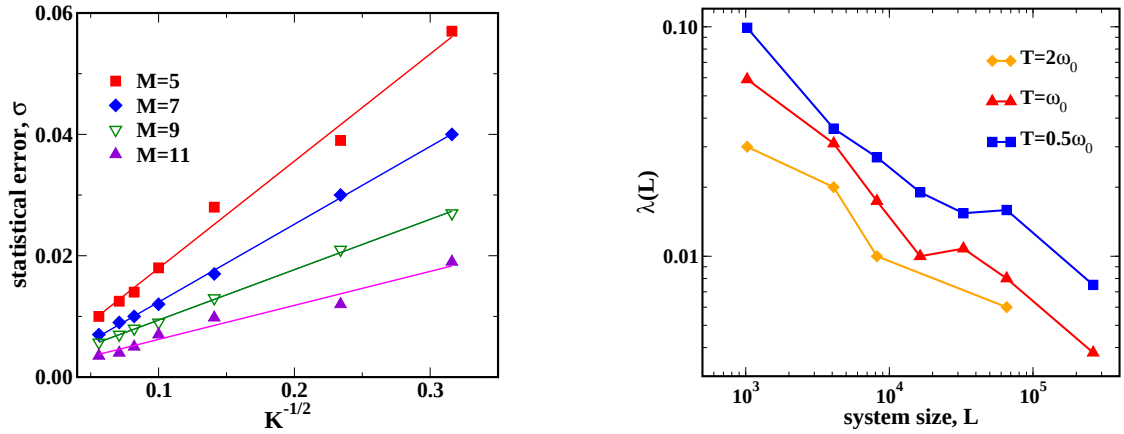

Figure 4.3: (Left) The error $\sigma(\mathcal{P})/\langle\mathcal{P}\rangle$ in the power absorbed at ω_{max} as a function of $K^{-1/2}$, where K is the number of random phase sets. The calculations are made for an increasing number of bath modes. (Right) The function $\lambda(L)$ versus the system size for two different temperatures.

4.2.2 Correlation functions

The dipole correlation function is a more stringent test since it depends directly on the dephasing rate. The dipole autocorrelation function was calculated using the Surrogate Hamiltonian without explicitly including the external field:

$$C(t) = \mathrm{tr}_S \left\{ \hat{\boldsymbol{\rho}}_S \hat{\mathbf{M}} \right\}, \tag{4.16}$$

where $\hat{\mathbf{M}} = \hat{\boldsymbol{\mu}}^* e^{-i\hat{\mathbf{H}}t} \hat{\boldsymbol{\mu}} e^{i\hat{\mathbf{H}}t}$ and $\hat{\boldsymbol{\mu}} \propto \hat{\mathbf{X}}$ is the actual dipole function.

Fig. 4.5 shows the dipole autocorrelation function calculated by Eq. (4.16) for finite temperature. The initial state for the time propagation was chosen as a random phase thermal wavepacket. Then, the initial state was operated on by the position operator of the oscillator and then was propagated in time. The calculations were performed with an increasing number of the bath modes which progressively pushed the converged part of the approximation to longer times. The thermal averaging was performed using an increasing number of the random phase sets. Reasonably accurate results were obtained with $K = 100$ random phase sets.

Fig. 4.4 shows the the expectation value of the position $\hat{\mathbf{X}}$ of the oscillator after applying the short pulse. The pulse duration was chosen as $t_p = 500$ fs. The bath parameters are the same as with the previous calculations. The convergence was obtained for a relatively large number of sets.

A comparison of the scaling of the numerical effort between the direct and random methods is shown in Fig. 4.6. The total power absorbed by the system at ω_{max} was

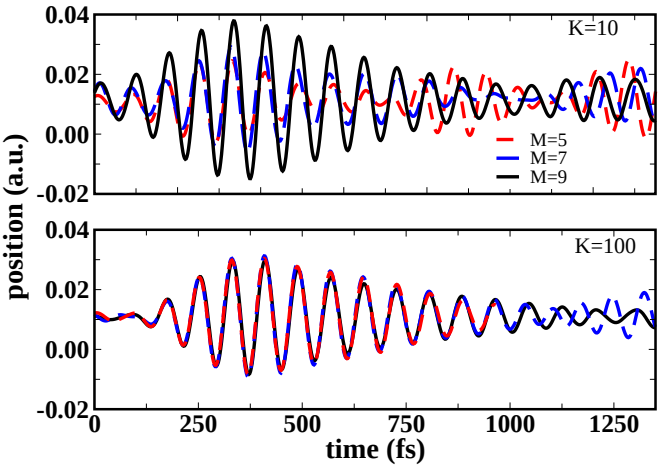

Figure 4.4: The expectation value of the position operator vs time. The dynamics is shown for an increasing number of bath modes (M=3,5,7). Upper and lower panels correspond to averaging over a different number of random phase sets (10 and 100 respectively).

calculated for two different temperatures and an increasing number of bath modes. The direct thermal averaging shows the expected increase in the numerical effort with the number of bath modes, as well as the increase of numerical effort with temperature. In particular, the number of J grows linearly with increasing the system size L and the temperature T. However, for a larger number of the bath modes $M > 11$, the cost of obtaining the J eigenfunctions should overcomes the cost of propagation. Thus, the total CPU time in the direct method will grow as $O(L^3)$.

The numerical effort required by the random phase method depends on the desired accuracy. The number of the propagations K that are necessary to achieve a given accuracy σ depends on the system size L and the temperature T. Determining $\lambda(L)$ by fitting Eq. (4.11) to the simulated data Cf. Fig. 4.3, we found that $K(L)$ decreases with L as $K(L) \sim L^{-1/2}$. This means that, in order to achieve a constant statistical error in the simulation results when the system size L is increased, the number of random phase sets K is decreased. It follows that for large system size i.e. a large number of the bath modes M and for high temperature the random phase simulation will always require less CPU time than the direct method. According to Fig. 4.6 for $k_bT = \omega_0$, the random method becomes more efficient for $M > 6$, and when $k_bT = 0.5\omega_0$ for $M > 7$. The two alternative ways for constructing the random wavepacket gave similar results. The additional computational effort required in method **B** to randomize the phase by real time propagation was found

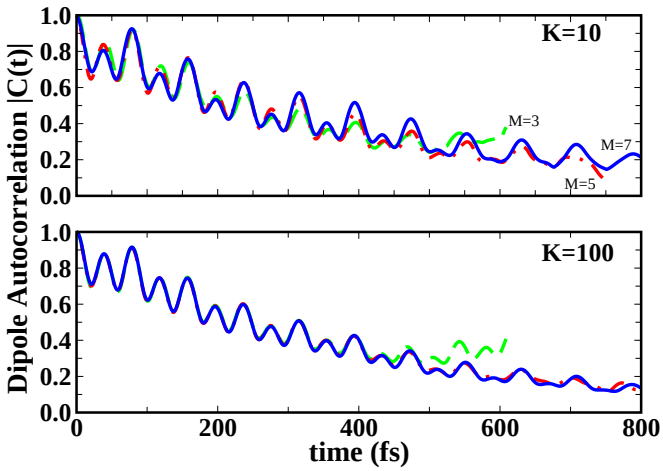

Figure 4.5: The absolute value of the dipole autocorrelation function for the relaxing Morse oscillator coupled to the Ohmic bath. The dynamics is shown for an increasing number of bath modes (M=3,5,7). Upper and lower panels correspond to averaging over a different number of random phase sets (K=10 and K=100 respectively).

to be insignificant.

A dominant source of computational error in the random phase method is associated with the choice of the initial wavefunction. This wavefunction should consist of equal amplitude of all the states of the combined Hilbert space $\mathcal{H}_S \otimes \mathcal{H}_B$. Good results were obtained by choosing an initial wavefunction as a δ function in coordinates that is located at the minimum of the potential while each spinor component has an equal amplitude and a different phase. The numerical tests also confirm that the actual CPU times follow the scaling arguments.

4.3 Conclusions

In this Chapter we introduced the new method for calculating thermal-averaged observables within the Surrogate Hamiltonian approach. The method is based on a random phase superposition of all states in the combined Hilbert space $\mathcal{H}_S \otimes \mathcal{H}_B$. By averaging the sum of projections of these superpositions the identity operator can be reconstructed for any basis set. By applying the thermal propagator $e^{-\frac{\beta}{2}\hat{\mathbf{H}}_0}$ to this state, a thermal wavefunction is produced. This pure state serves as an initial state for the time propagation and for the evaluation of the primary system observables. Averaging of many random phase sets leads to the thermal averaged observables.

The random phase method was tested for the model of a Morse oscillator in

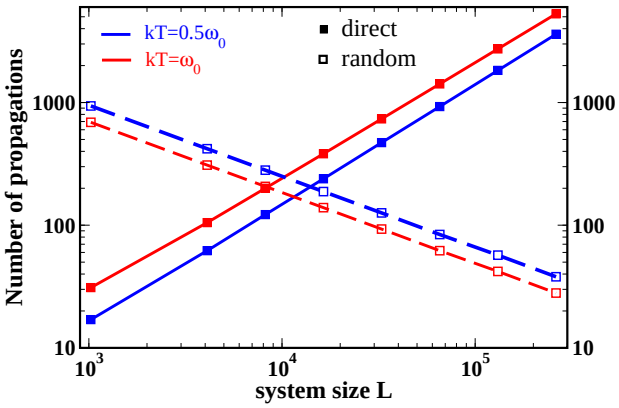

Figure 4.6: The numerical effort measured as the number of propagations J or K required for thermal averaging vs the system size L. The figure relates to the power absorbed at ω_{max}. The temperatures used were $k_bT = \omega_0$ (squares) and $k_bT = 0.5\omega_0$ (triangles). The solid lines refer to the direct method. The dashed lines refer to the number of random phase sets K needed to obtain the converged results with an accuracy of 1%.

equilibrium with an Ohmic bath, perturbed by a short pulse. The absorbed power and dipole correlation function were calculated for a relatively high temperature with an increasing number of bath modes. The results obtained from the random phase thermal averaging were compared with the results from a direct averaging using the eigenstates of the combined system-bath.

The scaling of the computation effort with the temperature and the number of bath modes is more favorable for the proposed random method compared to direct thermal averaging over the energy eigenstates. Comparable results are obtained by repeating a relatively small number of propagations. In addition since the random phase wavepacket can be expanded in any set of states, the calculation of the energy eigenstates becomes unnecessary.

An interesting issue is the source of the observed self-averaging. The numerical tests indicate that the size of the statistical pool is $\sim K \cdot L$, meaning that there is a strong self-averaging proportional to the number of states in the Hilbert space. A possible reason is the local character of the observables, which depend only on the primary systems operators. For sufficiently strong system-bath coupling we found that the eigenvalue spacing distribution obeys Wigner's semicircular law [155]. Such densities of states appear in systems consisting of a spin coupled to a bath of spins (for instance, in NMR) or in models with an environment described by random matrices [149]. In the latter the dynamics of the primary system has been found

self-averaging. For a weak system-bath coupling a Poisson spacing distribution was found and the self-averaging phenomenon was less pronounced.

To summarize our findings, the random phase method obtains converged results for thermally averaged observables by averaging a relatively small number of randomly chosen initial states. Moreover the number of initial states K required to obtain convergence is a decreasing function of the system size L for the strong system-bath coupling and decreases with temperature. This finding means that the Surrogate Hamiltonian method has the same scaling properties for the zero temperature simulation as for the finite temperature simulations. Moreover the finite temperature simulations can be run in parallel since each random phase run is independent of the others. As a consequence, the Surrogate Hamiltonian method can be applied practically for moderate temperature simulations, when the bath modes do not saturate.

The present thermal random phase method is not restricted to the Surrogate Hamiltonian approach. The basic construction is representation-independent. Therefore, the random phase method could be applied the same as to numerical simulations of spin-bath decoherence [156]. The method could also be used for thermal averaging in the multi-configuration time-dependent Hartree application to dissipative dynamics [119, 157].

Chapter 5

Dissipative dynamics of a system passing through a conical intersection

The Surrogate Hamiltonian method allows the analysis of multidimensional systems without restricting the potential shape. Early applications of the method [88, 93–96], as well as the models presented in the preceding chapters, considered a one-dimensional primary system coupled to a dissipative environment. Indeed, some chemical processes can be described in terms of dynamics of the nuclei on a single Born-Oppenheimer potential-energy surface (PES). However, the chemistry of numerous systems involves nuclear dynamics on a few multidimensional excited PESs. As a result, the Born-Oppenheimer (BO) [158] adiabatic separation of nuclear and electronic motions is almost certain to fail. Processes in which the BO approximation breaks down are known as *nonadiabatic* processes. Typical examples of nonadiabatic phenomena include the nonradiative relaxation of excited electronic states, photo-induced unimolecular decay and isomerization processes of polyatomic molecules.

The most complicated nonadiabatic processes involve conical intersections [103, 104]. These can exist in any dimensionality greater than one, so the simplest is a two-dimensional conical structure. Here the symmetry is such that the diabatic curves cross in an (n-1) dimensional seam. In the adiabatic representation, the curves actually cross at a single point, because of the symmetry (odd in one of the coordinates)

of the vibronic coupling. More complicated structures (higher-dimensional conical intersections, asymmetric conical intersections, pairs or clusters of conical intersections) can also occur. They are common for larger organic molecules [107, 159, 160], and they offer complex higher order mixing patterns in the dynamics.

Early attempts to treat nonadiabatic dynamics were based on the Landau-Zener approach [106, 161–163], where motion along one coordinate modulates the nonadiabatic transition among electronic states. While the coupling is most easily envisaged along one coordinate, generalizing the Landau-Zener approach to multiple coordinates lies at the heart of contemporary models for electron transfer [164] and for nonradiative decay [165]. These models, however, fail to provide results for transition rates, which are in quantitative agreement with the experimental data. Experimental studies using ultrafast laser techniques have measured the recovery of the bleach (the time scale of a complete photocycle) resulting in sub-picosecond time scales [166–169].

Because of the different geometry of curve crossing between isolated Landau-Zener avoided crossings and higher-dimensional conical intersections, population transfer can be very rapid in the conical case. This has led to the original interest in conical intersections, and it has been studied extensively, particularly using density operator methods [108, 109, 170–172]. The organic literature [107, 173] frequently uses conical intersections to discuss sub-picosecond transitions.

Most theoretical analyses of conical intersections use either two or three nuclear modes [108]. Electronic populations can then show ultrafast behavior returning to the ground electronic state, and some aspects of an intramolecular vibrational relaxation (IVR) and phase loss can also be understood. But the fundamental behavior of conical intersections in molecules larger than triatomic arises from the presence of multiple modes, and explicit treatment of multiple modes remains difficult. There is an exemplary analysis of a twenty-four mode dynamics model for pyrazine [174], as well as calculations utilizing the Redfield [18, 19] approach to deal with the rest of the vibrational modes as comprising a harmonic bath [175, 176].

In order to properly investigate nonadiabatic processes, the Surrogate Hamiltonian should be extended to at least two dimensions. The following Chapter considers the simplest model of a symmetry-allowed conical intersection, which includes two

electronic states and two vibrational modes. In addition to the Surrogate Hamiltonian, the dissipation is treated within the Lindblad formalism of semi-group dynamics [16, 42, 43]. This allows a direct comparison of the two simulation methods on the same model in order to elucidate the validity of those approaches.

Most studies of nonadiabatic processes involving conical intersections consider the overall electronic populations of the excited and the ground electronic states [108,170,177,178]. A question that naturally occurs is how the population dynamics is monitored experimentally. In our work, we focus on decay of photoexcited states, and on the experimental observables of pump/probe spectra such as recovery of the bleach. All of these are governed not only by the population dynamics, but also by the value of the transition dipole moment and by the energy redistribution. Hence it is necessary to deal not only with the electronic state population, but also with the energy distribution. As a result, in nearly all cases we have (in addition to the curve crossing problem) an IVR issue - the system must return to the starting configuration for the bleach recovery to be observed, and back transfer (re-crossing) can occur in the excited state, unless either IVR or effective dephasing make such recurrences impossible.

In order to deal with these questions, our model employs transient modulations of optical observables, which are the direct signature of the ultrafast dynamics measured in the pump-probe experiments. The use of the Surrogate Hamiltonian has the advantage of a consistent treatment of initial correlations between the system and the bath, as well as explicit description of the pulse field and its influence on the system-bath interactions. The non-perturbative approach is employed to describe the dynamics induced by the pump pulse, while the weak probe is treated within a perturbative picture. This allows us to associate a quantum mechanical window operator to the absorption of the probe pulse centered at a certain time t. The stimulated emission and absorption are calculated as expectation values of this window operator. The present modeling of the pump-probe experiment enables us to investigate the population dynamics, as well as the energy distribution during the nonadiabatic dynamics.

5.1 Theory

5.1.1 Model

We consider a primary system immersed in a bath. The Hamiltonian of such a combined system is given by:

$$\hat{\mathbf{H}} = \hat{\mathbf{H}}_S \otimes \mathbb{1}_B + \mathbb{1}_S \otimes \hat{\mathbf{H}}_B + \hat{\mathbf{H}}_{SB} + \hat{\mathbf{H}}_{SF}(t) \ , \tag{5.1}$$

where $\hat{\mathbf{H}}_S$ is the Hamiltonian of the primary system, $\hat{\mathbf{H}}_B$ - the bath Hamiltonian and $\hat{\mathbf{H}}_{SB}$ describes the interaction between the system and the bath. The time-dependent interaction of the system with the external electromagnetic field is represented by $\hat{\mathbf{H}}_{SF}(t)$.

In the context of conical intersections, the bath may describe a condensed-phase environment, as well as the molecule's inactive modes.

Let us consider the simplest model of a symmetry-allowed conical intersection [103,104,179]. It includes two electronic states g and e, and two vibrational modes: the totally symmetric Q_0 (also called the tuning mode), and the symmetry-breaking (coupling) mode Q_c, which is responsible for vibronic coupling [170]. Employing a diabatic electronic representation, the system Hamiltonian can be written as

$$\hat{\mathbf{H}}_S = \begin{pmatrix} \hat{\mathbf{H}}_g & V_d(\hat{\mathbf{Q}}_c) \\ V_d(\hat{\mathbf{Q}}_c) & \hat{\mathbf{H}}_e \end{pmatrix} \otimes \mathbb{1}_B \ , \tag{5.2}$$

with $\hat{\mathbf{H}}_{g/e} = \hat{\mathbf{T}} + V_{g/e}(\hat{\mathbf{Q}}, \hat{\mathbf{Q}}_c)$. $\hat{\mathbf{T}}$ is the kinetic energy operator, V_g and V_e are the potential energy operators on the ground and excited electronic states respectively, and V_d is the diabatic coupling. The $\hat{\mathbf{Q}}_c$, $\hat{\mathbf{Q}}_0$ are chosen to be dimensionless.

It is customary to choose a linear form for the diabatic coupling term:

$$V_d(\hat{\mathbf{Q}}_0, \hat{\mathbf{Q}}_c) = \Lambda \ \hat{\mathbf{Q}}_c \ \ , \tag{5.3}$$

which is appropriate in the vicinity of the conical intersection. Since diabatic coupling functions obtained from *ab initio* calculations turn out to be localized [180,181], the more physically motivated choice is a coupling term modulated by a damping Gaussian:

$$V_d(\hat{\mathbf{Q}}_0, \hat{\mathbf{Q}}_c) = \Lambda \ \hat{\mathbf{Q}}_c \ \ \mathrm{e}^{-(\hat{\mathbf{Q}}_0 - Q_{CI})^2/\sigma^2 - \hat{\mathbf{Q}}_c^2/\sigma^2} \tag{5.4}$$

where Q_{CI} is the point at which the conical intersection occurs along the symmetric mode Q_0. Thus the diabatic coupling is damped out as one moves away from the conical intersection point [95,182]. Complications will arise if the conical intersection is close to the Franck-Condon region, which will lead to interferences with the light induced excitation dynamics. This possibility will be excluded in the present study.

The coupling with the radiation is described by the semiclassical time-dependent Hamiltonian

$$\hat{\mathbf{H}}_{SF} = \begin{pmatrix} 0 & -\epsilon(t)\hat{\boldsymbol{\mu}}_{tr} \\ -\epsilon^*(t)\hat{\boldsymbol{\mu}}_{tr} & 0 \end{pmatrix} \otimes \mathbb{1}_B \ , \tag{5.5}$$

where $\hat{\boldsymbol{\mu}}_{tr} = \hat{\boldsymbol{\mu}}_{tr}(\hat{\mathbf{Q}}_0, \hat{\mathbf{Q}}_c,)$ is the electronic transition dipole operator, which is a function of the nuclear configuration. $\epsilon(t)$ is the time-dependent electric field. In the large wavelength limit the spatial dependence of $\epsilon(t)$ is ignored.

5.1.2 The interaction between system and bath within the Surrogate Hamiltonian method

The interaction between system and bath is described by the Hamiltonian $\hat{\mathbf{H}}_{SB}$, which can be decomposed into a sum of products of system and bath operators without loss of generality. The system-bath interaction $\hat{\mathbf{H}}_{SB}$ can be partitioned into terms describing different physical processes. The most general bilinear form for vibrational relaxation is given by the operator:

$$\hat{\mathbf{H}}^{vr}_{SB} = \begin{pmatrix} f_g(\hat{\mathbf{Q}}_0, \hat{\mathbf{Q}}_c) & 0 \\ 0 & f_e(\hat{\mathbf{Q}}_0, \hat{\mathbf{Q}}_c) \end{pmatrix} \otimes \sum_{\alpha=0,c} \sum_{i}^{N} \lambda_i^{\alpha} (\hat{\boldsymbol{\sigma}}_i^{\alpha+} + \hat{\boldsymbol{\sigma}}_i^{\alpha}) \ , \tag{5.6}$$

where $f(\hat{\mathbf{Q}}_0, \hat{\mathbf{Q}}_c)$ is a function of the system coordinate(s) operator. The system-bath coupling can vary between the ground and the excited potentials.

In the weak system-bath coupling regime the influence of the bath on the primary system is fully characterized by the spectral density function $J(\omega)$ [7]:

$$J_\alpha(\omega) = \sum_i |\lambda_i|^2 \delta(\omega - \omega_i) \ , \tag{5.7}$$

Use of the density of states $\rho(\omega_i) = (\omega_{i+1} - \omega_i)^{-1}$ in place of the delta function in Eq. 5.7 determines the coupling constants [84, 102]:

$$\lambda_i = \sqrt{J(\omega_i)/\rho(\omega_i)} \ , \tag{5.8}$$

Within the Surrogate Hamiltonian method, it is straightforward to introduce into the model different system-bath interaction mechanisms, such as electronic and vibrational pure dephasing. The process of dephasing corresponds physically to fluctuations in the values of the system energies - electronic dephasing is then the fluctuation in the electronic energy levels, while vibrational dephasing describes changes in the vibrational energies. A qualitative picture of pure dephasing is based on an almost elastic exchange of energy between bath modes, which alters the accumulated phase of the system. For electronic dephasing, the bath modulates the electronic excitation:

$$\hat{\mathbf{H}}_{SB}^{ed} = \Delta_V(\hat{\mathbf{Q}}_0, \hat{\mathbf{Q}}_c)\frac{1}{2}\begin{pmatrix} -1 & 0 \\ 0 & 1 \end{pmatrix} \otimes \sum_{ij} c_{ij}^{ed}(\hat{\boldsymbol{\sigma}}_i^+ \hat{\boldsymbol{\sigma}}_j + \hat{\boldsymbol{\sigma}}_j^+ \hat{\boldsymbol{\sigma}}_i) \; . \tag{5.9}$$

$\Delta_V(\hat{\mathbf{Q}}_0, \hat{\mathbf{Q}}_c)$ is the difference potential describing the dependence of the modulation on the nuclear displacement. The coefficients c_{ij} are biased to represent almost elastic encounters,

$$c_{ij} = \bar{c}_e \, \mathsf{e}^{-\frac{(\omega_i - \omega_j)^2}{2\sigma_\omega^2}} \; , \tag{5.10}$$

with $\bar{c}_e$ a global dephasing parameter, and σ_ω determines the inelastic width. The dephasing rate is proportional to the square of the band width of c_{ij} [95].

For vibrational dephasing, the bath modulates the vibrational Hamiltonian:

$$\hat{\mathbf{H}}_{SB}^{vd} = \begin{pmatrix} \hat{\mathbf{H}}_g & 0 \\ 0 & \hat{\mathbf{H}}_e \end{pmatrix} \otimes \sum_{ij} c_{ij}^{vd}(\hat{\boldsymbol{\sigma}}_i^+ \hat{\boldsymbol{\sigma}}_j + \hat{\boldsymbol{\sigma}}_j^+ \hat{\boldsymbol{\sigma}}_i) \; . \tag{5.11}$$

In order to activate a pure dephasing process, the bath modes must be initially populated.

5.1.3 Reduced dynamics in the density operator representation

We introduce in this section a brief description of the semigroup approach, which is applied to the problem of dissipative dynamics of conical intersection in addition to the Surrogate Hamiltonian method, described earlier.

The reduced dynamics approach is constructed to avoid the size scaling of a full treatment, allowing a computational scheme able to simulate a dynamical encounter

from first principles. The equations of motion are solved explicitly for a primary system, while the bath is treated implicitly. The approach requires equations of motion for the subsystem which are based on Lindblad formalism of semi-group dynamics [16,42,43]. One advantage of the semi-group approach is that the computational cost scales linearly with the propagation time, unlike the exponential scaling of the the Surrogate Hamiltonian. A disadvantage is that it is formulated in Liouville space, which squares the number of required representation points in comparison to a wave function description of the Surrogate Hamiltonian method. In addition, there is a hidden assumption [25] of an uncorrelated initial state of the system and the bath. In the Markovian limit, under the conditions of the complete positivity, the reduced equation of motion can be diagonalized to the Lindblad form [16,42,43]:

$$\frac{d}{dt}\hat{\boldsymbol{\rho}}_S = -\frac{i}{\hbar}\left[\hat{\mathbf{H}}_S, \hat{\boldsymbol{\rho}}_S\right] + \sum_j \left(\hat{\mathbf{F}}_j \hat{\boldsymbol{\rho}}_S \hat{\mathbf{F}}_j^+ - \frac{1}{2}\{\hat{\mathbf{F}}_j \hat{\mathbf{F}}_j^+, \hat{\boldsymbol{\rho}}_S\}\right) , \tag{5.12}$$

where $\hat{\mathbf{F}}_j$ are the Lindblad operators, representing the influence of the environment. $\{\hat{\mathbf{A}}, \hat{\mathbf{B}}\} = \hat{\mathbf{A}}\hat{\mathbf{B}} + \hat{\mathbf{B}}\hat{\mathbf{A}}$ is the anticommutator.

The nature of the bath is implied in the formulation of a specific Lindblad operator. Such operators can be constructed to display vibrational and electronic dissipation [183] of the system in baths of different physical natures. The rate of dissipation is derived from the nature of the bath and the system-bath coupling.

The choice $\hat{\mathbf{F}}_{vd} = \frac{\sqrt{\gamma_{vd}}\phi}{\hbar}\hat{\mathbf{H}}$ dictates pure vibrational dephasing of the system (γ_{vd} is the rate and ϕ is the phase shift in time). $\hat{\mathbf{F}}_{ed} = \sqrt{\gamma_{ed}}(|e\rangle\langle e| - |g\rangle\langle g|)$ represents electronic dephasing [184]. For physical reasons we chose the electronic dephasing operator to be in the diabatic representation. The reason is that the major interaction with the environment is induced by the transition dipole of the molecule, proportional to $(|e\rangle\langle e| - |g\rangle\langle g|)$ in the Condon approximation and the diabatic representation.

Quantum intramolecular vibrational relaxation is achieved using equations of motion [185,186], which are consistent with complete positivity:

$$\begin{aligned} \tfrac{d}{dt}\hat{\boldsymbol{\rho}}_S &= -\tfrac{i}{\hbar}\left[\hat{\mathbf{H}}, \hat{\boldsymbol{\rho}}_S\right] - \tfrac{i}{2\hbar}\gamma\left[\hat{\mathbf{q}}, \{\hat{\mathbf{p}}, \hat{\boldsymbol{\rho}}_S\}\right] \\ &-\tfrac{1}{\hbar^2}D_{pp}\left[\hat{\mathbf{q}}, [\hat{\mathbf{q}}, \hat{\boldsymbol{\rho}}_S]\right] - \tfrac{1}{\hbar^2}D_{qq}\left[\hat{\mathbf{p}}, [\hat{\mathbf{p}}, \hat{\boldsymbol{\rho}}_S]\right] - \tfrac{2}{\hbar^2}D_{pq}\left[\hat{\mathbf{q}}, [\hat{\mathbf{p}}, \hat{\boldsymbol{\rho}}_S]\right] , \end{aligned} \tag{5.13}$$

where thermal equilibrium imposes: $D_{pp} = \gamma m k_b T$ and $D_{qq} = \kappa\frac{\gamma\hbar^2}{16 m k_b T}$. p and q are momentum and space variables of the system. The κ is a parameter larger than

one (for $\kappa = 4/3$ the model is Gaussian, and if κ is larger, the model is Poisson-like). A cross diffusion term can be added $D_{pq} = \frac{\gamma\Omega\hbar^2}{12\pi k_b T}$, where Ω is the frequency cutoff parameter.

It should be noticed that D_{ij} terms are independent of the field.

5.1.4 Stimulation of pump-probe experiment and time-dependent observables

From the experimental point of view, the detection of ultrafast nonadiabatic processes becomes possible using femtosecond pump-probe techniques [1, 168, 169, 187–190]. These experiments provide information on the time scales of the processes under investigation. Nevertheless the interpretation of the results remains a non-trivial task. A direct signature of the ultrafast dynamics in such experiments are transient modulations of optical observables, reflecting the promotion of ground and excited state vibrational modes. However, it is generally not possible to define the exact number of electronic states and vibrational modes involved in the nonadiabatic dynamics.

The present study aims to construct a simplified quantum dynamical model, including a conical intersection, and to apply the previously developed tools [95, 132, 191] to simulate the pump-probe experiments.

The Surrogate Hamiltonian simulations start with a fully correlated ground state, determined by propagating an initial guess function in imaginary time [114] with the total system-bath Hamiltonian:

$$\Psi(\hat{\mathbf{Q}};\tau) = \mathrm{e}^{-\frac{\hat{\mathbf{H}}\tau}{\hbar}}\Psi(\hat{\mathbf{Q}};0)\ . \tag{5.14}$$

This initial state is the starting point for launching the pump-probe simulations. The use of the Surrogate Hamiltonian has the advantage of a consistent treatment of initial correlations between the system and the bath, as well as explicit description of the pulse field and its influence on the system-bath interactions. Commonly in most computational studies of nonadiabatic processes, the initial state is prepared by a Franck-Condon transition from the ground state [108]. This choice, however, ignores the system-bath correlations and the dynamical aspects of the pump pulse.

Upon applying the pump pulse, a significant fraction of the population is trans-

fered to the excited state. Since the pump pulse is strong, a non-perturbative treatment is needed. Our model enables us, to include explicitly the interaction between the system and the radiation (5.5). In this study the pump pulse has a Gaussian envelope in time:

$$\epsilon(t) = \epsilon_0 \, \mathsf{e}^{-(t-t_{max})^2/2\sigma_L^2} \, \mathsf{e}^{i\omega_L t} \; , \tag{5.15}$$

and the carrier frequency ω_L is chosen to match the difference between the ground and excited electronic potentials at the minimum of the ground state.

The probe pulse can be applied at any stage in the cycle of events. Typically, the probe pulse is short and weak. It can promote both excitation, leading to the energy absorption and deexcitation, resulting in stimulated emission. In this case a perturbative picture is justified and can save a significant computational effort. The total absorption from the probe pulse by an observable is thus represented by a window operator $\hat{\mathbf{W}}$. This operator describes a finite resolution position measurement [191, 192]:

$$\Delta E \;\approx\; -\hbar\omega_L \, \mathsf{tr}_S\{\hat{\boldsymbol{\rho}}_S(t_p) \cdot \hat{\mathbf{W}}\} \; . \tag{5.16}$$

The observation process is completed in a time duration proportional to the probe pulse duration τ_p. Eq. (5.16) collapses the observation to a single instant of time t_p. By employing time-dependent perturbation theory the window operator for a Gaussian shaped probe pulse becomes [191, 192]:

$$\hat{\mathbf{W}}(\hat{\mathbf{Q}}, \hat{\mathbf{Q}}') = \frac{\pi(\tau_p^2 \epsilon_0^2)}{\hbar^2} e^{-2\Delta(\hat{\mathbf{Q}})^2 \tau_p^2/\hbar^2} \cdot \hat{\boldsymbol{\mu}}^2(\hat{\mathbf{Q}}) \times \delta(\hat{\mathbf{Q}} - \hat{\mathbf{Q}}') \; |\psi_k\rangle\langle\psi_k| \; , \tag{5.17}$$

where $|\psi_k\rangle\langle\psi_k|$ is the electronic projection operator, which selects the ground electronic state for transient absorption. For emission, the projection operator selects the excited electronic state. The window operator, Eq. (5.17), is a function of the probe central frequency ω_L:

$$2\Delta(\hat{\mathbf{Q}}) = V_e(\hat{\mathbf{Q}}) - V_g(\hat{\mathbf{Q}}) - \hbar\omega_L \; , \tag{5.18}$$

i.e. $2\Delta(\hat{\mathbf{Q}})$ is the difference potential relative to the probe frequency. The employment of the window operator assumes a random phase between the pump and probe pulses, eliminating interference effects. An interference between pump and probe excitations is also eliminated once the electronic dephasing is complete. The memory of the pump phase is stored in the transition dipole phase. This is erased

once the relative phase between the ground and excited wave packets is lost by the electronic dephasing [193].

The present modeling of the pump-probe experiment enables us to investigate the population dynamics, as well as the energy distribution during the nonadiabatic dynamics. The dynamics of the excited electronic state is reflected in the stimulated-emission signal. The vibrational relaxation of the hot ground state population, on the other hand, can not be monitored by the time evolution of the vibrational population or the stimulated emission. The transient absorption, however, reflects the energy redistribution, since it shows the returning of the system to its initial configuration. The ground-state absorption bleaching, induced by the pump probe, will exhibit the recovery, reflecting the curve crossing dynamics as well as the subsequent vibrational cooling.

Most studies of nonadiabatic processes involving conical intersections consider the overall electronic populations of the excited and the ground electronic states [108, 170, 177, 178]. In the case of open-system dynamics, the time-dependent population probabilities of the diabatic electronic states are defined as:

$$P_n^{di}(t) = \mathsf{tr}\left\{\hat{\mathbf{N}}_n^{di}\hat{\boldsymbol{\rho}}_S(t)\right\} , \tag{5.19}$$

with $\hat{\mathbf{N}}_n^{di}$ being the projection operator of the nth electronic state in the diabatic representation. The reduced system density operator is defined as a partial trace over the bath degrees of freedom. The adiabatic electronic population is defined in a similar way by using diabatic-to-adiabatic transformation [170].

A question that naturally arises is how the population dynamics is monitored experimentally. This has been the leading argument in studies modeling femtosecond time-resolved experiments in systems incorporating conical intersections [194, 195].

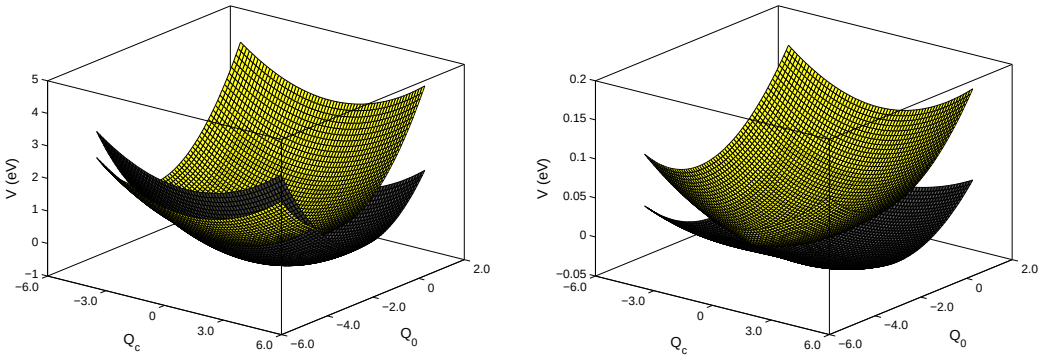

Figure 5.1: Schematic view of the potential energy surfaces in a diabatic (upper panel) and an adiabatic (lower panel) representations. The following parameters are used in the calculations (all in eV): $\omega = 0.074$, $\omega_c = 0.0936$, $\kappa_g = -0.0964$, $\kappa_e = 0.1194$, $\Lambda = 0.18$ $\Delta = 0.4617$ and the coordinates are dimensionless.

5.2 Results and Discussion

5.2.1 General

The diabatic potential energy surfaces are approximated by quadratic functions with linear intrastate couplings [170]. Using dimensionless normal coordinates:

$$V_g(\hat{\mathbf{Q}}_0, \hat{\mathbf{Q}}_c) = -\Delta_0 + \frac{\hbar\omega_0}{2}\hat{\mathbf{Q}}_0^2 + \kappa_g\hat{\mathbf{Q}}_0 + \frac{\hbar\omega_c}{2}\hat{\mathbf{Q}}_c^2 \,, \tag{5.20}$$

$$V_e(\hat{\mathbf{Q}}_0, \hat{\mathbf{Q}}_c) = \Delta_0 + \frac{\hbar\omega_0}{2}\hat{\mathbf{Q}}_0^2 + \kappa_e\hat{\mathbf{Q}}_0 + \frac{\hbar\omega_c}{2}\hat{\mathbf{Q}}_c^2 \,, \tag{5.21}$$

where ω_0 and ω_c are the vibrational frequencies of the totally symmetric mode Q_0 and the coupling mode Q_c respectively. The $2\Delta_0$ denotes the vertical excitation energy and $\kappa_{g/e}$ are the first-order intrastate electron-vibrational couplings.

The system parameters are chosen as follows (all in eV): $\omega_0 = 0.074$, $\omega_c = 0.0936$, $\kappa_g = -0.0964$, $\kappa_e = 0.1194$, $\Delta = 0.4617$ and the coordinates are dimensionless. The inter-state coupling is described as:

$$V_d(\hat{\mathbf{Q}}_0, \hat{\mathbf{Q}}_c) = \Lambda\hat{\mathbf{Q}}_c\, \mathrm{e}^{-(\hat{\mathbf{Q}}_0 - Q_{CI})^2/2\sigma^2} \,, \tag{5.22}$$

with Q_{CI} being the point where the conical intersection occurs along the tuning mode, and σ is the breadth of the coupling function. The coupling strength is $\Lambda = 0.18$ eV. The above geometry corresponds roughly to potential energy surfaces of the $S_1(n\pi^*)$ and $S_2(\pi\pi^*)$ excited states of pyrazine [174,196] along the two normal

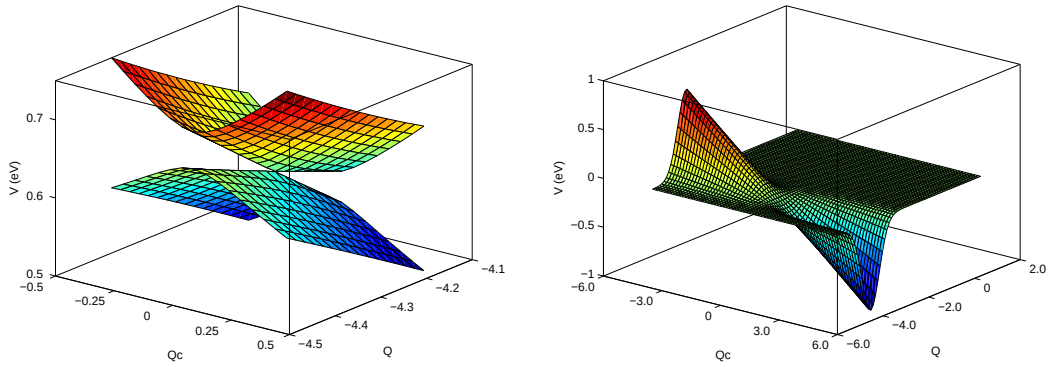

Figure 5.2: (Left) A close view of the conical intersection within the adiabatic representation. (Right) The diabatic coupling V_d, giving by Eq.(5.22).

modes ν_{6a} (the tuning mode) and ν_{10a} (the coupling mode). The ground electronic state S_0 of pyrazine lies about 3.94 eV lower than S_1. Here we use a simplified model with the ground state assumed to be S_1 to introduce the effect of the bleach recovery in a general way.

Fig. 5.1 shows diabatic (a) and adiabatic (b) potential surfaces and Fig. 5.2 shows a close view of the conical intersection in the adiabatic representation, as well as the diabatic coupling, given by Eq.(5.22). The diabatic surfaces cross along the line ($(n-1)$-dimensional seam), while in an adiabatic representation, the potentials touch at a single point $(Q_{CI}, 0)$.

The influence of the bath on the primary system is characterized by the spectral density function $J_\alpha(\epsilon)$. For an Ohmic bath the damping rate is frequency-independent and the spectral density in the continuum limit is given by

$$J_\alpha(\omega) = \eta_\alpha \ \omega \ \ \mathrm{e}^{-\omega/\omega_{cut}^{\alpha}} \tag{5.23}$$

for all frequencies ω up to the cutoff frequency ω_{cut}. The coupling strength η_α for the specific mode is given by the ratio of the damping rate γ and the vibrational frequency of this mode $\omega_{0/c}$. A finite bath with equally spaced sampling of the energy range is used in all calculations. The cutoff frequency is set to $2.5\omega_{0/c}$, which defines the shortest time scale of the bath (about $\tau_{bath} = 20$ fs). The time scale corresponding to the frequency spacing $\Delta\omega$ defines the Poincaré period (τ_{rec}). It should be larger than any other time scale of interest. With ω_{cut} fixed, this time

becomes:

$$\tau_{rec} = \frac{2\pi}{\Delta\omega} = \frac{2\pi N}{\omega_{cut}} \,. \tag{5.24}$$

Thus, with an increasing number of bath modes, the convergence progresses in time. In the present modeling the number of TLS is chosen to be $N = 30-40$ (for different coupling strengths), which ensures that τ_{rec} is greater than the overall simulation time. The calculations were performed in different interaction regimes identified by considering the relevant time scales: the weak coupling referring to $\gamma^{-1} = 750$ fs $\gg \tau_{osc}, \tau_{bath}$; and the intermediate situation characterized by $\gamma^{-1} = 75$ fs $\approx \tau_{osc} > \tau_{bath}$. The temperature of the bath has been neglected in these calculations and chosen to be zero.

The pump pulse envelope is modeled as a Gaussian function of Eq. (5.15) with the intensity ϵ_0 adjusted such that approximately $\sim 10\%$ of the ground state population was transferred to the excited state [191]. The width (FWHM) of the pulse which is connected to σ_L is chosen as 20 fs which is typical for charge transfer experiments [169]. t_{max} is fixed by starting the propagation at $t_0 = t_{max} - 3\sigma_L$. The probe pulse has the same profile as the pump pulse, but with only 10% of the pump intensity.

5.2.2 Simulation of pump-probe experiment

A direct signature of the ultrafast dynamics is provided by transient modulations of optical observables. In the case of the system with two electronic states, the absorption of the probe pulse reflects the dynamics of the ground state, while the stimulated emission signal reveals the dynamics of the excited state. The transient absorption and emission signals and their spectra are displayed in Figs. 5.3-5.4. The emission and absorption signals are plotted as a function of the time delay between the pump and probe pulses. The central frequency of the probe pulse is chosen to be the same as of the pump pulse ω_L. The dynamics of the isolated system ($\eta = 0$) are compared with those with weak vibrational relaxation ($\eta_0 = \eta_c = 0.01$, $\gamma^{-1} = 750$ fs) and medium electronic dephasing ($\bar{c}_e = 0.25$). It was found that pure nuclear dephasing does not affect noticeably the system dynamics on this time scale.

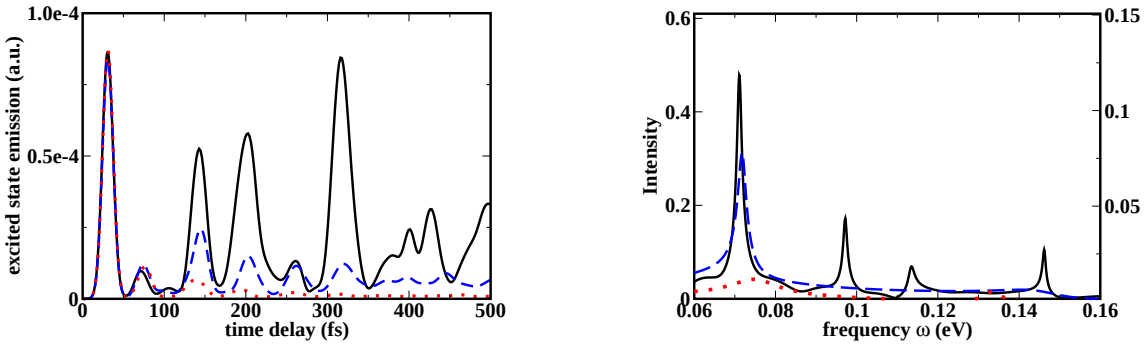

Figure 5.3: Transient stimulated-emission signal (left) and its spectrum (right) for the two-mode system, incorporating a conical intersection. The pump and probe frequencies are chosen to correspond to vertical excitation from the bottom of the ground electronic potential. Solid lines: the isolated system; dashed lines: vibrational relaxation with weak system-bath coupling ($\eta_0 = \eta_c = 0.01, \gamma^{-1} = 750$ fs); dotted lines: vibrational relaxation ($\eta_0 = \eta_c = 0.01$) with medium electronic dephasing ($\bar{c}_e = 0.25$). The number of bath modes is $N = 30$ with two simultaneous excitations allowed. Note the different scale for the spectrum of the isolated system(left ordinate in right panel).

Transient Emission

The excited state dynamics are reflected by the transient emission of the probe pulse (see the left panel of Fig. 5.3). After applying the pump pulse of 20 fs duration, about $\sim 10\%$ of the ground state population has been transfered to the electronic excited state. The excited wave packet starts to evolve and eventually reaches the vicinity of the conical intersection. A nonadiabatic population transfer to the ground state takes place within one vibrational period, which is seen as an initial ultrafast decay of the emission signal (~ 50 fs). The signal for the isolated system (full line) also shows quasi-periodic revivals caused by the nonadiabatic transfer back (re-crossings) to the excited potential state. The coherent motions of the excited wave packet are reflected in the periodic oscillations of the signal.

In the presence of vibrational relaxation (dashed line in Fig. 5.3), the amplitude of the revivals drops down significantly already after 100 fs. However, the initial peak of the emission signal is almost unaffected by the dissipation. In the medium or strong coupling regimes (not shown), the amplitude of the first peak decreases, while the time of its decay (~ 50 fs) remains unchanged. The influence of electronic dephasing (the dotted line in Fig. 5.3) is even more pronounced. Hence the emission signal does not show any quasi-periodic recurrences, caused by the population transfer back to

the excited state. The periodic oscillations are almost damped down after 300 fs.

Following the dynamics, it is found that the vibrational relaxation and the electronic dephasing effectively obstruct the re-crossings of the population to the excited state. As a result the emission signal turns off. The dissipation also damps the coherent motion of the excited wave packet, seen as an increase in the width of the spectrum of the signal.

The spectrum of the emission signal (Fig. 5.3, right) was obtained by using a filter-diagonalization method [115, 116, 197] with data window between 100 and 450 fs. For the isolated system (full line) it shows the first and second harmonics of the tuning mode Q_0 as well as the fundamental of the coupling mode Q_c. The latter indicates that during the internal-conversion process the coupling mode becomes highly excited. These phenomena reflect the strong mixing induced by the conical intersection. Vibrational relaxation and electronic dephasing reduce the emission signal significantly (note the different scale in Fig. 5.3, right panel), by suppressing the re-crossing process. Furthermore, vibrational relaxation leads to a finite width of the peaks, which increases with increasing system-bath coupling. The bath also red shifts the spectrum. Electronic dephasing causes a further broadening of the peaks and an additional red shift. It also diminishes completely the amplitude of the fundamental frequency of the coupling mode.

Transient Absorption

The absorption of the probe (Fig. 5.4, left) reflects the dynamics of the ground electronic state. The transient absorption signal is calculated as the absorption of the probe without the pump pulse subtracted from the absorption of the probe with the pump. The initial decay of the absorption transient (bleach) reveals the loss of ground state population due to the pump pulse. Since the pump pulse excites $\sim 10\%$ of the ground state population to the excited state, the ground state wave packet is only weakly perturbed by the excitation process. However, the "hole" left on the ground electronic state creates a nonstationary density which oscillates periodically with the ground state vibrational frequency [132, 152]. These dynamics can be measured experimentally via impulsive resonance Raman scattering.

The absorption signal for the isolated system (full line) shows primarily the

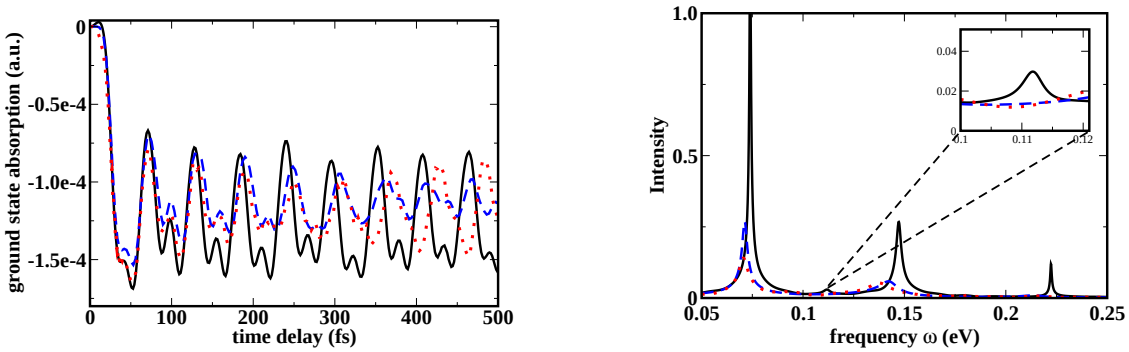

Figure 5.4: Transient absorption signal (left) and its spectrum (right) for the two mode system, involving conical intersection. The pump and probe frequencies are chosen to correspond to the bottom of the ground electronic potential. Solid lines: the isolated system; dashed lines: vibrational relaxation with weak system-bath coupling ($\eta_0 = \eta_c = 0.01, \gamma^{-1} = 750$ fs); dotted lines: vibrational relaxation ($\eta_0 = \eta_c = 0.01$) with medium electronic dephasing ($\bar{c}_e = 0.25$). The number of bath modes is $N = 30$ and two simultaneous excitations are allowed in the surrogate bath.

coherent motion of the remaining ground state wavepacket.

The power spectrum of the absorption signal is given in the right panel of Fig. 5.4. It shows the first, the second and higher harmonics of the symmetric mode Q_0 as well as the weak fundamental of the coupling mode Q_c. Since the pump frequency corresponds to the center of the ground electronic potential, the dynamical hole in coordinate space is produced with reflection symmetry with respect to the minimum point of the potential well. A momentum kick induced by the pump will break this symmetry leading to the appearance of a first harmonic component in the signal [191]. In the presence of dissipation, the fundamental of the coupling mode vanishes, while the harmonics of the symmetric mode are diminished significantly. The vibrational relaxation suppresses the higher harmonics faster. Electronic dephasing diffuses the localization of the hole, causing the peak broadening.

After the excited state wave packet has reached the conical intersection, population is nonadiabatically transferred back to the ground state. Therefore the transient absorption of the probe pulse from the ground state should reflect the increase in population, known experimentally as the "recovery of the bleach" [169]. The newly created population on the ground electronic surface is vibrationally excited and its appearance in the observation window of the probe is delayed by the time scale of vibrational relaxation. The "recovery of the bleach" phenomenon is governed not only by the population dynamics, which indeed happens on sub-picosecond time

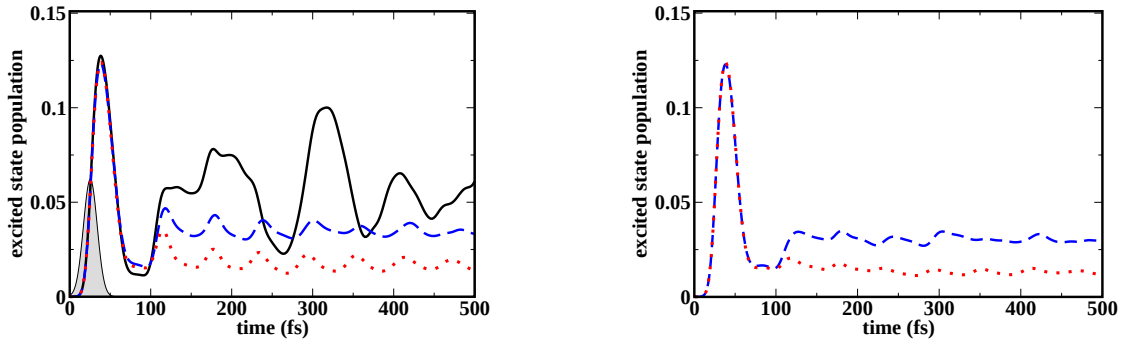

Figure 5.5: Time evolution of diabatic (left) and adiabatic (right) population probability of the excited electronic state. Gaussian laser pulse of $\tau_p = 20$ fs duration and $\omega_L = 1.25$ eV frequency is applied (the envelope of the pulse is shown). Full line: the isolated system ($\eta = 0$); dashed line: vibrational relaxation with weak coupling strength ($\eta_0 = \eta_c = 0.01, \gamma^{-1} = 750$ fs); dotted line: weak vibrational relaxation ($\eta_0 = \eta_c = 0.01$) and medium electronic dephasing ($\bar{c}_e = 0.25$). The number of bath modes is $N = 30$ and two simultaneous excitations are allowed.

scale, but also by the energy redistribution. The system must return to the starting configuration for bleach recovery to be observed. The present model shows that even for moderate vibrational relaxation, no "recovery of the bleach" is observed on the time scale shorter than 500 fs.

Population probabilities

It is interesting to compare the pump-probe signals to the time evolution of the population probabilities of electronic states. These probabilities have been widely considered as an appropriate measure of nonadiabatic dynamics in systems involving conical intersections [108, 170, 177, 178, 195].

The time evolution of the *diabatic* population of the excited state is shown in Fig. 5.5 (left panel). The full lines refer to the dynamics of the isolated system. It exhibits ultrafast decay on a time scale of about 20 fs after the pump pulse has been completed. The population has dropped below 0.02 (note that only $\sim 10\%$ of the ground state population has been transferred by the pump pulse). This initial decay is followed by pronounced quasiperiodic revivals and the population does not decrease any longer.

Similar behaviors have been obtained for a large variety of multi-dimensional systems involving conical intersections [170, 175, 198–200], including the model with an explicit treatment of the intramolecular environment [174]. All these studies

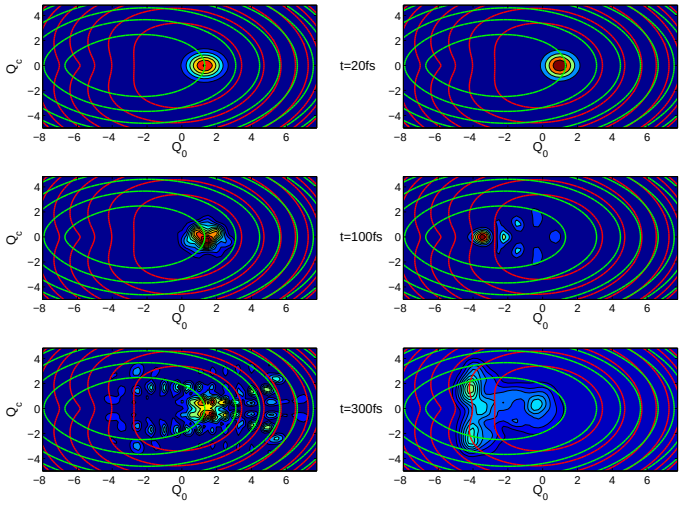

Figure 5.6: The diagonal elements ($Q_n = Q'_n$) of the reduced density matrices in the vibrational coordinate representation $\hat{\boldsymbol{\rho}}_S(Q_0, Q_c; Q'_0, Q'_c;)$ in the adiabatic excited (left panel) and ground (right panel) states. Snapshots are shown at 20 fs (top), 100 fs (middle) and 300 fs (bottom). The red contour lines refer to the adiabatic ground state, while the green contour lines represent the excited state.

use a Franck-Condon excitation initial state, while the present study starts from an equilibrium initial state and the excitation is caused by the ultrafast pulse. For this reason direct comparison is not possible, nevertheless the timescale of population dynamics is of the same order.

The addition of weak ($\eta_0 = \eta_c = 0.01$) vibrational relaxation (dashed line in Fig. 5.5) lowers the amplitude of the revivals and reduces the population in the excited electronic state. In the presence of pure electronic dephasing (dotted lines in Fig. 5.5) the amplitude of the revivals drops down even more significantly. Neither vibrational relaxation nor pure electronic dephasing changes the rate of the initial interstate crossing, meaning that the ultrafast time scale of the electronic population decay is a feature of the system topology, and is only slightly perturbed by the dissipative environment [175].

The time evolution of the adiabatic population of the excited state is shown in Fig. 5.5 (right panel). While the differences from the diabatic picture are minor, in the long-time limit the population decays to a value slightly lower than in the diabatic picture.

The additional decay in the population probability of the excited state (after 100

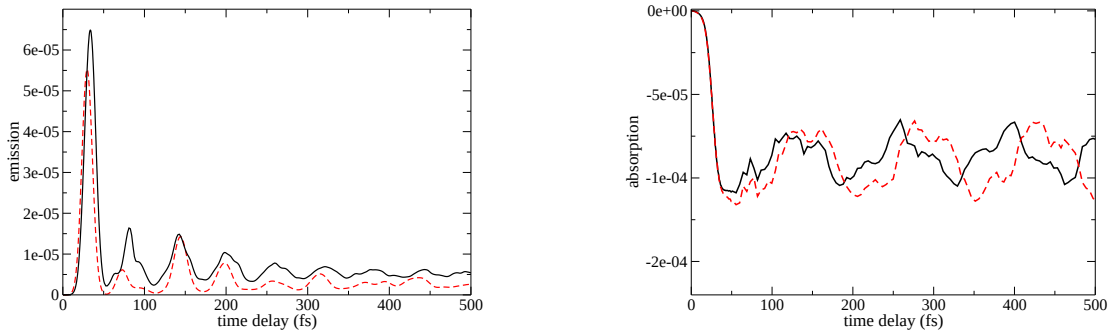

Figure 5.7: The stimulated emission (left) and the transient absorption (right) signals for the two-mode system, containing a conical intersection, are calculated using the Surrogate Hamiltonian (dashed lines) and the semi-group approaches (solid lines). The vibrational relaxation parameters are in the weak system-bath coupling range ($\eta_0 = \eta_c = 0.01, \gamma^{-1} = 1000$ fs);

fs), caused by the coupling to the environment, indeed reflects the fact that high vibrational levels of the electronic ground state are populated in the initial internal-conversion process [175,201]. Vibrational relaxation cools down this population, and together with electronic dephasing prevents an efficient transfer of the population back to the excited state. However, further energy relaxation to lower vibrational levels of the ground state continues on a much longer time scale. The system's returning to its initial configuration, which can be seen experimentally as recovery of the bleach, is not reflected in the early time evolution of the population probabilities.

Fig. 5.6 displays the diagonal elements ($Q_n = Q'_n$) of the reduced density matrix in the vibrational coordinate representation $\hat{\boldsymbol{\rho}}_S(Q_0, Q_c; Q'_0, Q'_c;)$ (in the diabatic electronic representation). It shows the fast disappearance of the excited wave packet via the conical intersection, and its reappearance in high vibrational levels of the lower surface.

The time evolution of the diabatic state population as well as transient modulations of optical observables are indeed affected by the conical intersection. The population probabilities, however, do not reflect the energy redistribution process and the experimentally measured recovery of the bleach.

5.2.3 The Surrogate Hamiltonian method versus the semi-group approach

The differences between the two methods lie in the initial system-bath correlations and the influence of the excitation pulse on the system bath coupling. The construction of the Surrogate Hamiltonian approach is non-Markovian and therefore it is preferable for treatment of ultra-short dynamics at conical intersections. However, in the present study the non-Markovian character of the system-bath interactions hardly affects the dynamics of any of the system's observables. The qualitative features of semi-group dynamics compare well to the Surrogate Hamiltonian approach, as can be seen in Fig. 5.7. The presented results support the finding that for short time dynamics in the weak coupling limit, the two approaches should converge [202].

In the Surrogate Hamiltonian calculations the temperature of the bath has been taken to zero, while in the semi-group approach it is set to a finite (low) value to avoid singularities in the relaxation terms D_{ij}. The temperature effects are negligible in the studied system, due to the large excess of energy coming from the electronic excitation.

From a numerical perspective, the Surrogate Hamiltonian method is advantageous for short simulation times. For example, for dynamical simulations up to 500 fsec 40 bath modes were sufficient to obtain the converged results. The wavepacket calculation was faster than the equivalent density operator propagation. In addition the Surrogate Hamiltonian method treats the excitation process more realistically since it includes implicitly the influence of the external field on the system bath coupling. For longer times the computational effort of the Surrogate Hamiltonian can become prohibitively expensive due to exponential scaling. The semi-group approach is able to simulate long time dynamics with linear scaling with time. This suggest combining the two methods.

In this case the simulation starts using the Surrogate Hamiltonian with a fully correlated system-bath initial state. The Surrogate Hamiltonian is also employed for the pump step, therefore the influence of the field is included. After the pump a reduced system density operator is calculated. This is done by tracing over the bath degrees of freedom from the projection defined by the Surrogate Hamiltonian wavefunction $\hat{\boldsymbol{\rho}}_S = \mathsf{tr}_B \{|\Psi\rangle\langle\Psi|\}$. This density operator is used as an initial state

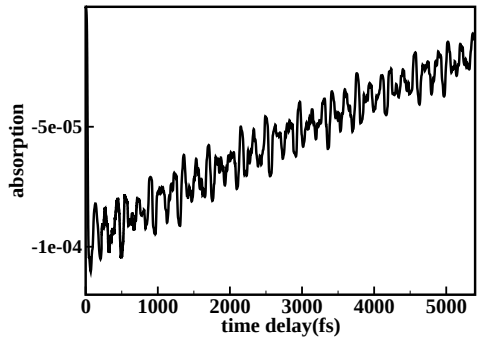

Figure 5.8: The recovery of the bleach: a long time simulation of the transient absorption for the two-mode system with a conical intersection. The Surrogate Hamiltonian is employed to simulate the system's interaction with the pump pulse used to initiate the dynamics. The system reduces density operator was calculated at the end of the pump pulse and then used as an initial state for the rest of the simulation using the semi-group approach. The parameters of the vibrational relaxation are in the range of medium system-bath coupling ($\gamma^{-1} = 500$ fs).

for Liouville dynamical simulation, which can be carried out to longer times. In order to evaluate relaxation parameters entering the Lindblad equation Eq.(5.13), two approaches have been compared in a time-window, in which the dynamics are Markovian.

The above procedure was employed to calculate the recovery of the bleach. The time scale, required to propagate the system to achieve full bleach recovery is in the order of a few picoseconds. Fig. 5.8 shows a monotonic recovery of the bleach on the picosecond time scale obtained from the combined approach.

5.2.4 Diabatic coupling geometry

It is well documented that nonadiabatic transfer events are extremely sensitive to the landscape of the potentials involved as well as to the nonadiabatic coupling functions [105]. Influence of the dimensionality on nonadiabatic dynamics has been widely discussed [106–109]. In the context of conical intersections, the issue of the topology also includes a comparison of a true crossing case versus an avoided one, as well as the influence of the form of the diabatic coupling. Studies carried out with slightly anharmonic potentials show the same qualitative behavior [203].

In many calculations the inter-state coupling amplitude is chosen as a constant. A better choice is to localize it near the region of the conical intersection point according to Eq. (5.22). Fig. 5.9 shows a short-time evolution of the excited state

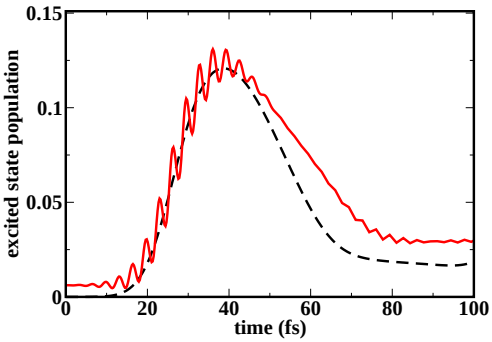

Figure 5.9: The population of the excited state for global ($V_d = \Lambda Q_c$, solid line) and local ($V_d = \Lambda Q_c\, \mathrm{e}^{-(Q_0-Q_{CI})^2/\sigma^2 - Q_c^2/\sigma^2}$, dashed line) diabatic couplings. Short time dynamics is shown in the presence of weak vibrational coupling ($\eta_0 = \eta_c = 0.01$, $\gamma^{-1} = 750$ fs).

population for the global diabatic coupling $V_d(\hat{\mathbf{Q}}_c) = \Lambda \hat{\mathbf{Q}}_c$ and the localized one [cf. Eq.(5.22)]. With the global coupling, the excited state is already populated before the excitation. Furthermore, the coupling immediately induces population transfer between the excited and the ground states. This is seen as fast oscillations with a frequency proportional to the electronic excitation energy 2Δ. As the diabatic coupling becomes more localized, one can observe a turnover effect [204]. First, the initial decay of the excited state population becomes more pronounced and then for very localized coupling the population is trapped in the excited state. This behavior is similar to the turnover effect as a function of the coupling constant Λ. The effect of the damping is less profound for the systems with a conical intersection compared with the one-dimensional nonadiabatic systems [95].

Next we compare the nonadiabatic dynamics of the 2D system, involving a conical intersection, and those of the 1D system with a local diabatic coupling. The parameters of the one-dimensional system are chosen to be the same as the tuning mode's geometry in the two-dimensional model ($\omega_0 = 0.074, \kappa_g = -0.0964, \kappa_e = 0.1194, \Delta = 0.4617$, all in eV). The diabatic coupling potential has a form of a damped Gaussian:

$$V_d(\hat{\mathbf{Q}}) = \Lambda\, \mathrm{e}^{-(\hat{\mathbf{Q}}-Q^*)^2/2\sigma^2}\ , \tag{5.25}$$

with Q^* being the position of the maximum coupling (referring to the point where the conical intersection occurs along the tuning mode in the 2D model). The same strength of the coupling ($\Lambda = 0.18$ eV) has been chosen for the both systems.

Fig. 5.10 displays the transient stimulated emission as a function of the time

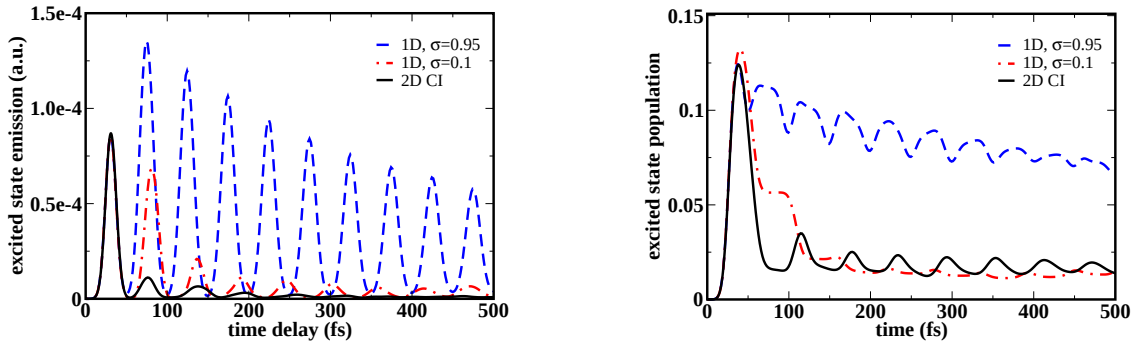

Figure 5.10: The nonadiabatic dissipative dynamics of a two dimensional system, involving a conical intersection (full lines) versus a one dimensional system with a local ($\sigma = 0.95$) nonadiabatic coupling (dashed lines). Dashed-dotted lines: a one dimensional system with more localized coupling ($\sigma = 0.1$). The transient stimulated-emission signal (left) and the population probability of the excited state (right) are shown. The strength of the diabatic coupling is $\Lambda = 0.18$ eV for all cases. The calculations are made for the system with weak vibrational relaxation ($\eta_0 = \eta_c = 0.01$) and medium electronic dephasing ($\bar{c}_e = 0.25$).

delay (left) and the time evolution of the diabatic population probability of the excited state (right) for two systems. The nonadiabatic dynamics are shown in the presence of dissipation (both vibrational relaxation and electronic dephasing are included). An initial fast decay of the excited state's population, typical for the system incorporating a conical intersection, does not occur in the one-dimensional system. There, the population, as well as the stimulated emission signal, exhibit much slower decay. The dynamics can be accelerated by further localizing of the diabatic coupling, but the turnover will eventually stop an additional increase in the decay rate.

Next we compare the nonadiabatic dynamics for the two-state two-mode system with different forms of the diabatic couplings. Fig. 5.11 shows the stimulated-emission signal (left) and the dynamics of the population probabilities (right) for three models. The dynamics of the system with a conical intersection (a true crossing) is compared to the system which involves an avoided surface crossing. In the avoided crossing model the diabatic coupling does not depend on the Q_c coordinate and is represented by a damped Gaussian according to Eq.(5.25). The third model has a symmetric diabatic coupling:

$$V_d(\hat{\mathbf{Q}}_0, \hat{\mathbf{Q}}_c) = \Lambda |\hat{\mathbf{Q}}_c| \, \mathrm{e}^{-(\hat{\mathbf{Q}}_0 - Q_{CI})^2/2\sigma^2} \, , \tag{5.26}$$

The dynamics of the population in the system with the avoided crossing are qualita-

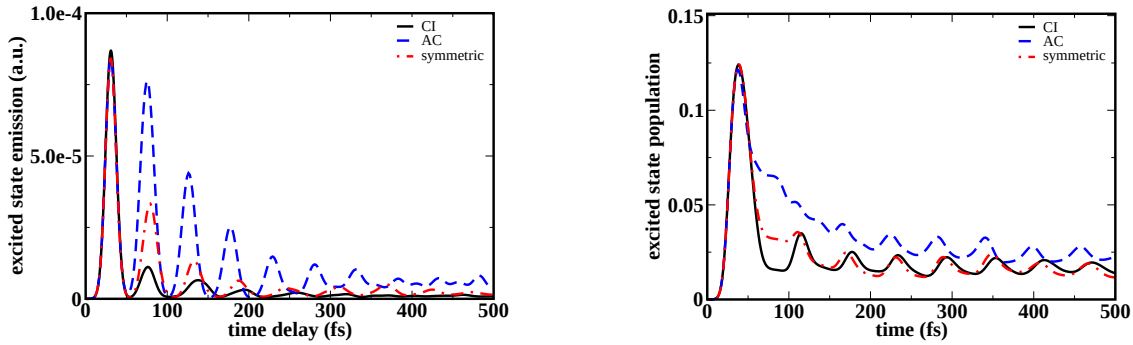

Figure 5.11: The nonadiabatic dissipative dynamics of a system with (a) a conical intersection (full lines), (b) an avoided crossing (dashed lines) and (c) a symmetric coupling (dashed-dotted lines). The transient stimulated-emission (left) and the population probability of the excited state (right) are shown for the system in presence of weak vibrational relaxation ($\eta_0 = \eta_c = 0.01$) and electronic dephasing ($\bar{c}_e = 0.25$). The strength of the diabatic coupling is $\Lambda = 0.18$eV for all cases.

tively similar to the dynamics in the one-dimensional model (Fig. 5.10). The decay is slower than in the crossing model. The oscillations of the stimulated-emission signal, indicating the coherent motion of the excited wave packet, persist for a quite long time (more than 500 fs). If the diabatic coupling is symmetric, the adiabatic surfaces exhibit a true crossing. The coupling, however, does not change a sign at the crossing point $(Q_{CI}, 0)$. In this case the stimulated-emission exhibits a fast decay, which is nevertheless slower than one for the system with a conical intersection. Only for the true conical intersection does the highly localized diabatic coupling cause the fastest initial decay of the observables associated with the excited state population.

5.3 Conclusions

The present study elucidates the dynamics of a system incorporating a conical intersection in the presence of a dissipative environment. The system was described by a model consisting of two vibronically coupled electronic states and two nuclear degrees of freedom. Dissipation is treated by using the Surrogate Hamiltonian approach and a reduced density operator dynamics based on the Lindblad formalism. The use of the Surrogate Hamiltonian has the advantage of a consistent treatment of initial correlations, non-Markovian dynamics and an explicit description of the pulse field. The latter is of a special importance, since our study is aimed at time-

dependent observables, which can be directly related to experiments.

Widely discussed adiabatic electronic state populations can only be partially connected to experimental pump-probe signals. Therefore the present study emphasizes the transient modulations of optical observables, which are a direct signature of the ultrafast dynamics, measured in the pump-probe experiments. The non-perturbative approach has been employed for describing the dynamics induced by the pump pulse, while the weak probe has been treated within a perturbative picture. This allows us to associate a quantum mechanical window operator to the absorption of the probe pulse centered at time t. The stimulated emission and absorption have been calculated as expectation values of this window operator.

The stimulated emission signals show a rapid initial decay on a time-scale of tens of femtoseconds, which can be associated with an ultrafast nonadiabatic transition via a conical intersection. This initial decay is almost unaffected by vibrational relaxation and the electronic dephasing. The dissipation becomes important in the following stage: it prevents a back transfer (re-crossing) leading to a sub-picosecond relaxation of the excited state population.

At the same time, it is clear that the pump/probe spectra are governed not only by the population dynamics, but also by the energy redistribution. After the initial curve crossing, the system may return close to its initial pre-pump configuration. Experimentally this is associated with the recovery of the bleach observed in the transient absorption signal. The *ground* state recovery dynamics, i.e. the bleach recovery and the cooling of the hot vibrational population, are not reflected in the electronic population probabilities. In our model the absorption signal shows coherent oscillations of the slightly perturbed ground state wave packet and apparently no fast recovery of the bleach up to 500 fsec. We can conclude that the energy relaxation, dominated by an intramolecular vibrational relaxation, proceeds much more slowly.

To summarize our findings, while the two-dimensional coupling scheme can mix states very rapidly, it cannot by itself (in the absence of ultrafast IVR or dephasing) lead to the fast bleach recovery. These observations have several implications: they suggest for example that the occurrences of 100 fs timescale bleach recovery in transition metal complexes in solution [167–169] might be better explained by simple

avoided crossings with strong outer sphere reorganization coupling terms than by invoking a conical intersection. They also suggest that conical mixing symmetry is not itself sufficient to generate a femtosecond bleach recovery or relaxation.

Chapter 6

Minimizing broadband excitation under dissipative conditions

Along with availability of ultrafast lasers, various techniques have been developed to design arbitrary shaped pulses. The pulse-shaping modulation has become an essential part of ongoing attempts to achieve a control of chemical reactions. The most studied feature of modulated pulses is frequency chirping, which describes the process of arranging the frequency components in a laser pulse with a certain phase ordering. Chirped pulses have been a subject of numerous experimental [205–214] and theoretical [110, 215–220] investigations. These studies have demonstrated that properly chirped broad-band pulses are superior to their transform-limited analogues in achieving a variety of dynamical goals.

Since the vast majority of the control experiments take place in condensed-phase environments, it is natural to ask to what extent the control of chemical processes is possible in the presence of the dissipation. Very often the only practical way to find an optimal control solution is to employ a feedback-loop optimization scheme [221–225] based on Genetic [226] or other evolutionary algorithms.

The subject of this Chapter is the interaction of an optimized chirped pulse with a molecule embedded in a solvent. The main objective of the simulations is to find an optimal field, which leads to minimal excitation without changing the frequency spectrum of the pulse. This control task is solved for the combined system, including the excited molecule immersed in a finite, but large environment. The latter may cause both vibrational and electronic dephasing, as well as vibrational relaxation -

processes, that have a time scale comparable to the pulse duration.

Employing the Surrogate Hamiltonian is advantageous due to a number of reasons. The method is based on a combined system-bath wavefunction, which enables a consistent treatment of initial correlations between the system and the bath. Moreover, an explicit treatment of a time-dependent field and its influence on the system-bath interactions are included. When the system coupled to the dissipative environment interacts with a strong electromagnetic field, the latter affects the system-bath coupling in an indirect way. Therefore it is particularly important to include the fields influence into the dynamics of the *combined* system. Finally, the Surrogate Hamiltonian enables the incorporation of a laser pulse of an arbitrary shape.

When an ultrashort pulse is transmitted through a solution containing a dye molecule, it is unavoidable that the photon energy will be partially converted into exciting the dye molecule. This excitation is enhanced if the frequency band of the pulse matches the absorption band of the molecule (cf Fig. 6.1). Can one minimize the excitation with the condition that there is no change in the frequency profile of the pulse and its energy? Considering the close relation between excitation and transmittance of the pulse such a control manipulation will also increase the transparency of the medium.

This problem has been addressed experimentally by Cerullo et al. [207] demonstrating that a negatively chirped pulse causes a minimum excitation. It was found that at low pulse fluence, the absorption and the fluorescence signal were independent of the chirp. However, as the fluence was increased, the fluorescence intensity exhibited a minimum at negative chirp, indicating that at this particular chirp the population transfer to the excited state was minimal. The optimal chirp for obtaining this minimum was found to be insensitive to variation of the pulse fluence in a broad range of fluencies.

Recently Nahmias et. al [227] have employed a closed-loop pulse shaping technique to search for better adopted pulse shapes, that will minimize the excitation. The main objective was to test whether nonlinear chirped pulses could reduce population transfer in a polyatomic chromophore in solution below levels attained by their linear chirped analogue. Moreover, dependence of the optimal solutions on the

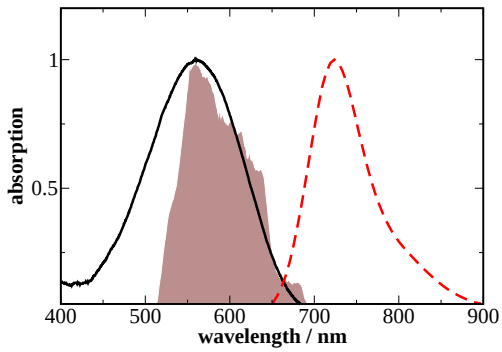

Figure 6.1: The pulse intensity spectrum along with absorption (solid line) and fluorescence (dashed line) spectra of LDS750 molecule in acetonitrile. Adapted from Ref. [227].

pulse fluence and on the nature of the solvent was investigated.

The present study is aimed at gaining insight on the interplay between the pulse parameters and the molecular response which lead to minimal excitation and maximal transmission. This task is carried by setting simulations which include light-matter interaction in an explicit fashion. Such a simulation allows to check the main control parameters in a well defined model.

The modeling of the process is based on a quantum description of the molecule and its environment using the Surrogate Hamiltonian method and on a semiclassical description of the radiation field.

The optimization scheme used in the present calculations employs a genetic algorithm [226], the global optimization method, proposed by Rabitz [221]. This is a closed-loop learning strategy that designs the optimal field to achieve a certain control task. Searching for the optimal solution, which leads to minimal transfer and maximal transmittance, dictates the condition of a constant frequency profile of the pulse. Therefore the optimization scheme should include varying the phases, rather than the pulse's amplitudes. The phases are used as input variables for the genetic algorithm. Different parameterization schemes are employed including expansion of the phase function in a Taylor series, as well as in a basis of periodic functions.

6.1 Theory

6.1.1 Model

The system under study describes a primary system immersed in a bath, while the external field is applied. The Hamiltonian of such a combined system is given by:

$$\hat{\mathbf{H}} = \hat{\mathbf{H}}_S \otimes \mathbb{1}_B + \mathbb{1}_S \otimes \hat{\mathbf{H}}_B + \hat{\mathbf{H}}_{SB} + \hat{\mathbf{H}}_{SF}(t) \ , \tag{6.1}$$

where $\hat{\mathbf{H}}_S$ is the Hamiltonian of the primary system, $\hat{\mathbf{H}}_B$ - the bath Hamiltonian and $\hat{\mathbf{H}}_{SB}$ describes the interaction between the system and the bath. The time-dependent interaction of the system with the electromagnetic field is represented by $\hat{\mathbf{H}}_{SF}(t)$.

We consider a molecular model with two electronic states and a single vibrational coordinate Q, coupled by an electromagnetic field. The system Hamiltonian is written as

$$\hat{\mathbf{H}}_S = \begin{pmatrix} \hat{\mathbf{H}}_g & -\mathsf{E}(t) \cdot \hat{\boldsymbol{\mu}}_{tr} \\ -\mathsf{E}^*(t) \cdot \hat{\boldsymbol{\mu}}_{tr} & \hat{\mathbf{H}}_e \end{pmatrix} \otimes \mathbb{1}_B \ , \tag{6.2}$$

with $\hat{\mathbf{H}}_{g/e} = \hat{\mathbf{T}} + V_{g/e}(\hat{\mathbf{Q}})$. $\hat{\mathbf{T}}$ is the kinetic energy operator, V_g and V_e are the potential energy operators on the ground and on the excited electronic states respectively. The coupling to the field is described in the dipole approximation with $\hat{\boldsymbol{\mu}}_{tr} = \hat{\boldsymbol{\mu}}_{tr}(\hat{\mathbf{Q}})$ being the electronic transition dipole operator. The electric field is given by

$$E(t) = \tfrac{1}{2} E_0(t)\, \mathsf{e}^{-i\omega_0 t} + \text{ c.c. } , \tag{6.3}$$

where $E_0(t)$ is a slowly varying envelope function and ω_0 is the carrier frequency. In the large wavelength limit, the spatial dependence of $E(t)$ is ignored.

The control objective is the total change in the population of the electronic state:

$$N_i(t) = \langle \Psi | \hat{\mathbf{P}}_i | \Psi \rangle \ , \tag{6.4}$$

where $\hat{\mathbf{P}}_i$ is the projection operator on either the ground or the excited electronic state and Ψ the total system-bath wavefunction. The flow of population from one electronic state to the other is given by the Heisenberg equation of motion [154,228]:

$$\frac{dN_g}{dt} = \frac{2}{\hbar}\, \mathsf{Im}[\langle \psi_e | \hat{\boldsymbol{\mu}} | \psi_g \rangle \cdot \mathsf{E}(t)] \tag{6.5}$$

which also can be written in the form

$$\frac{dN_g}{dt} = \frac{2}{\hbar}|\langle\psi_e|\hat{\boldsymbol{\mu}}|\psi_g\rangle||\,\mathsf{E}(t)|\,\mathsf{sin}(\phi_\mu + \phi_E) \tag{6.6}$$

where ϕ_μ and ϕ_E are the phase angle of the transition dipole moment and of the radiation field respectively. Without loosing generality ϕ_E can be set to zero because a constant phase of the field maps onto the phase of the transition dipole moment. Therefore, the direction of the population transfer is fully determined by the induced instantaneous phase of the transition dipole. In order to achieve, for example, the unidirectional population transfer from the ground to the excited state, the value of the relative phase angle is restricted to be negative [229].

6.1.2 Optimization scheme

The objective of the control is to reduce the population transfer from the ground electronic state to the excited state while maintaining the frequency spectrum of the pulse. This means that the control levers are the vector of phases of each frequency. The optimization strategy employs so-called closed-loop scheme [221,222] with Genetic algorithm [226].

The term "Genetic algorithm" describes a global optimization method based on several metaphors from biological evolution, commonly employed in coherent control [221, 224, 225]. The method generates a search in the space of solutions, guided by a set of rules. The operators of the genetic algorithm simulate selection, mutation and recombination processes [226]. The optimization procedure repeats those processes until the optimal solution is found.

The optimization scheme starts with a transform-limited pulse having a Gaussian envelope:

$$E(t) = E_0\ \mathsf{exp}\left[-\frac{(t-t_0)^2}{2\tau_p^2} - i\omega_0(t-t_0) - i\phi_E(t)\right] \tag{6.7}$$

where ω_0 and τ_p are the carrier frequency and the temporal width of the pulse respectively.

The pulse is then transformed to the frequency domain:

$$\mathcal{E}(\omega) = \mathcal{E}_0\ \mathsf{exp}\left[-\frac{(\omega-\omega_0)^2}{2\Gamma^2} - i\phi_\mathcal{E}(\omega)\right] \tag{6.8}$$

and parameterized by changing its phases $\phi_\mathcal{E}(\omega)$. One way is to add random phases at each point of the discrete spectrum. These random phases are considered as an

input for the genetic algorithm. This procedure, however, increases the pulse width in the time-domain significantly. The alternatives include either an expansion of the phase in a polynomial form $\sum_{k=1}^{N} c_k(\omega - \omega_0)^k$ or on the basis of the periodic functions [230]. In the first case each set of the polynomial coefficients represents a gene for the genetic algorithm. Considering the lowest order terms in the phase expansion (linear and quadratic), the pulse with linear chirp in the time domain is given by:

$$\mathcal{E}(\omega) = \mathcal{E}_0 \ \exp\left[-\frac{(\omega-\omega_0)^2}{2\Gamma^2} - i\chi'\frac{(\omega-\omega_0)^2}{2}\right] \tag{6.9}$$

The chirp rate term χ' causes a phase shift of each spectral component of the field proportional to its 'distance' from the carrier frequency. Thus a negatively chirped pulse the central frequency decreasing with time, and a positively chirped pulse the central frequency increases with time.

In the case of a periodic function, the phase is expanded as

$$\phi(\omega) = \sum_{k=1}^{K} c_k \ \cos(k(\omega-\omega_0)\tau_m + \theta_k) \ , \tag{6.10}$$

and the input for the genetic algorithm consists of the expansion coefficients c_k, θ_k. The periodic phase mask adds higher harmonics to the spectral phase function and splits the single pulse into train of sub-pulses in the time domain. The total duration of the optimized pulse is determined by the order of expansion and τ_m.

The new pulse is Fourier-transformed back to the time domain and introduced into the Schrödinger equation of the total system. Then the excited state population at the end of the pulse, defined as a *fitness*, is calculated.

The Genetic algorithm is implemented in the following way: the initial set of $N = 10$ candidate solutions is generated randomly using a uniform random number generator. Each set (a gene) consists of the phases expansion coefficients and represent a possible solution for the optimal pulse. Once the initial generation is formed, the fitness values of the different candidates solutions is calculated. At the next step the real number adaptive genetic algorithm (RAGA) operators are applied to construct a new generation.

The following RAGA operators [224, 231] were used in the simulations:
(1) (O_{best}): copy the $k_{best} = 2$ highest fitness candidate solutions to the new generation.

(2) (O_{rand}): formation of $k_{rand} = 2$ random candidates.
The range of formation of random candidates (noise) can be adjusted iteratively, depending on the fitness average.
(3) (O_{cros2}): two point cross-link between two parents to form two children.
(4) (O_{crosn}): n-point cross-link between two parents to form two children. The rearrangement was accomplished by the following steps: a random number η was chosen from a uniform distribution in the range of [0,1]. If $\eta \geq 0.5$, the element of parent 1 was copied to child 2 and the corresponding element from parent 2 to child 2, while if $\eta < 0.5$, the order was switched.

The procedure is repeated until the convergence criteria is fulfilled.

6.2 Results and Discussion

Let us consider two harmonic potential energy surfaces S_0 and S_1 of equal frequency. Following Cerullo et al. [207] a highly displaced low-frequency harmonic mode (ω_0 = 170 cm^{-1} and Δ = 2.9 in dimensionless coordinates) is chosen. The vertical excitation energy E_0 is $16.1 \cdot 10^{-3}$ cm^{-1}. This model was purported to schematically represent the effects the combination of both underdamped (intramolecular) and overdamped (intermolecular) motions.

The duration of the transform-limited pulses was chosen to t_{p_0}=10 fs for all calculations and the intensity was within the experimental data [227]. The central frequency was slightly red-shifted according to the resonance.

The influence of the bath on the primary system is characterized by the spectral density function $J(\omega)$. For an Ohmic bath the damping rate is frequency-independent. The spectral density in the continuum limit is given by

$$J(\omega) = \eta \ \omega \ \ \mathsf{e}^{-\omega/\omega_{cut}} \tag{6.11}$$

for all frequencies ω up to the cutoff frequency ω_{cut}. The coupling strength η is given by the ratio of the damping rate γ and the vibrational frequency ω_0. A finite bath with equally spaced sampling of the energy range is used in all calculations. The cutoff frequency is set to $2.5\omega_0$, which defines the shortest time scale of the bath (about τ_{bath} = 80 fs). The time scale corresponding to the frequency spacing $\Delta\omega$ defines the Poincaré period (τ_{rec}). It should be larger than any other time scale of

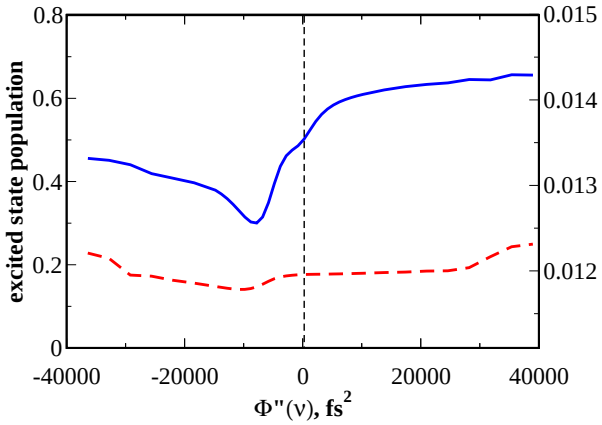

Figure 6.2: Excited state population as a function of the linear chirp for the isolated system ($\eta = 0$). The population is shown at the end of the pulse for the high (solid line) and the low (dashed line) fluences. The duration of the corresponding transform-limited pulse is t_{p_0}= 10 fs. Note the different scale for the excited population for two energy regimes.

interest. With ω_{cut} fixed, this time becomes:

$$\tau_{rec} = \frac{2\pi}{\Delta\omega} = \frac{2\pi N}{\omega_{cut}} \ . \tag{6.12}$$

Thus, with an increasing number of bath modes, the convergence progresses in time. In the present modeling the number of TLS has been chosen to be $N = 15 - 20$ (for different coupling strengths). This ensures that τ_{rec} is greater than the overall simulation time. The temperature of the bath has been chosen to be zero.

6.2.1 Linear chirped pulse

Isolated system

We start the study with a system without dissipation, subject to a chirped electromagnetic field of the following form [232]:

$$E(t) = E_0 \ \exp\left[-\frac{(t-t_0)^2}{2\tau_p^2} + i\frac{\chi}{2}(t-t_0)^2 + i\omega_0 t\right] \ , \tag{6.13}$$

where ω_0 is the transform-limited carrier frequency of the field and χ is the chirped rate in the time representation . The pulse duration τ_p and the chirp rate χ are defined as:

$$\tau_p^2 = {\tau_{p_0}}^2 + [2\Phi''(\omega_0)/\tau_{p_0}]^2 \ , \tag{6.14}$$

$$\chi = -4\Phi''(\omega_0)\{\tau_{p_0}^4 + 4\Phi''(\omega_0)^2\}^{-1} \ , \tag{6.15}$$

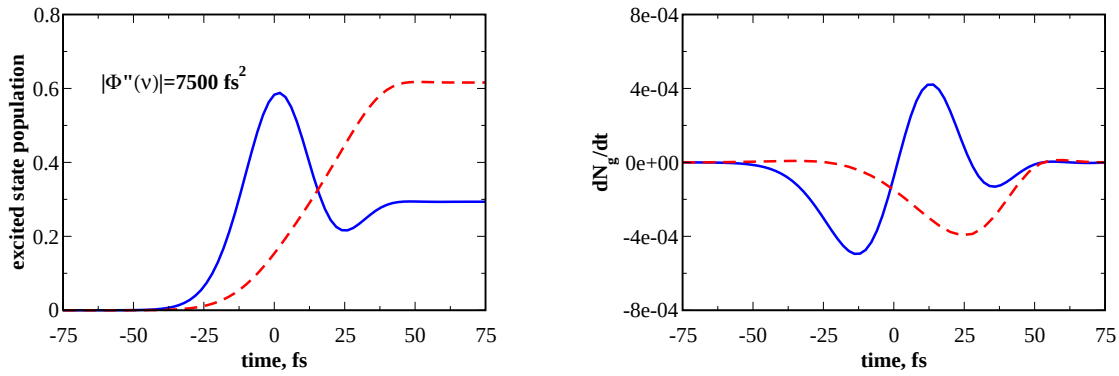

Figure 6.3: (Left) Time evolution of the excited state population $N_e(t)$ of the isolated system ($\eta = 0$) for the high energy excitation. The population is calculated for a negatively ($\Phi''(\nu) = -7500$ fs^2, solid line) and a positively ($\Phi''(\nu) = 7500$ fs^2, dashed line) chirped pulses. (Right) The imaginary part of the transition dipole moment multiplied by the field amplitude.

where $\Phi''(\nu) = 4\pi^2\Phi''(\omega)$ is a linear chirp parameter and $\Delta t_{FWHM} = 2\tau_{p_0}\sqrt{\ln 2}$ is the full width half maximum of the temporal intensity profile of the corresponding transform-limited pulse.

Fig. 6.2 shows the excited state population at the end of the pulse as a function of the linear chirp parameter $\Phi''(\nu)$ in two energy limits. In the high-energy limit Fig. 6.2 shows a minimum at a negative chirp (about $\Phi''(\nu)$ = -7500 fs^2) indicating that at this particular chirp the population transfer to the excited state is minimal. Thus at low intensity the chirp hardly affects the population transfer. However, the minimum is slightly shifted to a larger negative value of the chirp.

Fig. 6.3 shows the time evolution of the excited state population $N_e(t)$ and the time derivative $\frac{dN_g}{dt}$ (calculated independently as an imaginary part of the transition dipole moment multiplied by the field according to Eq. 6.6) for pulses with a chirp parameter $\Phi''(\nu) = \pm 7500$ fs^2. For a high-intensity field the dynamics caused by a negatively chirped pulse differs from those induced by a positive one. For both pulses, the phase first gains a negative value and the population is transferred from the ground state to the excited one. However, for a negatively chirped pulse, the phase changes its sign (twice) during the dynamics and the pulse also dumps some population back to the ground state.

Positively chirped pulses lead to a monotonic population transfer. With sufficient intensity, this may cause a population inversion [207, 211, 229, 232]. The coupling window, given by an instantaneous frequency of the chirped pulse moves from lower

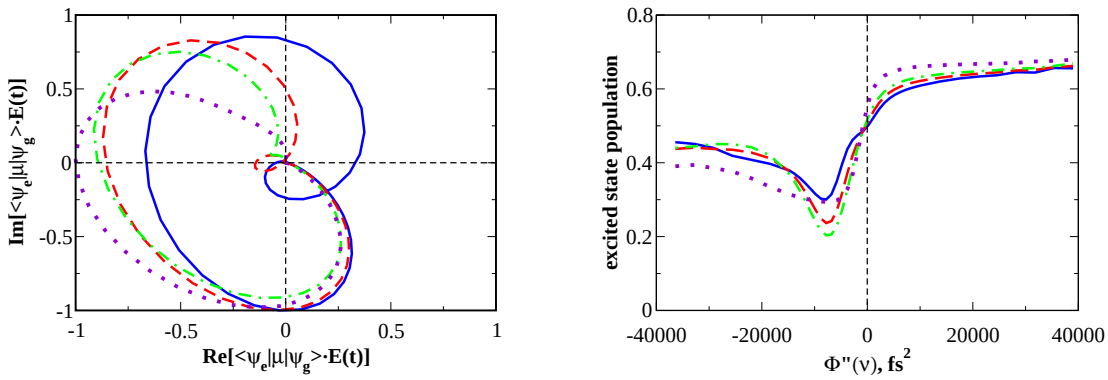

Figure 6.4: (Left) Trajectories of the transition dipole moment, renormalized by its maximal amplitude, for excitation by the linear negatively chirped pulse ($\Phi''(\nu) = -7500$ fs^2). (Right) Excited state population at the end of the pulse as a function of the linear chirp parameter $\Phi''(\nu)$. The calculations are performed for the system without dissipation (solid line) and for the system with vibrational relaxation with weak ($\gamma^{-1} = 1000$ fs, dashed line), medium ($\gamma^{-1} = 500$ fs, dashed-dotted line) and strong ($\gamma^{-1} = 125$ fs, dotted line) system-bath couplings.

to higher frequencies. The excited wavepacket, however, moves down due to the potential gradient of the excited state. Thus the evolution of the imaginary part of the transition dipole is restricted to negative values with pure absorption dominating.

For negatively chirped pulses, the coupling window follows the motion of the excited wavepacket, which gains an extra phase. These dynamics induce the relative phase shift, that may modify the total relative phase relation between the ground and excited state wavefunctions [229]. The imaginary part of the transition dipole moment is not restricted to negative values anymore and the pulse induces both absorption and stimulated emission.

Dissipative system

The top panel of Fig. 6.4 displays the transition dipole trajectories during the excitation process for the dissipative system with vibrational relaxation and dephasing. The calculations are performed for the negatively chirped pulse with an optimal linear chirp parameter $\Phi''(\nu) \approx$ -7500 fs^2 (the pulse, which leads to the minimum population transfer). The trajectory corresponding to a system without dissipation lies in both the negative and the positive imaginary quadrants. As mentioned above, when the phase gains negative values the population is transfered from the ground state to the excited one and vise versa. The addition of vibrational relaxation slows

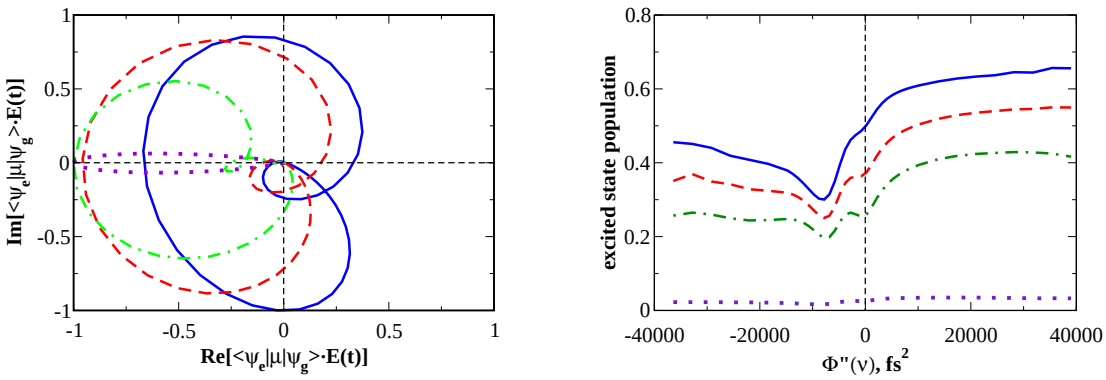

Figure 6.5: (Left) Trajectories of the transition dipole moment, renormalized by its maximal amplitude, for excitation by the linear negatively chirped pulse ($\Phi''(\nu) = -7500$ fs^2). (Right) Excited state population at the end of the pulse as a function of the linear chirp parameter $\Phi''(\nu)$. The calculations are performed for the isolated system (solid line) and for the system with pure electronic dephasing: weak ($\gamma_{ed}^{-1} = 250$ fs, dashed line), medium ($\gamma_{ed}^{-1} = 125$ fs, dashed-dotted line) and strong ($\gamma_{ed}^{-1} = 20$ fs, dotted line) couplings.

down the dynamics and decreases the value of the relative phase angle. As a result less population is transferred to the excited state, when the phase is negative (absorption).

The bottom panel of Fig. 6.4 shows the excited state population at the end of the pulse as a function of the linear chirp parameter $\Phi''(\nu)$. Including vibrational relaxation leads to a shift of the minimum toward smaller negative chirps, while for large negative chirps the population becomes constant. The latter is consistent with the experimental results for the LD690 dye in a solution, obtained by Cerullo et al. [207]. For very long negatively chirped pulses, the time scale of the excited state dynamics becomes significantly longer relative to the pulse duration. Thus the red tail of the pulse misses the excited population and does not contribute to the stimulated emission. Since the vibrational relaxation leads to an additional delay of the excited state wavepacket, the population becomes constant for shorter pulses. Delay in the dynamics due to the vibrational relaxation may lead to enhancement in the population transfer, if the excitation pulse is positively chirped [233]. The effect of vibrational relaxation may be more involved. For high-fluence pulses a significant hole is created in the ground state distribution, initiating the ground state dynamics. Vibrational relaxation on the ground state will dump these dynamics, which may influence indirectly the population transfer.

Next the influence of a pure electronic dephasing on the population transfer is considered. Electronic dephasing has the fastest time scale of dissipative processes in a condensed phase environment. Coherent superposition of the ground and excited electronic states, created by the pulse, will be affected by the electronic dephasing if its time scale is similar to the pulse duration. Fig. 6.5 shows (right) the excited state population at the end of the pulse as a function of the chirp parameter, and (left) the trajectories of the transition dipole moment in the presence of the pure electronic dephasing. The main effect of dephasing is the destruction of the phase coherence between the excited and the ground state wavefunctions. If the dephasing rate ($\gamma_{ed}^{-1} = 250$ fs) is longer than the pulse duration, the change in the population transfer is minor. The effect, however, is more profound for longer pulses (both negatively and positively chirped). Medium and strong electronic dephasing reduces significantly the amount of population transfered to the excited state. While the trajectories of the transition dipole moment for the optimal pulse decreases as the dephasing becomes stronger, the character of the dynamics remains the same. The trajectories lie in both negative and positive quadrants, meaning that the pulse initiates absorption, followed by stimulated emission. The optimal chirp rate seems to be insensitive to the electronic dephasing.

6.2.2 Nonlinear chirped pulses

Isolated system

The performance of the linearly optimal chirped pulses can be compared to unrestricted optimal pulses such as a pulse with a different phase at each point of the discrete frequency spectrum. Such an optimal pulse is displayed in Fig. 6.6. The evolution of the excited state population is shown for the linearly chirped and for the optimized pulses. The total duration of the pulse is four times longer than the experimental data of Ref. [227]. The optimization algorithm chooses the optimal pulse with the best distribution of energy, which eventually dumps all population back to the ground state. This pulse is not unique and may have a complex structure (the inset figure in Fig. 6.6). The question of obtaining such pulses depends on the abilities of particular pulse shapers. However, since there is always experimental

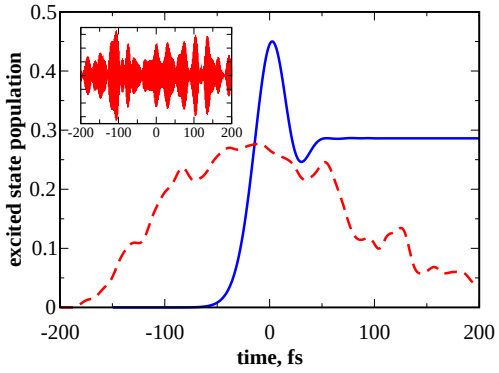

Figure 6.6: Time evolution of the excited state population $N_e(t)$ of the isolated system for the high-energy excitation. The population is calculated for a linear negatively chirped pulse (solid line), and for the optimal pulse (dashed line), obtained by using a genetic algorithm with the random phases, generated at discrete points of the frequency spectrum. The inset figure shows the temporal profile of the optimized pulse.

restrictions of phase modulation and as a result the pulse duration is confined, only pulses with duration limited to the experimental data are studied [227].

To obtain optimized pulses with a limited time duration, the frequency-dependent phase was expanded either in Taylor series (up to the second order) to obtain the linearly chirped pulse or in the basis of periodic functions (up to 4th-5th order). The expansion coefficients were introduced as input genes in the genetic algorithm. The procedure reduces significantly the size of the search space in comparison to the free parameterization (multiplying by random phase at each of the frequency spectrum components) and therefore results in faster convergence.

The minimization of the excited state population at the end of the pulse converges after approximately 30-40 generations to a value that is 40% lower than the population transfered by the initial randomly generated pulse (the first generation). The optimal pulse performs better than the linearly chirped pulse, transferring 30% less of the population to the excited state at the end of the pulse (see Fig. 6.8, left panel).

Fig. 6.7 shows the Wigner time-frequency representation of the linear negatively chirped pulse (left panel) and an example of an optimized nonlinearly chirped pulse (right panel). Note that the latter shows negative amplitude indicating a phase structure between the two large subpulses. The first one (approximately $t < 0$) shows mainly negative quadratic phase behavior (a linear chirp in the time domain).

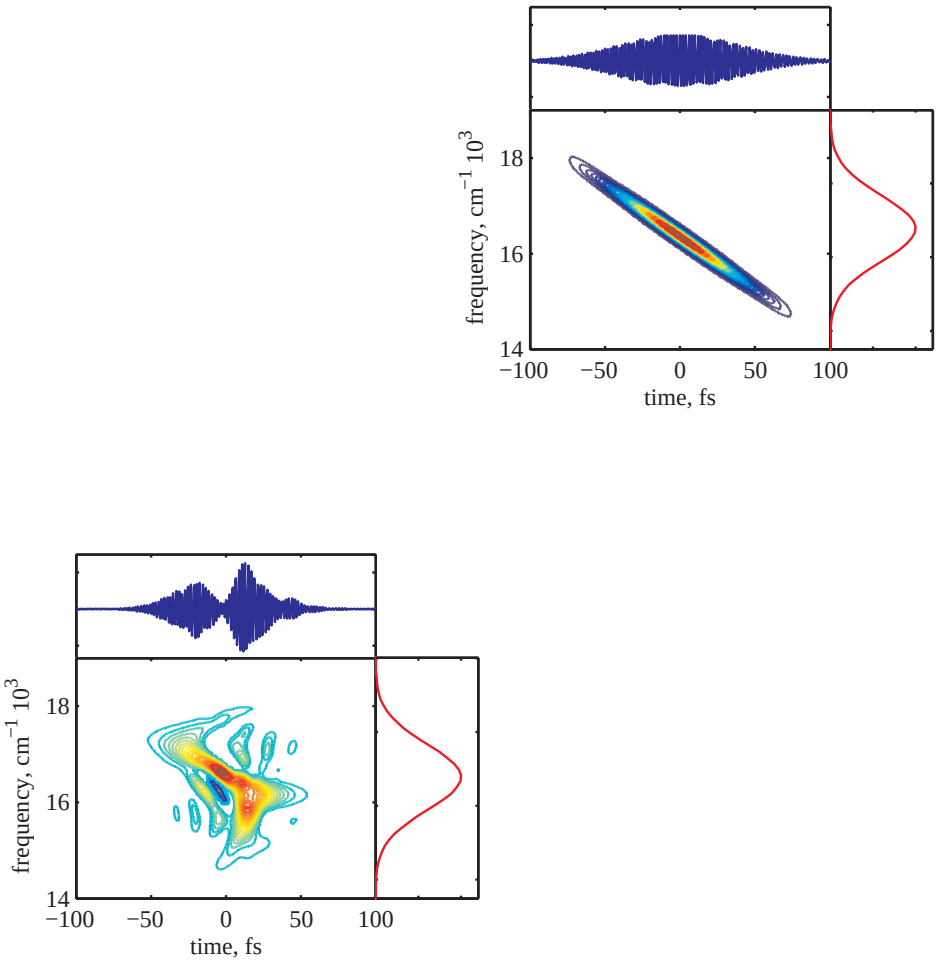

Figure 6.7: Calculations for non-dissipative system. Time-frequency Wigner distribution corresponding to the optimized linear (left) and nonlinear (right) chirped pulses. The right sides show the frequency spectra of the pulses, while their temporal profiles are shown in the upper panels. The phase is expanded in the Taylor series up to the second order (linear chirp) and in the basis of periodic functions (nonlinear chirp).

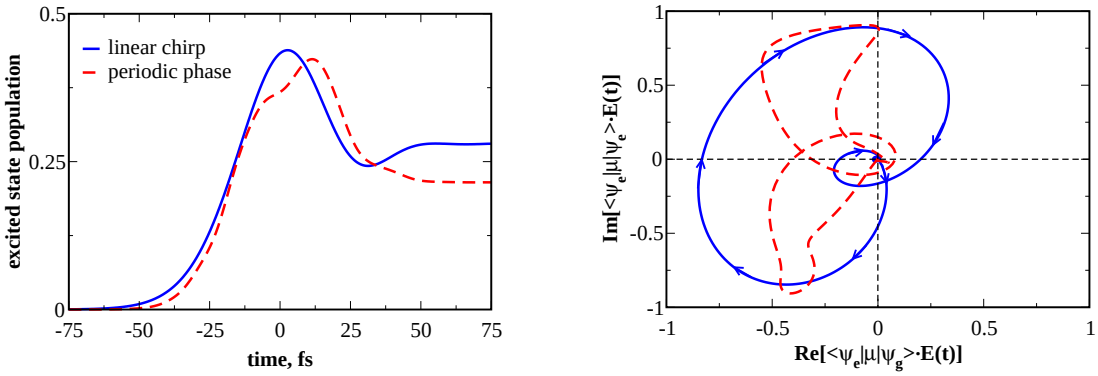

Figure 6.8: (Left) Evolution of the excited state population $N_e(t)$ of the isolated system for the high-energy excitation. The population is calculated for a linear negatively chirped pulse (solid line), and for the optimal pulse (dashed line), obtained by using a genetic algorithm with the phase expanded in the basis of periodic functions. (Right) Trajectories of the transition dipole moment, renormalized by its maximal amplitude. Solid and dashed lines refer to the linear chirped pulse and its nonlinear analogue respectively.

Consisting of the "blue" portion of the spectrum, this part of the total pulse leads to absorption. The second subpulse is highly nonlinear (while shows very small positive chirp) and causes mainly stimulated emission.

Evolution of the transition dipole moment sheds some light on the pulse's behavior. The left panel of Fig. 6.8 displays the transition dipole trajectories during the excitation process. Besides the small overlap, the phase of the first subpulse gains mostly negative value and as a result the population is transfered from the ground state to the excited one. The phase of the second subpulse is primarily in the positive quadrants and the pulse's chief contribution is stimulated emission.

The nonlinear feature of the optimal pulse supports the idea that the pulse follows the dynamics of the excited state wavepacket. The red edge of the pulse arrives earlier than in the case of the linearly chirped pulse, since the wavepacket has already reached the minimum of the excited state potential. The total duration of the optimal pulse is shorter than its linear analogue.

We have shown that without time restriction, it is easy to obtain shaped pulses, which lead to zero fluorescence. Optimal pulses with time duration confined to the experimental data (not longer than 100 fs) may actually be shorter than linearly chirped pulses and still perform better (transferring 30 % less of the population).

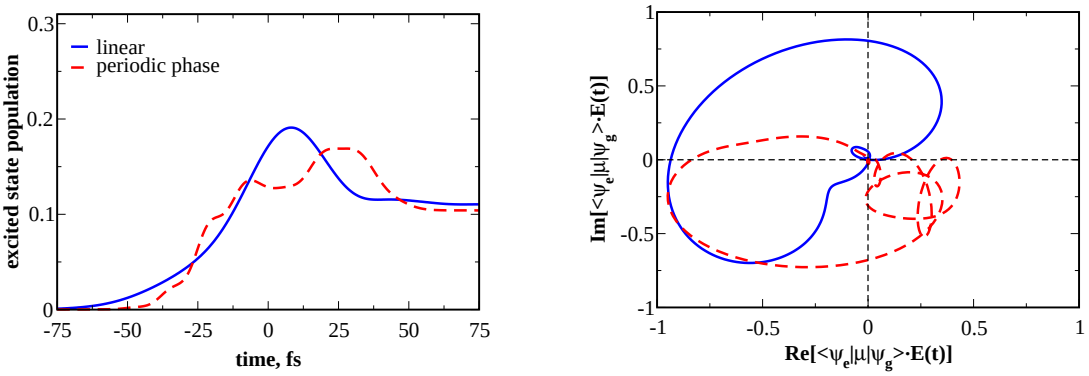

Figure 6.9: (Left) Time evolution of the excited state population $N_e(t)$ of the dissipative system for the high-energy excitation. The population is calculated for a linear negatively chirped pulse (solid line) and for the optimal pulse, obtained by using a genetic algorithm (dashed line). (Right) Trajectories of the transition dipole moment, renormalized by its maximal amplitude. Calculations were performed for the system with with weak vibrational relaxation ($\gamma^{-1} = 500$ fs) and medium pure electronic dephasing ($\gamma_{ed}^{-1} \approx 150$ fs).

Dissipative system

The effect of dissipation on the optimal pulses is next considered. Electronic dephasing, as shown previously for the linearly chirped pulses, reduces the population in the excited state at the end of the pulse, simply by destroying the transition dipole. The effect of the vibrational relaxation is minor, at the time scales typical for a molecule in solution.

Fig. 6.9 shows the evolution of the excited state population (left panel) and the transition dipole trajectories during the excitation process (right panel) for a system with medium vibrational relaxation ($\gamma_{vr}^{-1} = 500$ fs) and medium electronic dephasing ($\gamma_{ed}^{-1} \approx 150$ fs). Results for the linearly chirped pulse were compared with those of the optimal pulse. Surprisingly, the nonlinear pulse leads to almost the same result as its linearly chirped analogue. The difference in the population at the end of the pulse is less that 4% (while for the nondissipative system it is approximately 30 %) The total population transfered to the excited state is significantly lower (approximately 50 %), as a result of including electronic dephasing. The trajectories of the transition dipole moment (Fig. 6.9, right) lie in both negative and positive quadrants, meaning that the pulses lead to both absorption and stimulated emission, but the value of the relative phase decreases as the dephasing becomes stronger.

Fig. 6.10 shows the Wigner time-frequency representation of the linear negatively

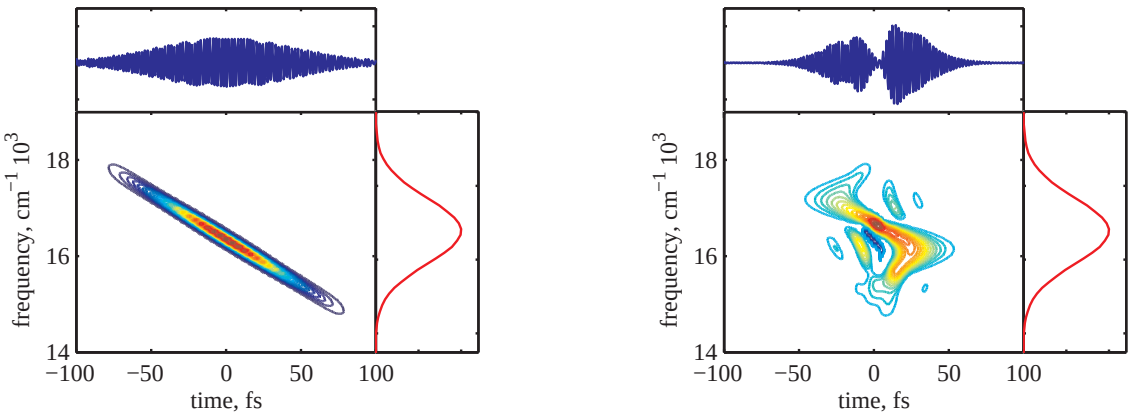

Figure 6.10: Calculations for the dissipative system. Time-frequency Wigner distribution corresponding to the optimal linear (left) and nonlinear (right) chirped pulses. Calculations were performed for the system with medium vibrational relaxation (γ^{-1} = 500 fs) and electronic dephasing ($\gamma_{ed}^{-1} \approx 150$ fs).

chirped pulse (left panel) and the optimized nonlinearly chirped pulse (right panel). The shape of the optimized pulse is similar to the one obtained for the non-dissipative system. While it consists of few subpulses, there is a part with noticeable negative chirp and a part, which shows a profound positive chirp. The appearance of the positively chirped part can be associated with the backward movement of the excited state wavepacket.

Does the specific form of the optimized pulse depend on the parameters of the primary system? Fig. 6.11 shows the Wigner distribution of the optimized pulse for the primary system with a different set of parameters. The calculations are performed for the high-frequency vibrational mode of 1662 cm^{-1} with dimensionless displacement of D=0.35. These parameters refer to one of the vibrational modes of LD690 [208, 234]. Since the excited state period is about 20 fs, we choose an artificially short time scale of the vibrational relaxation and pure electronic dephasing. The obtained optimized pulse consists of a train of subpulses, which follow the dynamics of the excited wavepacket. Since the oscillation period is much shorter than the one for the low-frequency mode, the phase of the transition dipole moment changes its sign a few times according to the position of the excited state wavepacket. The result is a more complex interplay between absorption and stimulated emission. The optimal pulse can not be defined anymore as a “pure” negatively chirped one.

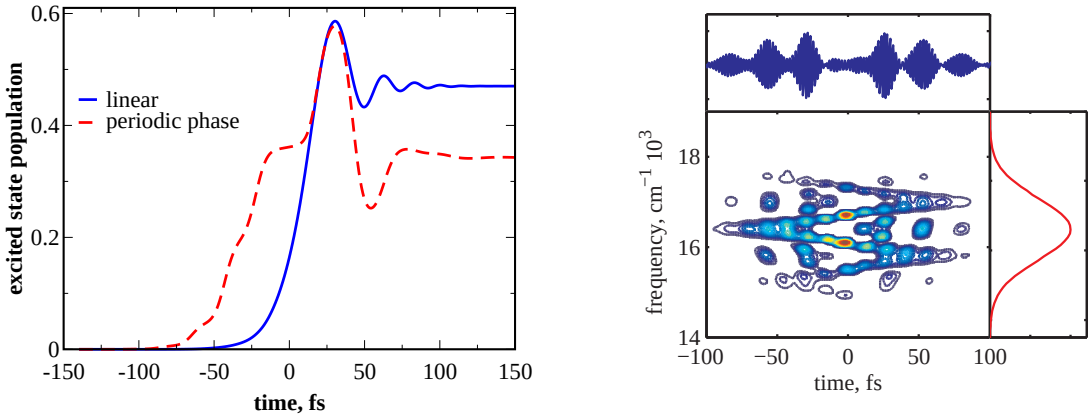

Figure 6.11: (Left) Time evolution of the excited state population $N_e(t)$ of the dissipative system for the high-energy excitation. The population is calculated for a linear negatively chirped pulse (solid line) and for the optimal pulse, obtained by using a genetic algorithm (dashed line). (Right) Time-frequency Wigner distribution corresponding to the optimized nonlinear chirped pulse. The calculation are performed for the primary system with the following parameters: the ground and the excited state frequencies ω=1662 cm^{-1} and the dimensionless displacement of D=0.35. The right sides show the frequency spectra of the pulses, while their temporal profiles are shown in the upper panels. The phase is expanded in the basis of periodic functions.

Compiling the presented results one can not find direct semiclassical analogy between the dynamics on the excited state and the chirp rate as mentioned in Ref. [235]. This point will be investigated in the future studies.

6.2.3 Role of intensity

Cerullo et al. [207] have reported that the optimal linear chirp for fluorescence minimization was insensitive to the pulse intensity. The experimental study of Nahmias et al. [227] seems to confirm these findings. The calculations for a non-dissipative system show strong dependence of the population transfer on the pulse intensity. The value of the optimal linear chirp as a function of fluence is shown in Fig. 6.12. The fluence range lies within the experimental data reported in Ref. [227].

The position of the optimal linear chirp is shifted to smaller values as the fluence increases. Vibrational relaxation hardly affects this tendency, while electronic dephasing reduces this dependence.

The left panel of Fig. 6.13 shows the excited state population at the end of

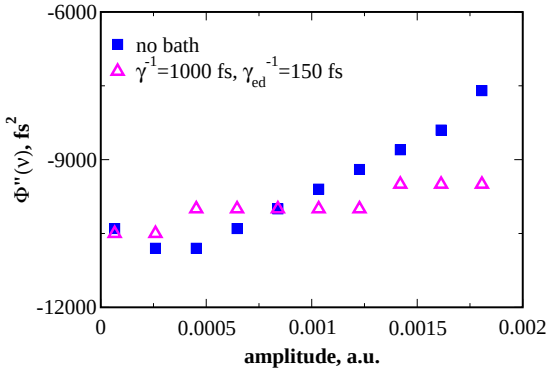

Figure 6.12: Effect of the intensity for linearly chirped pulses. The value of the linear chirp is plotted as a function of the pulse fluence (the amplitude of the corresponding transform-limited pulse. Calculations were performed for the isolated system (squares) and as well as for a dissipative system (triangles) with with medium vibrational relaxation ($\gamma^{-1} = 500$ fs) and medium pure electronic dephasing ($\gamma_{ed}^{-1} \approx 150$ fs).

the pulse as a function of the pulse intensity (the amplitude of the corresponding transform-limited pulse) for non-dissipative system. The results for the linearly chirped pulses (triangles) are compared to those obtained for the optimized nonlinear pulse (squares). The intensity of the pulse runs over the range with a maximum factor of two higher than in the experiment of Nahmias et al. [227]. We can determine at least three regions in the whole range of intensities. At a low-fluence region, the population at the end of the pulse depends linearly on the pulse intensity. The difference between the linearly chirped and optimal nonlinear pulses is minor. The additional region is at very high intensities. Here both kind of pulses become very close to transform-limited 2π-pulse, which can "dump" all population back to the ground state. The nonlinear pulses perform better at this region. The assumption of a one-photon process is probably incorrect for the high-intensity region and for real physical systems.

The intermediate-region (centered about the intensity, referred to the transform-limited π-pulse) shows a very distinct behavior for two kinds of pulses. The optimal nonlinearly chirped pulses lead to noticeably better results, transferring between 20% to 70 % less population, than linearly chirped pulses. The right panel of Fig. 6.13 displays results for the system with weak vibrational dephasing and medium electronic dephasing. Dissipation affects the above dependence in the following way: first, the electronic dephasing reduces the amount of population, that eventually

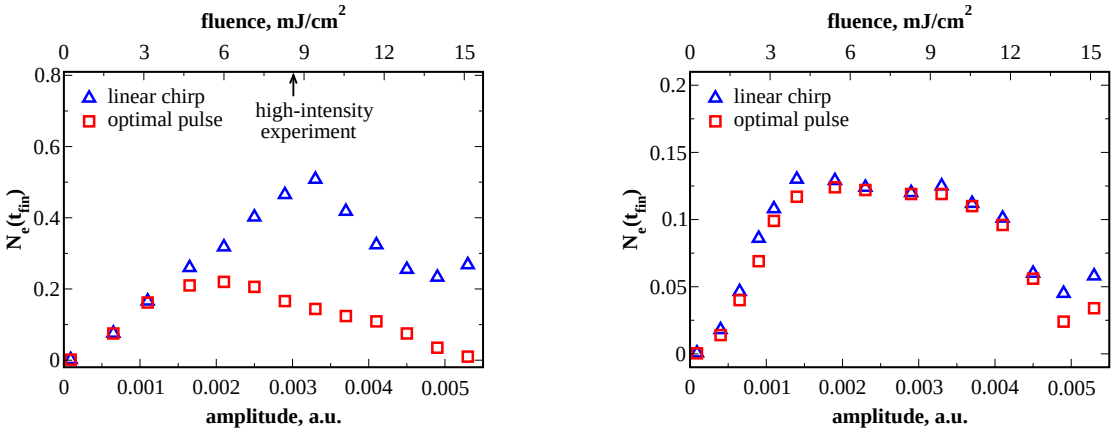

Figure 6.13: The excited state population at the end of the pulse as function of the pulse fluence (the amplitude of the corresponding transform-limited pulse). Calculations were performed (left panel) for the system without dissipation and (right panel) for the system with medium vibrational relaxation ($\gamma^{-1} = 500$ fs) and medium pure electronic dephasing ($\gamma_{ed}^{-1} \approx 150$ fs). The arrow points to the maximal fluence used in the experiment by Nahmias et al. [227].

transfered to the excited state. The effect is however less profound for the very high intensity region, since the optimal pulses in this region (both linearly and nonlinearly chirped) are shorter than the time scale of the electronic dephasing. Secondly, it blurs the difference between linearly chirped and nonlinear optimized pulses, since the former are affected to the larger extent.

6.3 Conclusions

The present study simulates an ultrafast light-induced process under dissipative conditions. Defining the optimal pulse, which leads to *minimal* fluorescence without change in the frequency profile, was considered to be the optimal task. This task is equivalent to preserving the number of photons transmitted through the medium with allowance for shifting the photon frequency from blue to red. Can one obtain a well-defined optimal solution for such a system with dissipation, especially if the pulse duration exceeds the time scale of relaxation processes? To what extent does the optimal pulse perform better than its linearly chirped analogue?

The dynamics of the primary system were modeled as a single, highly-displaced low-frequency mode. This particular choice is used to represent schematically the effect of both intramolecular and intermolecular coordinates on the rapid dynamic

Stokes shift of the dye emission. Dissipation was treated by using the Surrogate Hamiltonian approach, which has an advantage of a consistent treatment of initial correlations, non-Markovian dynamics, and an explicit description of the pulse field.

Using the learning feedback control we were able to obtain pulse shapes leading to a minimum fluorescence with maximal transmittance. These pulses have a complex structure and are extended to long durations. It is possible however to determine optimal pulses with restricted time duration, which are still preferable relative to linearly chirped ones. These pulses usually consist of a large negatively chirped part and an additional nonlinear subpulse. In the high-intensity region nonlinear pulses suppresses the population transfer to the excited state more efficiently than their linearly chirped analogue. The amount of population transferred to the excited state at the end of the pulse is 30-70% lower for the linearly chirped pulses.

Vibrational relaxation has a minor effect on the optimal solutions. For linearly chirped pulses it shifted the optimal chirp parameter to slightly smaller values due to dephasing of the excited wavepacket. The electronic dephasing, on the other hand, may reduce the amount of the population transferred to the excited state significantly, especially if its time scale is comparable with the duration of the pulse. The influence of the electronic dephasing on the form of the optimal pulse was however insignificant. This confirms the experimental findings of Nahmias et al. [227] of the negligible solvent effect on the optimal pulse shapes.

Contrary to the experiment, we found a significant effect of the pulse fluence. While at low-intensity , the difference between the linearly chirped and the optimized nonlinearly chirped pulses is hardly noticeable, the situation changes at high-intensity limit. The optimal pulses perform better than the linearly chirped pulses. Including electronic dephasing may reduce this difference, affecting the linearly chirped pulses (which have longer duration). At very high intensities, both pulses become similar to the transform-limited 2π pulses. In agreement with experiment, changing the pulse fluence in the range of experimental data, has a negligible effect on the form of the optimal pulse.

When comparing the current simulations with experiments, the effect of nonuniform intensity should be considered. The molecules in solution have a random orientation leading to a $\cos^2$ distribution. In addition the high intensity is the result

of tight focusing which adds a Gaussian spatial intensity distribution. Finally we have also ignored the propagation effect in the medium which can alter the pulse shape and intensity. The present model is restricted to two electronic states and one primary vibrational mode. If an additional electronic excited state is positioned for excited state absorption the present optimal solutions will be modified to avoid such a state. For these reasons a comparison with experiment is only qualitative. It is aimed to clarify the main effects of chirp and intensity on population transfer in a two state model.

Chapter 7

Epilogue

The vast majority of chemical processes occur in condensed-phase environments. Therefore the development of theoretical tools, able to describe quantum many-body systems from first principles, is essential. The chief obstacle facing dynamical simulations of extended systems is the exponential scaling of the computational effort with the number of degrees of freedom. Despite the growing number of theoretical methods, no comprehensive solution to this scaling problem has been achieved. Most of the existing theoretical methods fail to provide a consistent treatment of all aspects of a quantum system interacting with a dissipative environment.

The Surrogate Hamiltonian method, which is the basis of the presented work, has been developed for simulating quantum transient phenomena taking place in a condensed-phase environment. The numerical and physical properties of the method make it advantageous for treating a wide range of dissipative processes. While the method is formally based on the idea of system-bath partitioning, it requires solving of the time-dependent Schrödinger equation for the *combined* system rather than the Lioville equation for the reduced density matrix. This construction leads to a number of advantages: the ability to start with the fully correlated initial state, to include properly non-Markovian effects, and in addition, to treat time-dependent fields nonperturbatively. Employing a *finite* Hamiltonian to describe the dynamics of the combined system makes the method well-suited for studying short-time phenomena far from thermal equilibrium.

The presented study summarizes the development of the Surrogate Hamiltonian extending the realm of its applications significantly .

The original construction of the method was limited to phenomena at low temperatures. The new method, presented in **Chapter 4** enables employing the Surrogate Hamiltonian to a wider range of temperatures with more favorable scaling properties. The method is based on averaging over random phase thermal wavefunctions - Boltzmann-weighted, random-phase superpositions of states in the combined system-bath Hilbert space.

The random phase method obtains converged results for thermal observables by averaging a relatively small number of randomly chosen initial states. Moreover the number of initial states required to obtain convergence is a decreasing function of the size of the total Hilbert space due to self-averaging, and it also decreases with temperature. These findings suggest that the Surrogate Hamiltonian method has the same scaling properties for the zero temperature simulation as for the finite temperature simulations. Moreover the finite temperature simulations can be run in parallel since each random phase run is independent of the others. As a consequence, the Surrogate Hamiltonian method can be applied for moderate temperature simulations, as long as the bath modes do not saturate. Moreover, the present thermal random phase method is not restricted to the Surrogate Hamiltonian approach. Since the basic construction is representation-independent, the method could also be used for thermal averaging in the multi-configuration time-dependent Hartree application for dissipative dynamics [119].

The Surrogate Hamiltonian method employs a bath of two-level systems, which has different quantum properties from those of the widely-used harmonic bath. The possibility of entanglement of bath modes, mediated by the primary system supports the fact that there is a conceptual difference between the spin bath and the harmonic baths. The aim of the numerical comparison between the two kinds (presented in **Chapter 3**) was to check if the differences were reflected in the dynamics of the primary system.

The main findings confirmed the fact that in the weak coupling limit the harmonic bath can be mapped to the spin bath [97–99]. In addition, under this limit the spin bath converges with only single excitations of the bath modes, which means that the system and the bath are almost disentangled. This fact is consistent with the convergence to the Markovian limit [142].

The spin and harmonic baths begin to deviate when the initial excitation of the primary system is increased. This difference is observed for excitations where the dynamics generated by the harmonic bath are still Markovian. The first indication of differences is the requirement for two simultaneous bath excitations in order to converge the spin bath. For longer time periods, the spin bath saturates, limiting the ability to assimilate the system's energy. The conclusion is that the limit of weak coupling is more restrictive in the spin bath case. The effect of the saturation can be reduced if the bath Hamiltonian includes a mode-mode coupling term. This term causes diffusion of excitation between the modes, spreading the excitation over a greater number of bath modes. Thus bath modes, which are relatively far from resonance with the primary system become populated and the saturation is suppressed. In practice, this allows increasing the convergence timescale of the spin bath.

The possibility of entanglement of bath modes mediated by the primary system is a major difference between the spin bath and the harmonic bath. After a short initial period where only single excitations occur, in the spin bath entanglement between pairs of spins sets-in with what seems as an exponential growth. Later on the pair entanglement is replaced by higher order terms. All these correlations are absent from the harmonic bath. Nevertheless, the dynamics of the primary systems are not very different, except for systems that have extremely strong coupling. The very similar dynamics observed in the weak and medium coupling cases indicate that from the viewpoint of the reduced dynamics it is hard to distinguish between the two baths.

While the Surrogate Hamiltonian method employs a spin bath, the construction of the bath used in our work is still based on the idea of spectral density. The concept of spectral density is derived from normal mode analysis and therefore intrinsically suffers from the assumption of a weak system-bath coupling. As a result, using the Surrogate Hamiltonian for systems with strong system-bath coupling is questionable, even if there is no formal restriction in the model. Future development of the Surrogate Hamiltonian should focus on a different construction of the spin bath. One of the possibilities is to build the bath from first principles - a strategy, that has already been employed for modeling dissipative dynamics on solid surfaces [94].

Alternative directions may use a random matrix modeling of the environment [145–150].

The effect of dissipation on nonadiabatic dynamics has been discussed in **Chapter 5**. Particularly, the Surrogate Hamiltonian method was applied to a system containing a conical intersection in the presence of a dissipative environment. It is well documented that nonadiabatic transfer events are extremely sensitive to the landscape of the potentials involved [105]. The influence of the dimensionality on nonadiabatic transitions has been acknowledged [106–109]. In this case, the numerical extension of the Surrogate Hamiltonian method to multidimensional models was employed to provide a new insight into nonadiabatic processes. The purpose of the study was to identify a mechanism for extremely rapid transfer of electronic energy into a vibrational one, measured experimentally as a sub-picosecond recovery of the bleach [166–169].

This task posed the challenge of introducing optical observables, which are a direct signature of the ultrafast dynamics, measured in the pump-probe experiments. The use of the Surrogate Hamiltonian has the advantage of an explicit description of the pulse field and its influence on the system-bath interactions. The method enables a consistent treatment of initial correlations between the system and the bath and the dynamical aspects of the pump pulse. All those are absent in most computational models employing the initial state prepared by the Franck-Condon transition from the ground state.

In our model, the non-perturbative approach has been employed to describe the dynamics induced by the strong pump pulse, while the weak probe has been treated within a perturbative picture. This allowed us to associate a quantum mechanical window operator to the absorption of the probe pulse centered at time t. The stimulated emission and absorption have been calculated as expectation values of this window operator. The present modeling of the pump-probe experiment enabled us to investigate the population dynamics, as well as the energy distribution during the nonadiabatic dynamics.

The main findings of our work support the physical picture of rapid curve-crossing in the case of conical intersection. The stimulated emission signals have shown decay on a time-scale of tens of femtoseconds. However, the origin of the fast bleach

recovery, measured in charge-transfer experiments [167–169] remained unclear. The energy relaxation, dominated by an intramolecular vibrational relaxation and monitored by the transient absorption signal, proceeded at a much slower time scale. This suggests that conical mixing symmetry is in itself not sufficient to generate a femtosecond bleach recovery or relaxation.

The comparison between the semi-group approach and the Surrogate Hamiltonian method, introduced in the thesis, supports the findings, that for short dynamics in a weak coupling limit, the two approaches converge [202]. The difference between the two methods lies in the initial correlation and the influence of the excitation pulse on the system bath coupling. The construction of the Surrogate Hamiltonian approach is non-Markovian and therefore it is preferable for treatment of ultra-short dynamics at conical intersections.

From a numerical perspective, the Surrogate Hamiltonian method is advantageous for short simulation times. The wavepacket calculation was faster than the equivalent density operator propagation. For longer times the computational effort of the Surrogate Hamiltonian can become prohibitively expensive due to exponential scaling. The semi-group approach can simulate long time dynamics with linear scaling with time. These findings suggest combining the two methods. The first step of the combined simulation starts using the Surrogate Hamiltonian with a fully correlated system-bath initial state. The Surrogate Hamiltonian is also employed for the pump step, guaranteeing that the influence of the field is included. The reduced system density operator is calculated at the next step, serving as an initial state for a Liouville dynamical simulation. In order to evaluate relaxation parameters entering the Lindblad equation, two approaches have to be compared in a time-window, in which the dynamics are Markovian.

The interaction of an optimized chirped pulse with a molecule embedded in a solvent has been investigated in the study presented in **Chapter 6**. The study was aimed at gaining insight on the interplay between the pulse parameters and the molecular response, which leads to minimal excitation and maximal transmission. This task was carried out by setting simulations which included light-matter interaction in an explicit fashion. The closed-loop feedback strategy has been employed to find the optimal field. The effect of the dissipation on the optimized solutions

has been investigated, and the results of the simulations were compared to the experimental data.

In this thesis the Surrogate Hamiltonian has been developed as an efficient and practical tool. It has shown the ability to treat strongly driven chemical systems consistently, including the system-bath correlations and the influence of electromagnetic fields. The numerical extension of the Surrogate Hamiltonian beyond one dimension (currently to three dimensions) allows the treatment of realistic chemical systems with nonadiabatically coupled potential energy surfaces. The random-phase thermal wavefunction enables numerical simulations at a wider range of temperatures. The limitation of the Surrogate Hamiltonian to short times can be overcome by its combination with the semi-group approach. The combined method enables us, in principle, to simulate long-time dynamics, approaching equilibrium.

Although the Surrogate Hamiltonian is not restricted to a particular type of bath correlation functions, the construction of the bath, formally based on the concept of the spectral density, should be revised. Other dissipative environments should be formulated within the framework of the Surrogate Hamiltonian.

The Surrogate Hamiltonian joins a growing number of theoretical methods, whose aim is to supply comprehensive models for quantum dynamics of many-body systems. Its numerical and physical advantages make us believe that the Surrogate Hamiltonian is an appropriate and even a superior method for treating a wide range of dissipative processes. Nevertheless, the presented study is only the beginning of the journey towards establishing a better understanding of quantum dissipative phenomena.

Appendix A

The representation and propagation of a wave function

The dynamics of a molecular system is represented by a wavefunction propagating in time according to the time-dependent Schrödinger equation,

$$i\frac{\partial}{\partial t}|\Psi(t)\rangle = \hat{\mathbf{H}}|\Psi(t)\rangle \ , \tag{A.1}$$

The starting point is an effective scheme to represent the wavefunction $|\Psi\rangle$. Within this scheme, the basic mapping operation generated by the operator $\hat{\mathbf{H}}$ has to be defined.

A.1 The grid representation

Representing the state $|\Psi(t)\rangle$ in the Schrödinger picture as a wave function $\langle q|\Psi(t)\rangle = \Psi(q,t)$ on a grid in coordinate space is an extremely flexible choice. It allows for the treatment of a broad class of problems independent of the shape of the potential energy surfaces.

A wave function $\Psi(q)$ can be approximated by a finite set of analytical functions (see for example [3, 6])

$$\Psi(q) \approx \sum_{n=1}^{N_f} a_n g_n(q) \ . \tag{A.2}$$

The expansion coefficients are determined by matching the approximation to the

true wave function at N_g grid points q_j,

$$\Psi(q_j) \equiv \sum_{n=1}^{N_g} a_n g_n(q_j) \; . \tag{A.3}$$

If the $g_n(q)$ are orthogonal functions and $N_f = N_g$, the expansion coefficients are given by

$$a_n = \sum_{n=1}^{N_f} \Psi^*(q_j) g_n(q_j) \; . \tag{A.4}$$

A special case of the orthogonal representation is the Fourier method [3]. The functions $g_n(q)$ are then chosen as plain waves,

$$g_n(q) = \mathsf{e}^{2\pi i n q/L} \, , \quad n = -\left(\frac{N_f}{2} - 1\right), \ldots, 0, \ldots, \frac{N_f}{2} \, , \tag{A.5}$$

with equally spaced sampling points $q_j = (j-1)\Delta q$ on a grid of length L. The approximation of the wave function becomes

$$\Psi(q) \approx \sum_{n=-\left(N_f/2-1\right)}^{N_f/2} a_n \, \mathsf{e}^{2\pi i n q/L} \, , \tag{A.6}$$

and the Fourier expansion coefficients,

$$a_n = \frac{1}{N_f} \sum_{n=1}^{N_f} \Psi(q_j) \, \mathsf{e}^{-2\pi i n q_j/L} \, , \tag{A.7}$$

represent the amplitude of the wave function in Fourier, or momentum, space. The grid distance in momentum space is given by $\Delta p = 2\pi/L$, the grid distance in coordinate space is related to the largest representable momentum by $\Delta q = \pi/p_{max}$.

The power of the Fourier method results from the fact that the operators entering the Hamiltonian can each be applied locally in coordinate or momentum space, and the transformation connecting these two representations is the fast Fourier transform with its favorable scaling of $N_f \log(N_f)$. All operator functions depending on $\hat{\mathbf{q}}$ like the potential energy operator correspond to diagonal matrices in coordinate space, and the wave function $\Psi(q_j)$ can simply be multiplied by them. The kinetic energy operator as well as other operator functions depending on $\hat{\mathbf{p}}$ can be applied by multiplication in momentum space,

$$T(p_j)\Psi(p_j) = \frac{p_j^2}{2m}\Psi(p_j) \tag{A.8}$$

where m is mass and p_j are the momentum space grid points.

A.2 The Chebychev propagator

The Chebychev method [236] employs the idea of a polynomial expansion of the time evolution operator,

$$\hat{\mathbf{U}}(t) = \mathsf{e}^{-i\hat{\mathbf{H}}t} \approx \sum_{n=0}^{N} a_n P_n(-i\hat{\mathbf{H}}t) \tag{A.9}$$

with complex Chebychev polynomials $P_n(\hat{\mathbf{X}}) = \Phi_n(\hat{\mathbf{X}})$ as basis set. The complex Chebychev polynomials are defined in the range $[-i, i]$. Therefore the ″has to be renormalized by its spectral range $\Delta E = E_{max} - E_{min}$, and for efficiency it should be shifted such that the spectral range is $[-1, 1]$:

$$\hat{\mathbf{H}}_{norm} = 2\frac{\hat{\mathbf{H}} - \mathbb{1}(\frac{1}{2}\Delta E + V_{min})}{\Delta E} \,. \tag{A.10}$$

Inserting Eq. (A.10) into Eq. (A.9) leads to

$$\Psi(t) = \hat{\mathbf{U}}(t)\Psi(0) \approx \mathsf{e}^{-i(\frac{1}{2}\Delta E + V_{min})t} \sum_{n=0}^{N} a_n(\alpha)\Phi_n(-i\hat{\mathbf{H}}_{norm})\Psi(0) \tag{A.11}$$

with the argument $\alpha = \Delta E t/2$. The expansion coefficients are related to the Bessel functions of the first kind J_n:

$$a_n(\alpha) = \int_{-i}^{i} dx \frac{\mathsf{e}^{i\alpha x}\Phi_n(x)}{\sqrt{1-x^2}} = 2J_n(\alpha) \,, \tag{A.12}$$

and the Chebychev polynomials are calculated using the recursion relation

$$\begin{aligned} &\Phi_{n+1}(x) = 2x\Phi_n(x) - \Phi_{n-1}(x) \,, \\ &\Phi_0(x) \equiv 1 \,, \quad \Phi_1(x) = x \,. \end{aligned} \tag{A.13}$$

The error of the Chebychev method is uniformly distributed over the whole range of eigenvalues of $\hat{\mathbf{H}}$ and can be reduced to machine precision due to a property of the Bessel functions $J_n(\alpha)$: When the order n becomes larger than the argument α, J_n decreases exponentially fast. The number of terms required in the expansion is therefore determined by the spectral range of the ″and by the desired time step. It should be noted that the time step does not affect the accuracy of the method. The Chebychev method is therefore suited for large time steps, and a practical lower limit imposed by numerical efficiency is about 40 terms in the expansion [3].

A.3 Eigenfunctions through imaginary time propagation

The Fourier method can also be used to compute eigenvalues and eigenfunctions of a given Hamiltonian [114]. To this end the imaginary time $\tau = it$ is introduced into the formal solution of the time-dependent Schrödinger equation,

$$|\Psi(\tau)\rangle = \mathrm{e}^{-\hat{\mathbf{H}}\tau}|\Psi(0)\rangle \; . \tag{A.14}$$

An arbitrary initial guess wave function can be expanded into eigenstates of the Hamiltonian, $|\Psi(0)\rangle = \sum_n c_n|\varphi_n\rangle$. For $\tau \to \infty$, only the ground state component of the initial guess will survive. The imaginary time propagation, Eq. (A.14), is obviously not unitary, the wave function therefore needs to be renormalized during propagation.

The choice of the initial guess determines the convergence of the method. The energy expectation value, $\langle\Psi(\tau)|\hat{\mathbf{H}}|\Psi(\tau)\rangle$, or the standard deviation of energy, $\langle\Psi(\tau)|\hat{\mathbf{H}}^2|\Psi(\tau)\rangle - \langle\Psi(\tau)|\hat{\mathbf{H}}|\Psi(\tau)\rangle^2$, which is a measure of the purity of the eigenstate, is monitored to determine convergence. Higher eigenstates than the ground state can be calculated by projecting out lower lying eigenstates, i.e. to obtain the nth eigenstate a new Hamiltonian,

$$\hat{\mathbf{H}}_n = \hat{\mathbf{H}} - \sum_{i=0}^{n-1} |\varphi_i\rangle\langle\varphi_i| \tag{A.15}$$

can be defined and used in Eq. (A.14). Since all lower lying eigenstates $|\varphi_i\rangle$ need to be stored to compute $|\varphi_n\rangle$, this is feasible only for a few eigenstates. Furthermore, long propagation times τ are necessary to differentiate between nearly degenerate states due to a time-energy uncertainty relation.

However, imaginary time propagation with the Hamiltonian, Eq. (A.15), represents a special choice of the more general Filter Diagonalization approach [115–117]. The basic idea of Filter Diagonalization to extract eigenvalues and eigenstates of a given operator consists of a combined use of applying a filter and algebraic diagonalization [115]. The correlations present in the initial guess are eliminated through a short-time filter between distant eigenstates and by diagonalization between closely lying eigenstates [115–117]. Imaginary time propagation can be viewed as a long term filter, with no diagonalization part. It is therefore less efficient than full filter

diagonalization, but it requires only minor changes of existing programs.

Appendix B

The bit representation of a bath of two level systems

More comprehensive description of numerical features of the Surrogate Hamiltonian method is given in Ref. [88, 95, 237].

B.1 The wave function

The state of the system combined with the bath is described by a 2^N-dimensional spinor with N being the number of modes. The dimension 2^N results from the number of possibilities to combine 2 states (spin-up/spin-down, bath mode excited/not excited, bit set/not set) N times.

For $N = 1$ and $N = 2$, respectively, this wave function spinor becomes

$$\Psi^{N=1}(\hat{\mathbf{Q}}) = \begin{pmatrix} \psi_0(\hat{\mathbf{Q}}, \alpha) \\ \psi_1(\hat{\mathbf{Q}}, \alpha) \end{pmatrix} , \quad \Psi^{N=2}(\hat{\mathbf{Q}}) = \begin{pmatrix} \psi_0(\hat{\mathbf{Q}}, \alpha) \\ \psi_1(\hat{\mathbf{Q}}, \alpha) \\ \psi_2(\hat{\mathbf{Q}}, \alpha) \\ \psi_3(\hat{\mathbf{Q}}, \alpha) \end{pmatrix} , \tag{B.1}$$

where $\hat{\mathbf{Q}}$ represents the nuclear degrees of freedom of the wave function and α the electronic degrees of freedom. The spinor is bit ordered, i.e. the kth bit set in the spinor index corresponds to the ith TLS mode excited if the counting of bits starts at $k = 0$. This means that the zeroth component corresponds to no bath mode being excited, the first and second component to the excitation of the first and second bath mode, and the third component corresponds to the first and second bath mode

being excited *simultaneously*, and so forth.

The number of simultaneous excitations can be restricted. The occurrence of the kth excitation in N bits is a combination,

$$\binom{N}{k} = \frac{N!}{k!(N-k)!} \ .$$

The dimension of the spinor D is then given by the sum of binomial coefficients

$$D = \sum_{k=0}^{N_{exc}} \binom{N_{exc}}{k} \tag{B.2}$$

with N_{exc} the number of simultaneously allowed excitations. Assume a bath with 4 modes and at most 2 simultaneous excitations. Then D is:

$$D = \binom{4}{0} + \binom{4}{1} + \binom{4}{2} = 1 + 4 + 6 = 11 \ ,$$

which means there is one spinor component corresponding to none of the bath modes excited, four components have one bit set and there are 6 possibilities to excite 2 bits out of 4. Making use of the Binomial Theorem

$$(a+b)^N = \sum_{k=0}^{N} \binom{N}{k} a^{N-k} b^k$$

with $a = b = 1$, it again is found that $D = 2^N$ if all N excitations are allowed simultaneously. The restriction of simultaneously allowed excitations leads to significant numerical savings, both in computation time and storage, and its validity can simply be checked by increasing N_{exc}.

B.2 The operators

The bath operators entering the Hamiltonian are sums over the operators acting on a single mode. In bit representation the operator of mode k acts on bit k (assuming $k = 0, \ldots, N-1$), i.e. on the spinor components which have the kth bit set in their indices. One should clearly distinguish between bath modes and spinor components. For example, the $k = 0$ mode which may or may not be excited should not be confused with the zeroth spinor component corresponding to all modes deexcited.

As a simple example, consider the operator $\hat{\mathbf{S}}_z = \frac{1}{2}\left(\begin{smallmatrix} -1 & 0 \\ 0 & +1 \end{smallmatrix}\right)$ and a bath consisting of $N = 3$ modes. Then the total $\hat{\mathbf{S}}_z^{(N=3)}$ is a diagonal 8×8-matrix. The $\hat{\mathbf{S}}_z^{(k=2)}$ acts on

the total 8-dimensional space with the first four diagonal elements -1 since the $k = 2$ bit is 0, i.e. the third mode is not excited, and the second four diagonal elements $+1$ since the $k = 2$ bit is 1, i.e. the third mode is excited. The $\hat{\mathbf{S}}_z^{(k=1)}$-operator acting on the second mode acts on the two 4-dimensional subspaces with the first two diagonal elements -1 and the second two $+1$. Finally the $\hat{\mathbf{S}}_z^{(k=0)}$-operator acts on the four 2-dimensional subspaces. Since the total $\hat{\mathbf{S}}_z^{(N=3)}$-operator is the sum over the $\hat{\mathbf{S}}_z^k$ operators, its bit representation is given by

$$S_z^{(N=3)} = \frac{1}{2}\begin{pmatrix} -3 & 0 & \cdots & & & & & \\ 0 & -1 & 0 & \cdots & & & & \\ \cdots & 0 & -1 & 0 & \cdots & & & \\ \cdots & & 0 & +1 & 0 & \cdots & & \\ \cdots & & & 0 & -1 & 0 & \cdots & \\ \cdots & & & & 0 & +1 & 0 & \cdots \\ \cdots & & & & & 0 & +1 & 0 \\ \cdots & & & & & & 0 & +3 \end{pmatrix} . \tag{B.3}$$

However, this matrix neither needs to be stored nor explicitly computed. Instead, the fact that computers are built on bit operations and modern programming languages offer built-in functions for testing for and operating on bits can be used.

The occupation number $\hat{\mathbf{n}}_k$ needed in the bath Hamiltonian, Eq. (2.2), can be computed in a similar fashion. The matrix representation for two modes is given by

$$\sum_{k=0}^{1} \varepsilon_k \hat{\mathbf{n}}_k = \begin{pmatrix} 0 & 0 & 0 & 0 \\ 0 & \varepsilon_0 & 0 & 0 \\ 0 & 0 & \varepsilon_1 & 0 \\ 0 & 0 & 0 & \varepsilon_0 + \varepsilon_1 \end{pmatrix} . \tag{B.4}$$

If more complicated operators acting on the bath shall be obtained, it is useful to write down rigorously how to build bath operators acting in D-dimensional space from spin operators acting in two-dimensional space. All bath operators can be expressed as a combination of creation and annihilation operators. The creation operator for mode k can be written as

$$\hat{\boldsymbol{\sigma}}_k^{+N} = \prod_{j=1}^{N-k} \mathbb{1}_2 \otimes \hat{\boldsymbol{\sigma}}^+ \otimes \prod_{j=1}^{k-1} \mathbb{1}_2 \tag{B.5}$$

with

$$\hat{\boldsymbol{\sigma}}^{+} = \begin{pmatrix} 0 & 0 \\ 1 & 0 \end{pmatrix} , \tag{B.6}$$

and the kth annihilator is given by the conjugated expression built on $\hat{\boldsymbol{\sigma}}$. With the help of Eq. (B.6) the bath operators needed in the interaction Hamiltonian, Eq. (2.5), can now be constructed.

The matrix representation of $\sum_k d_k(\hat{\boldsymbol{\sigma}}_k^{+} + \hat{\boldsymbol{\sigma}}_k)$ describing energy relaxation has already been given [88], it is noted here for completeness:

$$\sum_k d_k(\hat{\boldsymbol{\sigma}}_k^{+} + \hat{\boldsymbol{\sigma}}_k) = \begin{pmatrix} 0 & d_0 & d_1 & 0 & d_2 & 0 & 0 & 0 \\ d_0 & 0 & 0 & d_1 & 0 & d_2 & 0 & 0 \\ d_1 & 0 & 0 & d_0 & 0 & 0 & d_2 & 0 \\ 0 & d_1 & d_0 & 0 & 0 & 0 & 0 & d_2 \\ d_2 & 0 & 0 & 0 & 0 & d_0 & d_1 & 0 \\ 0 & d_2 & 0 & 0 & d_0 & 0 & 0 & d_1 \\ 0 & 0 & d_2 & 0 & d_1 & 0 & 0 & d_0 \\ 0 & 0 & 0 & d_2 & 0 & d_1 & d_0 & 0 \end{pmatrix} . \tag{B.7}$$

The upper triangle in Eq. (B.7) corresponds to annihilation, and the lower triangle to creation of bath modes. The action of the bath operators $\sum_k d_k(\hat{\boldsymbol{\sigma}}_k^{+} + \hat{\boldsymbol{\sigma}}_k)$ is given by an exclusive *or*, which is true only if one of the bit is 1 while the other is 0. To illustrate the exclusive *or*, for example for $N = 3$ the fourth spinor component is obtained from

$$\tilde{\Psi}_4 \;=\; \underbrace{d_2\Psi_0}_{\text{creation}} \;+\; \underbrace{d_0\Psi_5 + d_1\Psi_6}_{\text{annihilation}}$$

with

$d_2 \to 2^2:$	100	$d_0 \to 2^0:$	001	$d_1 \to 2^1:$	010
$\Psi_0 \to 0:$	$\underline{000}$	$\Psi_5 \to 5:$	$\underline{101}$	$\Psi_6 \to 6:$	$\underline{110}$
$\tilde{\Psi}_4 \to 4:$	100		100		100

(it should be remembered that bits are counted from right to left starting from 0). In the above example, all combinations of 2^k and j leading to $i = 4$ are listed. For

all other combinations the exclusive *or* leads to false, i.e.

$$\begin{aligned} d_2 \to 2^2: \quad & 100 & \qquad d_0 \to 2^0: \quad & 001 \\ \Psi_1 \to 1: \quad & \underline{001} & \qquad \Psi_6 \to 6: \quad & \underline{110} \\ \tilde{\Psi}_4 \to 4 \neq 5: \quad & 101 & \qquad \tilde{\Psi}_4 \to 4 \neq 7: \quad & 111\,. \end{aligned}$$

The dephasing operator $\hat{\mathbf{O}} = \sum_{kl} c_{kl}(\hat{\boldsymbol{\sigma}}_k^+ \hat{\boldsymbol{\sigma}}_l + \hat{\boldsymbol{\sigma}}_l^+ \hat{\boldsymbol{\sigma}}_k)$ reads for $N = 3$ modes

$$\sum_{k,l=0}^{2} O_{kl} = \begin{pmatrix} 0 & 0 & 0 & 0 & 0 & 0 & 0 & 0 \\ 0 & 0 & c_{01} & 0 & c_{02} & 0 & 0 & 0 \\ 0 & c_{10} & 0 & 0 & c_{12} & 0 & 0 & 0 \\ 0 & 0 & 0 & 0 & 0 & c_{12} & c_{02} & 0 \\ 0 & c_{20} & c_{21} & 0 & 0 & 0 & 0 & 0 \\ 0 & 0 & 0 & c_{21} & 0 & 0 & c_{01} & 0 \\ 0 & 0 & 0 & c_{20} & 0 & c_{10} & 0 & 0 \\ 0 & 0 & 0 & 0 & 0 & 0 & 0 & 0 \end{pmatrix} . \tag{B.8}$$

The application of Eq. (B.8), $\Psi_i = \sum_{kl} O_{kl} \Psi_j$, requires several bit tests: First, the number of excitations in the spinor indices i and j must be equal. This corresponds to the requirement that dephasing doesn't alter the energy of the bath, i.e. conserves the number of bath excitations. Second, the indices of O_{kl} in Eq. (B.8) numbering the bath modes bit-added, $k+l$, must be equal to the exclusive *or* of i and j. This is a generalization of the single application of the exclusive *or* described in the previous paragraph for the case when only one bath operator acts on the spinor, and not two consecutively.

Appendix C

Harmonic bath vs spin bath

The differences between harmonic and spin baths can be illuminated by studying the simple system of a spin-$\frac{1}{2}$ coupled to a bath. For the harmonic bath the total Hamiltonian in second quantization is given by:

$$\hat{\mathbf{H}} = \frac{1}{2}\Omega\hat{\sigma}_z + \sum_j \omega_j \hat{\mathbf{b}}_j^+ \hat{\mathbf{b}}_j + \sum_j \lambda_j(\hat{\mathbf{b}}_j + \hat{\mathbf{b}}_j^+)(\hat{\sigma}_+ + \hat{\sigma}_-) \ . \tag{C.1}$$

Thus the Heisenberg equations of motion for the system operators are:

$$\frac{d}{dt}\hat{\sigma}_\pm = \frac{1}{i}[\hat{\sigma}_\pm, \hat{\mathbf{H}}] = \pm i\Omega\hat{\sigma}_\pm - i\hat{\sigma}_z \sum_j \lambda_j(\hat{\mathbf{b}}_j + \hat{\mathbf{b}}_j^+) \ . \tag{C.2}$$

Similarly, the equations of motion for the bath operators are:

$$\frac{d}{dt}\hat{\mathbf{b}}_j = -i\omega_j\hat{\mathbf{b}}_j - i\lambda_j(\hat{\sigma}_+ + \hat{\sigma}_-) \ . \tag{C.3}$$

Since the annihilation and creation operators $\hat{\mathbf{b}}_j$ and $\hat{\mathbf{b}}_j^+$, satisfy the standard Bose commutation relation, $[\hat{\mathbf{b}}_j, \hat{\mathbf{b}}_{j'}^+] = \delta_{j,j'}$, a closed set of equations is obtained for each of the independent bath modes.

Now, let us consider a different model, where the primary system is coupled to a bath of spins-$\frac{1}{2}$. The total Hamiltonian may be written in the form:

$$\hat{\mathbf{H}} = \Omega\hat{\sigma}_z^0 + \frac{1}{2}\sum_j \omega_j \hat{\boldsymbol{\sigma}}_z^j - \frac{1}{2}\sum_j \lambda_j \hat{\sigma}_+^0 \hat{\boldsymbol{\sigma}}_-^j + h.c. \ , \tag{C.4}$$

where $\hat{\boldsymbol{\sigma}}_{x,y,z}$ designates the set of Pauli operators and $\hat{\boldsymbol{\sigma}}_\pm^i = \hat{\boldsymbol{\sigma}}_x^i \pm \hat{\boldsymbol{\sigma}}_y^i$ are the usual ladder operators. For simplicity, we consider a system (0) consisting of a spin-$\frac{1}{2}$ which interacts with a pair (1,2) of spins. Thus, the Hamiltonian of the whole

system reads:

$$\hat{\mathbf{H}} = \Omega\hat{\sigma}_z^0 + \frac{1}{2}(\omega_1\hat{\boldsymbol{\sigma}}_z^1 + \omega_2\hat{\boldsymbol{\sigma}}_z^2) - \frac{\lambda_1}{2}(\hat{\sigma}_+^0\hat{\boldsymbol{\sigma}}_-^1 + \hat{\sigma}_-^0\hat{\boldsymbol{\sigma}}_+^1) - \frac{\lambda_2}{2}(\hat{\sigma}_+^0\hat{\boldsymbol{\sigma}}_-^2 + \hat{\sigma}_-^0\hat{\boldsymbol{\sigma}}_+^2) \; . \tag{C.5}$$

The Heisenberg equations of motion for the system operator are:

$$\frac{d}{dt}\hat{\sigma}_\pm^0 = \pm i(2\Omega\hat{\sigma}_\pm^0 + \frac{\lambda_1}{2}\hat{\sigma}_z^0\hat{\boldsymbol{\sigma}}_\pm^1 + \frac{\lambda_2}{2}\hat{\sigma}_z^0\hat{\boldsymbol{\sigma}}_\pm^2) \; , \tag{C.6}$$

and the equation of motion for the bath operator reads:

$$\frac{d}{dt}\hat{\boldsymbol{\sigma}}_\pm^{1,2} = \pm i(\omega_{1,2}\hat{\boldsymbol{\sigma}}_\pm^{1,2} + \frac{\lambda_{1,2}}{2}\sigma_\pm^0\hat{\boldsymbol{\sigma}}_z^{1,2}) \; . \tag{C.7}$$

The commutation relations for spin operators are different from those of bosons:

$$[\hat{\boldsymbol{\sigma}}_i, \hat{\boldsymbol{\sigma}}_j] = -2i\hat{\boldsymbol{\sigma}}_k \; , \tag{C.8}$$

which makes the set of the equations above non-closed. After some algebra, the equation for the bath operators becomes:

$$\frac{d}{dt}(\hat{\sigma}_z^0\hat{\boldsymbol{\sigma}}_\pm^{1,2}) = \pm i\omega_{1,2}\hat{\sigma}_z^0\hat{\boldsymbol{\sigma}}_\pm^{1,2} \pm i\frac{\lambda_1}{2}\hat{\sigma}_\pm^0 + i\lambda_2(\hat{\sigma}_+^0\hat{\boldsymbol{\sigma}}_\pm^{1,2}\hat{\boldsymbol{\sigma}}_-^{2,1} - \hat{\sigma}_-^0\hat{\boldsymbol{\sigma}}_\pm^{1,2}\hat{\boldsymbol{\sigma}}_+^{2,1}) \; . \tag{C.9}$$

The triple correlations of the type $\hat{\sigma}_+^0\hat{\boldsymbol{\sigma}}_\pm^1\hat{\boldsymbol{\sigma}}_-^2$ is a manifestation of the build-up of *quantum entanglement* - a specific correlation between different modes, which has no analogy in classical physics. These correlations make a difference between the spin bath and the harmonic oscillator one, since the latter does not have quantum correlations between the bath modes.

Appendix D

Entanglement between different bath modes

In order to check whether the reduced *two-system* density matrix $\hat{\boldsymbol{\rho}}$ is entangled, first we will use the partial transposition criterion proposed by Peres [137] and Horodecki et al. [138]. A mixed state described by density matrix $\hat{\boldsymbol{\rho}}$ is non-separable (and therefore cannot be written as a product state of two subsystems (i) and (j), $\hat{\boldsymbol{\rho}} = \hat{\boldsymbol{\rho}}_i \otimes \hat{\boldsymbol{\rho}}_j$), iff the partial transposition of $\hat{\boldsymbol{\rho}}$ with respect to one of the two subsystems has negative eigenvalues. The partial transpose $\hat{\boldsymbol{\rho}}^{\mathsf{T_j}}$ is obtained by transposing in a matrix representation of $\hat{\boldsymbol{\rho}}$ only those indices corresponding to subsystem (j), i.e. $\rho^{\mathsf{T_j}}_{m\mu,n\nu} = \rho_{m\nu,n\mu}$. The following notation for matrix elements of a composite system is used:

$$\rho_{m\mu,n\nu} = \langle e_m \otimes f_\mu | \hat{\boldsymbol{\rho}} | e_n \otimes f_\nu \rangle \ , \tag{D.1}$$

where e_m and f_μ denote the arbitrary orthonormal bases in Hilbert space describing the first (i) and second (j) system, respectively.

Checking the positivity of the partial transpose is equivalent to checking the signs of the eigenvalues of $\hat{\boldsymbol{\rho}}^{\mathsf{T_j}}$ or ,alternatively, the signs of the following determinants:

$$W_1 = \rho^{\mathsf{T_j}}_{11,11}\rho^{\mathsf{T_j}}_{22,22} - \rho^{\mathsf{T_j}}_{11,22}\rho^{\mathsf{T_j}}_{22,11}, \tag{D.2}$$

$$W_2 = \rho^{\mathsf{T_j}}_{12,12}\rho^{\mathsf{T_j}}_{21,21} - \rho^{\mathsf{T_j}}_{12,21}\rho^{\mathsf{T_j}}_{21,12}. \tag{D.3}$$

In the case when one of the above determinants is negative, the state $\hat{\boldsymbol{\rho}}$ is non-separable, and hence there is entanglement between the two subsystems $\hat{\boldsymbol{\rho}}_i$, $\hat{\boldsymbol{\rho}}_j$.

Another entanglement measure for a mixed state of two spin-$\frac{1}{2}$ particles is the

entanglement of formation [139–141]. Explicitly, for the reduced two-system density matrix $\hat{\boldsymbol{\rho}}$ the entanglement of formation is defined by

$$E(\rho) = h\left(\frac{1}{2}\left[1+\sqrt{1-\mathcal{C}(\rho)^2}\right]\right) , \tag{D.4}$$

where h is the binary entropy function $h(x) = -x\log_2 x - (1-x)\log_2(1-x)$ and $\mathcal{C}(\rho)$ is the concurrence. The concurrence is calculated in the following way: first we define the "spin-flipped" density matrix to be

$$\widetilde{\rho} = (\sigma_y \otimes \sigma_y)\rho^*(\sigma_y \otimes \sigma_y) , \tag{D.5}$$

where the asterisk denotes complex conjugation of $\hat{\boldsymbol{\rho}}$ in the standard basis $\{|00\rangle, |01\rangle, |10\rangle, |11\rangle, \}$ and σ_y expressed in the same basis is the matrix

$$\sigma_y = \begin{pmatrix} 0 & -i \\ i & 0 \end{pmatrix} . \tag{D.6}$$

As both ρ and $\widetilde{\rho}$ are positive operators, it follows that the product $\rho\widetilde{\rho}$, though non-Hermitian, also has only real and non-negative eigenvalues. Let the square roots of these eigenvalues, in decreasing order , be λ_1, λ_2, λ_3, and λ_4. Then the concurrence of the density matrix ρ is defined as $\mathcal{C} = \max\{\lambda_1 - \lambda_2 - \lambda_3 - \lambda_4, 0\}$. It should be noted that $\mathcal{C} = 0$ corresponds to a non-entangled state, while $\mathcal{C} = 1$ - to a completely entangled state and the entanglement of formation E is a monotonically increasing function of $\mathcal{C}$.

Bibliography

[1] A. H. Zewail, *Femtochemistry - Ultrafast Dynamics of the Chemical Bond*, World Scientific, Singapore, 1994

[2] J. Manz and L. Wöste, editors, *Femtosecond Chemistry*, VCH, Weinheim, 1995

[3] R. Kosloff, J. Phys. Chem. **92**, 2087 (1988)

[4] R. Kosloff, *"The Fourier Method", in Numerical Grid Methods and Their Application to Schrödinger equation*, Kluwer Academic, The Netherlands, 1993

[5] C. Leforestier, R. H. Bisseling, C. Cerjan, and et al., J. Comp. Phys. **94**, 59 (1991)

[6] R. Kosloff, *"Quantum Molecular Dynamics on Grids" in Dynamics of Molecules and Chemical Reactions*, Marcel Dekker, New York, 1996

[7] U. Weiss, *Quantum Dissipative Systems*, World Scientific, Singapore, 1999

[8] E. B. Davies, *Quantum Theory of Open Systems*, Academic Press, London, 1976

[9] R. Alicki, arXiv:quant-ph **0205173** (2002)

[10] S. Nakajima, Prog. Theor. Phys. **20**, 948 (1958)

[11] R. Zwanzig, J. Chem. Phys. **33**, 1338 (1960)

[12] R. Zwanzig, J. Stat. Phys. **9**, 215 (1973)

[13] T. Arimitsu, Y. Takahashi, and F. Shibata, Physica A **100**, 507 (1980)

[14] F. Haake, *Quantum Statistics in Optics and Solid State Physics*, Springer-Verlag, Berlin, 1973

[15] N. G. van Kampen, *Stochastic Processes in Physics and Chemistry*, North-Holland, Amsterdam, 1992

[16] R. Alicki and K. Lendi, *Quantum Dynamical Semigroups and Applications*, Springer-Verlag, Berlin, 1987

[17] F. Bloch, Phys. Rev. **105**, 1206 (1957)

[18] A. G. Redfield, Phys. Rev. **98**, 1787 (1955)

[19] A. G. Redfield, IBM J. Res. Dev. **1**, 19 (1957)

[20] K. Blum, *Density Matrix Theory and Applications*, Plenum, New York, 1981

[21] W. T. Pollard, A. K. Felts, and R. A. Friesner, Adv. Chem. Phys. **93**, 77 (1996)

[22] V. May and O. Kühn, *Charge and Energy Transfer Dynamics in Molecular Sysrems*, Wiley-VCH, Berlin, 2000

[23] V. Romero-Rochin and I. Oppenheim, Physica A **155**, 52 (1989)

[24] J. Cao, J. Chem. Phys. **107**, 3204 (1997)

[25] D. Kohen, C. C. Martson, and D. Tannor, J. Chem. Phys. **107**, 5236 (1997)

[26] E. Geva, E. Rosenman, and D. Tannor, J. Chem. Phys. **113**, 1380 (2000)

[27] B. B. Laird, J. Budimir, and J. L. Skinner, J. Chem. Phys. **94**, 4391 (1991)

[28] D. R. Reichman and R. J. Silbey, J. Chem. Phys. **194**, 1506 (1996)

[29] S. Jang, J. Cao, and R. J. Silbey, J. Chem. Phys. **116**, 2705 (2002)

[30] A. A. Golosov and D. R. Reichman, J. Chem. Phys. **115**, 9848 (2001)

[31] A. A. Golosov and D. R. Reichman, J. Chem. Phys. **115**, 9862 (2001)

[32] Q. Shi and E. Geva, **119**, 12063 (2003)

[33] Y. Tanimura and P. G. Wolynes, Phys. Rev. A **43**, 4131 (1991)

[34] J. Wilkie, Phys. Rev. E **62**, 8808 (2000)

[35] T. Mančal and V. May, Chem. Phys. **268**, 201 (2001)

[36] R. Xu and Y. J. Yan, J. Chem. Phys. **116**, 9196 (2002)

[37] U. Kleinekathöfer, J. Chem. Phys. **121**, 2505 (2004)

[38] C. Meier and D. Tannor, J. Chem. Phys. **111**, 3365 (1999)

[39] F. Haake and R. Reibold, Phys. Rev. A **32**, 2462 (1985)

[40] A. Suárez, R. Silbey, and I. Oppenheim, J. Chem. Phys. **97**, 5101 (1992)

[41] P. Pechukas, Phys. Rev. Lett. **73**, 1060 (1994)

[42] G. Lindblad, Commun. Math. Phys. **48**, 119 (1976)

[43] V. Gorini, A. Kossokowski, and E. C. G. Sudarshan, J. Math. Phys. **17**, 821 (1976)

[44] K. Kraus, Ann. Phys. **64**, 311 (1971)

[45] D. W. Oxtoby, Annu. Rev. Phys. Chem. **32**, 77 (1981)

[46] J. L. Skinner, Annu. Rev. Phys. Chem. **39**, 463 (1988)

[47] E. Geva, R. Kosloff, and J. Skinner, J. Chem. Phys. **102**, 8541 (1995)

[48] N. Gisin and I. C. Percival, J. Phys. A: Math. Gen. **25**, 5677 (1992)

[49] J. Dalibard, Y. Castin, and K. Molmer, Phys. Rev. Lett. **68**, 580 (1992)

[50] L. Diósi, N. Gisin, and W. T. Strunz, Phys. Rev. A **58**, 1699 (1998)

[51] P. Gaspard and M. Nagaoka, J. Chem. Phys. **111**, 5676 (1999)

[52] H. P. Breuer and F. Petruccione, Phys. Rev. Lett. **74**, 3788 (1995)

[53] H. P. Breuer, B. Kappler, and F. Petruccione, Phys. Rev. A **59**, 1633 (1999)

[54] R. Kosloff, M. A. Ratner, and W. B. Davis, J. Chem. Phys. **106**, 7036 (1997)

[55] O. Prezhdo, J. Chem. Phys. **111**, 8366 (1999)

[56] I. de Vega, D. Alonso, P. Gaspard, and W. T. Strunz, J. Chem. Phys. **122**, 124106 (2005)

[57] R. P. Feynman and A. R. Hibbs, *Quantum Mechanics and Path Integrals*, McGraw-Hill, New York, 1965

[58] R. Feynman and F. Vernon, Ann. Phys. **24**, 118 (1963)

[59] P. G. Wolynes, Phys. Rev. Lett. **47**, 968 (1981)

[60] A. O. Caldeira and A. J. Leggett, Ann. Phys. **149**, 374 (1983)

[61] R. D. Coalson, J. Chem. Phys. **86**, 995 (1987)

[62] C. H. Mak and D. Chandler, Phys. Rev. A **44**, 2352 (1991)

[63] R. Egger and U. Weiss, Z. Phys. B: Condens. Matter **89**, 97 (1992)

[64] M. Winterstetter and W. Domcke, Chem. Phys. Lett. **236**, 445 (1995)

[65] M. Winterstetter and U. Weiss, Chem. Phys. **217**, 155 (1997)

[66] M. Topaler and N. Makri, J. Chem. Phys. **101**, 7500 (1994)

[67] D. Makarov and N. Makri, Chem. Phys. Lett. **221**, 482 (1994)

[68] E. Sim and N. Makri, J. Phys. Chem. B **101**, 5446 (1997)

[69] J. S. Shao and N. Makri, J. Chem. Phys. **116**, 507 (2002)

[70] A. A. Golosov, S. I. Tsonchev, P. Pechukas, and R. A. Friesner, J. Chem. Phys. **111**, 9918 (1999)

[71] A. A. Golosov and D. R. Reichman, J. Chem. Phys. **115**, 9862 (2001)

[72] J. C. Tully, J. Chem. Phys. **93**, 1061 (1990)

[73] G. D. Billing, J. Chem. Phys. **99**, 5849 (1993)

[74] E. Rabani, G. Krilov, and B. J. Berne, J. Chem. Phys. **112**, 2605 (2000)

[75] E. Sim, G. Krilov, and B. Berne, J. Phys. Chem. A **105**, 2824 (2001)

[76] J. A. Poulsen and P. J. Rossky, J. Chem. Phys. **115**, 8024 (2001)

[77] A. A. Golosov, D. R. Reichman, and E. Rabani, J. Chem. Phys. **118**, 457 (2003)

[78] G. A. Voth, Adv. Chem. Phys. **93**, 135 (1996)

[79] E. Geva, Q. Shi, and G. A. Voth, J. Chem. Phys. **115**, 9209 (2001)

[80] S. Jang and G. A. Voth, J. Chem. Phys. **111**, 2371 (1999)

[81] D. R. Reichman and E. Rabani, Phys. Rev. Lett. **87**, 265702 (2001)

[82] E. Rabani and D. R. Reichman, J. Chem. Phys. **116**, 6271 (2002)

[83] E. J. Heller, J. Chem. Phys. **94**, 2723 (1991)

[84] N. Makri, J. Phys. Chem. B **103**, 2823 (1999)

[85] K. Thompson and N. Makri, Phys. Rev. E **59**, 4729 (1999)

[86] H. Wang, X. Sun, and W. H. Miller, J. Chem. Phys. **108**, 9726 (1998)

[87] E. Pollak and J. Liao, J. Chem. Phys. **108**, 2733 (1998)

[88] R. Baer and R. Kosloff, J. Chem. Phys. **106**, 8862 (1997)

[89] H.-D. Meyer, U. Manthe, and L. S. Cederbaum, Chem. Phys. Lett. **73**, 165 (1990)

[90] H.-D. Meyer, U. Manthe, and L. S. Cederbaum, *in Numerical Grid Methods and Their Application to Schrödinger equation*, pages 141–152, Kluwer Academic, The Netherlands, 1993

[91] M. H. Beck, A. Jäckle, G. A. Worth, and H.-D. Meyer, Phys. Rep. **324**, 1 (2000)

[92] H. Wang, J. Chem. Phys. **113**, 9948 (2000)

[93] R. Baer, Y. Zeiri, and R. Kosloff, Phys. Rev. B **55**, 10952 (1997)

[94] C. P. Koch, T. Klüner, H.-J. Freund, and R. Kosloff, J. Chem. Phys. **119**, 1750 (2003)

[95] C. P. Koch, T. Klüner, and R. Kosloff, J. Chem. Phys. **116**, 7983 (2002)

[96] C. P. Koch, T. Klüner, H.-J. Freund, and R. Kosloff, Phys. Rev. Lett. **90**, 117601 (2003)

[97] A. O. Caldeira, A. H. C. Neto, and T. O. de Carvalho, Phys. Rev. B **48**, 13974 (1993)

[98] K. Forsythe and N. Makri, Phys. Rev. B **60**, 972 (1998)

[99] S. Tsonchev and P. Pechukas, Phys. Rev. E **61**, 6171 (1999)

[100] N. V. Prokof'ev and P. Stamp, Rep. Prog. Phys. **63**, 669 (2000)

[101] J. Shao and P. Hänggi, Phys. Rev. Lett. **81**, 5710 (1998)

[102] W. H. Louisell, *Quantum Statistical Properties of Radiation*, Wiley, New York, 1990

[103] J. von Neumann and E. Wigner, Physik. Z **30**, 467 (1929)

[104] E. Teller, J. Phys. Chem. **41**, 109 (1937)

[105] D. Yarkony, J. Chem. Phys. **114**, 2601 (2001)

[106] H. Nakamura, *Nonadiabatic Transition*, World, River Edge, 2002

[107] J. Michl and V. Bonačić-Koutecký, *Electronic Aspects of Organic Photochemistry*, Wiley, New York, 1990

[108] W. Domcke, D. Yarkony, and H. Köppel, editors, *Conical Intersections. Electronic Sructure, Dynamics and Spectroscopy*, World Scientific, Singapore, 2004

[109] G. Stock and W. Domcke, Adv. Chem. Phys. **100**, 1 (1997)

[110] J. Cao, M. Messina, and K. R. Wilson, J. Chem. Phys. **106**, 5239 (1997)

[111] W. Zhu and H. Rabitz, J. Chem. Phys. **118**, 6751 (2003)

[112] R. Xua, Y. Yan, Y. Ohtsuki, Y. Fujimura, and H. Rabitz, J. Chem. Phys. **120**, 6600 (2004)

[113] W. T. Pollard and R. A. Friesner, J. Chem. Phys. **100**, 5054 (1994)

[114] R. Kosloff and H. Tal-Ezer, Chem. Phys. Lett. **127**, 223 (1986)

[115] M. R. Wall and D. Neuhauser, J. Chem. Phys. **102**, 8011 (1995)

[116] V. A. Mandelshtam and H. Taylor, J. Chem. Phys. **107**, 6756 (1997)

[117] J. Pang, T. Dieckmann, J. Feigon, and D. Neuhauser, J. Chem. Phys. **108**, 8360 (1998)

[118] J. S. Bader and B. J. Berne, J. Chem. Phys. , 8359 (1994)

[119] M. Nest and H.-D. Meyer, J. Chem. Phys. **119**, 24 (2003)

[120] I. Burghardt, M. Nest, and G. A. Worth, J. Chem. Phys. **119**, 5364 (2003)

[121] N. Makri, Annu. Rev. Phys. Chem. **50**, 167 (1999)

[122] M. H. Beck, A. Jäckle, G. A. Worht, and H.-D. Meyer, Phys. Rev. **324**, 1 (2000)

[123] H.-D. Meyer and G. A. Worth, Theor. chim. Acta **109**, 251 (2003)

[124] G. A. Worth, H.-D. Meyer, and L. S. Cederbaum, J. Chem. Phys. **105**, 4412 (1996)

[125] V. Romero-Rochin and I. Oppenheim, Physica A **155**, 52 (1989)

[126] T. Mančal and V. May, J. Chem. Phys. **114**, 1510 (2001)

[127] D. Guilini, E. Joos, C. Kiefer, J. Kupsch, I.-O. Stamatescu, and H. D. Zeh, editors, *Decoherence and the Appearence of a Classical World in Quantum Theory*, Springer-Verlag, Berlin, 1996

[128] F. Haake and R. Reibold, Phys. Rev. A **32**, 2462 (1985)

[129] A. K. Rajagopal, Phys. Lett. A **246**, 237 (1998)

[130] W. T. Strunz, F. Haake, and D. Braun, Phys. Rev. A **67**, 022101 (2003)

[131] J. P. Paz and W. H. Zurek, Phys. Rev. Lett. **82**, 5181 (1999)

[132] U. Banin, A. Bartana, S. Ruhman, and R. Kosloff, J. Chem. Phys. **101**, 8461 (1994)

[133] W. H. Zurek, Phys. Rev. D **26**, 1862 (1982)

[134] E. Joos and H. D. Zeh, Z. Phys. B: Condens. Matter **59**, 223 (1985)

[135] D. Braun, Phys. Rev. Lett. **89**, 277901 (2002)

[136] F. Benatti, R. Floreanini, and M. Piani, Phys. Rev. Lett. **91**, 070401 (2003)

[137] A. Peres, Phys. Rev. Lett. **77**, 1413 (1996)

[138] M. Horodecki, P. Horodecki, and R. Horodecki, Phys. Lett. A **223**, 1 (1996)

[139] C. H. Bennett, D. P. DiVincenzo, J. A. Smolin, and W. K. Wootters, Phys. Rev. A **54**, 3824 (1996)

[140] S. Hill and W. K. Wootters, Phys. Rev. Lett. **78**, 5022 (1997)

[141] W. K. Wootters, Phys. Rev. Lett. **80**, 2245 (1998)

[142] G. Lindblad, J. Math. Phys. **39**, 2763 (1998)

[143] J. Vala and R. Kosloff, unpublished, 2002

[144] D. Gelman and R. Kosloff, Chem. Phys. Lett. **381**, 129 (2003)

[145] W. M. Gelbart, S. A. Rice, and K. F. Freed, J. Chem. Phys. **57**, 4699 (1972)

[146] P. A. Mello, P. P. , and N. Kumar, J. Stat. Phys. **51**, 77 (1988)

[147] A. Bulgac, G. D. Dang, and D. Kusnezov, Phys. Rev. E **54**, 3468 (1996)

[148] E. Lutz and H. A. Weidenmüller, Physica A **267**, 354 (1999)

[149] M. Esposito and P. Gaspard, Phys. Rev. E **68**, 066113 (2003)

[150] D. Cohen and T. Kottos, Phys. Rev. E **69**, 055201 (2004)

[151] A. M. Ferrenberg, D. P. Landau, and K. Binder, J. Stat. Phys. **63**, 867 (1991)

[152] G. Ashkenazi, R. Kosloff, S. Ruhman, and H. Tal-Ezer, J. Chem. Phys. **103**, 10005 (1995)

[153] Y. Huang, D. J. Kouri, and D. Hoffman, J. Chem. Phys. **101**, 10497 (1994)

[154] R. Kosloff, A. D. Hammerich, and D. Tannor, Phys. Rev. Lett. **69**, 2172 (1992)

[155] M. Mehta, *Random Matrices*, Academic, New York, second edition, 1991

[156] V. V. Dobrovitski and H. A. D. Raedt, Phys. Rev. E **67**, 56702 (2003)

[157] U. Peskin and M. Steinberg, J. Chem. Phys. **109**, 704 (1998)

[158] M. Born and J. R. Oppenheimer, Ann. Phys. **87**, 457 (1927)

[159] F. Bernardi, S. De, M. Olivucci, and M. Robb, J. Am. Chem. Soc. **112**, 1737 (1990)

[160] F. Bernardi, M. Olivucci, and M. Robb, Chem. Soc. Rev. **25**, 321 (1996)

[161] L. D. Landau, Physik. Z. Sowjetunion **2**, 46 (1932)

[162] C. Zener, Proc. R. Soc. A. **137** (1932)

[163] M. Baer, Adv. Chem. Phys. **124**, 39 (2002)

[164] M. Bixon and J. Jortner, Adv. Chem. Phys. **106**, 35 (1999)

[165] A. Nitzan and J. Jortner, J. Chem. Phys. **56**, 5200 (1972)

[166] T. Kobayashi, Y. Takagi, H. Kandori, K. Kemnitz, and K. Yoshihara, Chem. Phys. Lett. **180**, 416 (1991)

[167] P. J. Reid, C. Silva, P. F. Barbara, and J. T. Hupp, J. Phys. Chem. **99**, 2609 (1995)

[168] P. F. Barbara, G. C. Walker, and T. P. Smith, Science **256**, 975 (1992)

[169] P. Kambhampati, D. H. Son, T. W. Kee, and P. F. Barbara, J. Phys. Chem. A **104**, 10637 (2000)

[170] H. Köppel, W. Domcke, and L. Cederbaum, Adv. Chem. Phys. **57**, 59 (1984)

[171] A. Toniolo, G. Granucci, and T. J. Martinez, J. Phys. Chem. A **107**, 3822 (2003)

[172] A. Toniolo, M. Ben-Nun, and T. J. Martinez, J. Phys. Chem. A **107**, 829 (2003)

[173] A. Toniolo, S. Olsen, L. Manohar, and T. J. Martinez, Faraday Discuss. Chem. Soc. **127**, 149 (2004)

[174] G. Worth, H.-D. Meyer, and L. Cederbaum, J. Chem. Phys. **109**, 3518 (1998)

[175] A. Kühl and W. Domcke, J. Chem. Phys. **116**, 263 (2002)

[176] T. Gerdts and U. Manthe, Chem. Phys. Lett. **295**, 167 (1998)

[177] W. Domcke and H. Köppel, Chem. Phys. Lett. **140**, 133 (1987)

[178] G. Stock, R. Schneider, and W. Domcke, J. Chem. Phys. **90**, 7184 (1989)

[179] G. Herzberg and H. C. Longuet-Higgins, Faraday Discuss. Chem. Soc. **35**, 77 (1967)

[180] T. Klüner, S. Thiel, and V. Staemmler, J. Phys. B: Atomic Molecular and Optical Physics **32**, 4931 (1999)

[181] T. Pacher, L. Cederbaum, and Köppel, Adv. Chem. Phys. **84**, 293 (1993)

[182] A. Ferretti, A. Lami, and G. Villani, J. Chem. Phys. **106** (1997)

[183] G. Katz, Y. Zeiri, and R. Kosloff, Chem. Phys. Lett. **358**, 284 (2002)

[184] P. Saalfrank, R. Baer, and R. Kosloff, Chem. Phys. Lett. **230**, 463 (1994)

[185] L. Diósi, Physica A **199**, 517 (1993)

[186] L. Diósi, N. Gisin, and W. T. Struntz, Phys. Rev. A **58**, 1699 (1998)

[187] R. Schoenlein, L. Peteanu, R. A. Mathies, and C. V. Shank, Science **254**, 412 (1991)

[188] N. H. Damrauer, G. Cerullo, A. Yeh, T. R. Boussie, C. V. Shank, and J. K. McCusker, Science **275**, 54 (1997)

[189] Q. Wang, R. W. Schoenlein, L. A. Peteanu, R. A. Mathies, and C. V. Shank, Science **266**, 5184 (1994)

[190] A. T. Yeh, C. V. Shank, and J. K. McCusker, Science **289**, 235 (2000)

[191] E. Gershgoren, J. Vala, R. Kosloff, and S. Ruhman, J. Phys. Chem. A **105**, 5081 (2001)

[192] L. Ungar and J. Cina, Adv. Chem. Phys. **100**, 171 (1997)

[193] N. Scherer, R. Carlson, A. Matro, M. Du, A. Ruggiero, V. Romero-Rochin, J. Cina, G. Fleming, and S. Rice, J. Chem. Phys. **95**, 1487 (1991)

[194] G. Stock and W. Domcke, Phys. Rev. A **45**, 3032 (1992)

[195] L. Seidner, G. Stock, and W. Domcke, J. Chem. Phys. **103**, 3998 (1995)

[196] R. Schneider, W. Domcke, and H. Köppel, J. Chem. Phys. **92**, 1045 (1990)

[197] V. Mandelshtam, J. Chem. Phys. **108**, 9999 (1998)

[198] H. Köppel, L. Cederbaum, and W. Domcke, J. Chem. Phys. **89** (1988)

[199] U. Manthe and H. Köppel, J. Chem. Phys. **93**, 345 (1990)

[200] F. Santoro and C. Petrongolo, J. Chem. Phys. **110**, 4419 (1999)

[201] A. Kühl and W. Domcke, Chem. Phys. **259**, 227 (2000)

[202] D. Gelman, C. Koch, and R. Kosloff, J. Chem. Phys. **121**, 661 (2004)

[203] D. Lockwood, M. Ratner, and R. Kosloff, J. Chem. Phys. **117** (2002)

[204] G. Ashkenazi, R. Kosloff, and M. A. Ratner, J. Am. Chem. Soc. **121**, 3386 (1999)

[205] B. Kohler, V. V. Yakovlev, J. Che, J. L. Krause, M. Messina, K. R. Wilson, N. Schwentner, R. M. Whitnell, and Y. Yan, Phys. Rev. Lett. **74**, 3360 (1995)

[206] C. J. Bardeen, Q. Wang, and C. V. Shank, Phys. Rev. Lett. **75**, 3410 (1995)

[207] G. Cerullo, C. J. Bardeen, Q. Wang, and C. V. Shank, Chem. Phys. Lett. **262**, 362 (1996)

[208] C. J. Bardeen, Q. Wang, and C. V. Shank, J. Phys. Chem. A **102**, 2759 (1998)

[209] A. H. Buist, M. Müller, R. I. Ghauharali, G. J. Brakenhoff, J. A. Squier, C. J. Bardeen, V. V. Yakovlev, and K. R. Wilson, Optics Letters **24**, 244 (1999)

[210] T. Brixner, N. H. Damrauer, P. Niklaus, and G. Gerber, Nature **414**, 57 (2001)

[211] K. Misawa and T. Kobayashi, J. Chem. Phys. **113**, 7546 (2000)

[212] S.-H. Lee, K.-H. Jung, J. H. Sung, K.-H. Hong, and C. H. Nam, J. Chem. Phys. **117**, 9858 (2002)

[213] K. A. Walowicz, I. Pastirk, V. V. Lozovoy, and M. Dantus, J. Phys. Chem. A **106**, 9369 (2002)

[214] V. I. Prokhorenko, A. M. Nagy, and R. J. D. Miller, J. Chem. Phys. **122**, 184502 (2005)

[215] S. Ruhman and R. Kosloff, J. Opt. Soc. Am. B **7**, 1748 (1990)

[216] D. H. Schirrmeister and V. May, Chem. Phys. Lett. **297**, 383 (1998)

[217] B. D. Fainberg, J. Chem. Phys. **109**, 4523 (1998)

[218] C. J. Bardeen, J. Cao, F. L. H. Brown, and K. R. Wilson, Chem. Phys. Lett. **302**, 405 (1999)

[219] V. Malinovsky and J. L. Krause, Phys. Rev. A **63**, 043415 (2001)

[220] B. D. Fainberg and V. Narbaev, J. Chem. Phys. **116**, 4530 (2002)

[221] R. S. Judson and H. Rabitz, Phys. Rev. Lett. **68**, 1500 (1992)

[222] J. Geremia, W. Zhu, and H. Rabitz, J. Chem. Phys. **113**, 10841 (2000)

[223] D. Meshulach and Y. Silberberg, Nature **396**, 239 (1998)

[224] D. Zeidler, S. Frey, K.-L. Kompa, and M. Motzkus, Phys. Rev. A **64**, 023420 (2001)

[225] B. J. Pearson, J. L. White, T. C. Weinacht, and P. H. Bucksbaum, Phys. Rev. A **63**, 063412 (2001)

[226] D. E. Goldberg, *Genetic Algorithms in Search, Optimization, and Machine Learning*, Addison-Wesley, Reading, MA, 1989

[227] O. Nahmias, O. Bismuth, O. Shoshana, and S. Ruhman, J. Phys. Chem. A **109**, 8246 (2005)

[228] S. A. Rice and M. Zhao, *Optical Control for Molecular Dynamics*, John Wiley and Sons, New York, 2000

[229] J. Vala and R. Kosloff, Optics Express **8**, 238 (2001)

[230] T. Hornung, R. Meier, and M. Motzkus, Chem. Phys. Lett. **326**, 445 (2000)

[231] Y. Zeiri, E. Fattal, and R. Kosloff, J. Chem. Phys. **102**, 1859 (1995)

[232] J. Cao, C. J. Bardeen, and K. R. Wilson, Phys. Rev. Lett. **80**, 1406 (1998)

[233] B. D. Fainberg and V. A. Gorbunov, J. Chem. Phys. **121**, 8748 (2004)

[234] C. J. Bardeen, S. J. Rosenthal, and C. V. Shank, J. Phys. Chem. A **103**, 10506 (1999)

[235] J. Cao, C. J. Bardeen, and K. R. Wilson, J. Chem. Phys. **113**, 1898 (2000)

[236] H. Tal-Ezer and R. Kosloff, J. Chem. Phys. **81**, 3967 (1984)

[237] C. P. Koch, *Quantum dissipative dynamics with a Surrogate Hamiltonian. The method and applications*, PhD thesis, Humboldt-Universität zu Berlin, www.edoc.hu-berlin.de/dissertationen/koch-christiane-2002-10-18/PDF/Koch.pdf, 2002

Appendix E

List of publications

The thesis is based on the following publications:

- D. Gelman and R. Kolsoff, "Simulating dissipative phenomena with a random phase thermal wavefunctions, high temperature application of the Surrogate Hamiltonian approach",

  Chem. Phys. Lett., **381**, 129, (2003).

- D. Gelman, C. P. Koch and R. Kosloff, "Dissipative quantum dynamics with the surrogate Hamiltonian approach. A comparison between spin and harmonic baths",

  J. Chem. Phys., **121**, 661, (2004).

- D. Gelman, G. Katz, R. Kosloff and M. A. Ratner, "Dissipative dynamics of a system passing through a conical intersection: Ultrafast pump-probe observables",

  J. Chem. Phys., **123**, 134112, (2005).

- D. Gelman and R. Kolsoff, "Minimizing broadband excitation under dissipative conditions",

  J. Chem. Phys. **123**, 234506, (2005).